ITATION PAGE

Form Approved
OMB No. 0704-0188

RT DATE	3. REPORT TYPE AND DATES COVERED
05-15-92	Technical 06-01-91 to 05-31-92

4. TITLE AND SUBTITLE
The Interface of Nanoscale Inclusion Chemistry

5. FUNDING NUMBERS
N00014-90-J-1159

6. AUTHOR(S)
G.D. Stucky

7. PERFORMING ORGANIZATION NAME(S) AND ADDRESS(ES)
University of California
Department of Chemistry
Santa Barbara, CA 93106

8. PERFORMING ORGANIZATION REPORT NUMBER
T2

9. SPONSORING/MONITORING AGENCY NAME(S) AND ADDRESS(ES)
Office of Naval Research
Chemistry Program
800 N. Quincy Street
Alexandria, VA 22217

10. SPONSORING/MONITORING AGENCY REPORT NUMBER

11. SUPPLEMENTARY NOTES
Prepared for Publication in Progress in Inorganic Chemistry

12a. DISTRIBUTION/AVAILABILITY STATEMENT
Approved for public release;
distribution unlimited

12b. DISTRIBUTION CODE

13. ABSTRACT *(Maximum 200 words)*

This review presents a selected review of nanoscale inclusion chemistry using 3-D periodic hosts with an emphasis on optical properties. Inclusion chemistry is defined in the context of the above discussion as the interaction between a 3-D host surfaces with one or more types of guests. It is an area receiving increased enthusiasm and interest because of the basic research concepts and challenges that remain to be explored. The host is in effect a solid state inorganic "molecular recognition" template. Ideally, this packaging would make it possible to: selectively modulate the host framework electronic or optical properties with guest atoms or molecules; impose selected order-disorder constraints on the self-organization process; modify internanophase behavior by varying the host dielectric constant and guest concentration; generate electronically or coordinatively unsaturated atomic assemblies; synthesize nanocomposite materials in which the host and guest interact in a synergistic or combinatorial fashion to give tunable or new properties.

14. SUBJECT TERMS	15. NUMBER OF PAGES
	81
	16. PRICE CODE

17. SECURITY CLASSIFICATION OF REPORT	18. SECURITY CLASSIFICATION OF THIS PAGE	19. SECURITY CLASSIFICATION OF ABSTRACT	20. LIMITATION OF ABSTRACT
Unclassified	Unclassified	Unclassified	UL

OFFICE OF NAVAL RESEARCH

Contract N00014-90-J-1159
R&T Code 413n007

Technical Report No. 2

The Interface of Nanoscale Inclusion Chemistry

by

G.D. Stucky

Prepared for Publication in

Progress in Inorganic Chemistry

May 15, 1992

Galley Proof

The Interface of Nanoscale Inclusion Chemistry

GALEN D. STUCKY

Department of Chemistry
University of California
Santa Barbara, California

CONTENTS

I. INTRODUCTION 000

A. Materials Synthesis and Nanoscale Inclusion Chemistry 000
B. Examples of Optical Applications 000
1. Quantum Confinement 000
2. Off-Resonance Nonlinear Optics 000
C. Some Nanoscale Hosts 000
1. Glasses and Disordered Media 000
2. Layered Nanoscale Synthesis and One-Dimensional Confinement of Ordered Arrays 000
3. Three-Dimensional Surfaces and Periodic Packaging 000
D. Guests 000

II. HOST COMPOSITION AND TOPOGRAPHY 000

A. Zeolites 000
B. Molecular Sieves and Tetrahedral Atom Open Framework Hosts 000
C. Nontetrahedral Atom Open Framework Structures 000
D. Other Large Channel Systems 000
E. Nonlinear Optic Hosts—$KTiOPO_4$ Structural Family 000

III. THE HOST–GUEST RELATIONSHIP 000

A. Host Variables in Interface Dynamics 000
1. Three-Dimensional Surface Electric Fields 000
2. Framework Flexibility 000
3. External Tuning of Host Response by Temperature, Pressure, and Electric Fields 000
4. Guest Modification of Host Electronic and Optical Properties 000
5. Host Surface Reconstruction and Modification 000
B. Guest Variables in Interface Dynamics 000
1. Exterior Surface–Interior Surface Considerations and Pore Size Constraints ... 000

Progress in Inorganic Chemistry, Vol. 40, Edited by Stephen J. Lippard.
ISBN 0-471-57191-1

2. The Host–Guest Interface and Self-Organization 000
3. Nanocluster Guests and Quantum Confinement 000

IV. NANOCOMPOSITE SYNTHESIS AND PROPERTIES USING THREE-DIMENSIONAL SURFACE CONFINEMENT 000

A. Charge Carrier Cluster Guests 000
1. Sodalite Based Hosts 000
2. Larger Cage Packaging 000
3. Large Channel Host Confinement 000
B. Oriented Organic Nonlinear Optic Guests 000
1. Background 000
2. Host Considerations 000
3. Guest Considerations 000
4. Organic Nucleation in Channels 000
C. Nonlinear Optic Framework Active Hosts 000
1. Background 000
2. Synthesis Phase Space and Combination Phases 000
3. Selective Siting and Pinning of Delocalized Excited States 000

V. CONCLUSION 000

ACKNOWLEDGMENTS 000

REFERENCES 000

I. INTRODUCTION

A. Materials Synthesis and Nanoscale Inclusion Chemistry

Even though solid state chemistry has been fundamental to the technological evolution of human history from prehistoric times, the synthesis of solid materials still remains in its infancy. The apparent simplicity of this chemistry quickly vanishes when one considers that hypothetically the perfect crystal can be only obtained at absolute zero. The thermodynamically favored crystal composition of an extended solid is one in which some atomic sites are vacant or there is displacement of atoms from the lattice sites. The law of definite proportions used in molecular chemistry is no longer valid, and bulk physical properties can be widely varied with the same chemical stoichiometry by changing defect concentration. In addition, most crystalline materials can exist as solid solutions with variable composition, allowing chemists to design a wide variety of new materials with specific properties. A perusal of the development of semiconductor and ferroelectric materials quickly establishes the importance of these parameters as both liabilities and assets. These considerations also suggest the reason why the evolution of solid state chemistry has resulted in a relatively

large body of literature on single element, binary and, to a much smaller extent, ternary metal atom compositions with only a glimmer of what lies beyond in higher order phases.

Another dimension to materials synthesis has been added recently with the chemists' ability to create *nanoscale phases*. In the nanoscale size regime, where the volume-to-surface area ratio of the bulk material rapidly decreases, one finds, for example, the transition from an extended band structure to a quantum confined structure. In nucleation and synthesis chemistry the nanoscale dimension is a region of phase and chemical instability in which a given thermodynamic path becomes unstable and several options (new steady or thermodynamic states) are available. Physically, this simply means that the intermolecular and interatomic interaction energies associated with self-assembly are of the same order of magnitude as the attractive energy that the atoms or molecules have for their surroundings. The chemistry of this nucleation process is, therefore, particularly sensitive to changes in composition and external effects such as temperature, electric fields, or anything that even slightly perturbs the dynamics and kinetics of the system. In nanoscale phases, large chemical or physical fluctuations can be generated and potentially used. It is a region in which cooperative nonlinear behavior describes the physics and chemistry of the system, with processes of the "bifurcation" type.

Because nanophase chemistry has proven important to a wide variety of fields, ranging from atom and electron transport in biological systems, heterogeneous catalysis, and photocatalysis to the development of new electrooptic devices based on quantum confinement, there has been an explosion of interest in this area by scientists from many disciplines. Syntheses of nanoscale phases have been carried out in numerous ways to give unexpectedly different materials with varied structural, optical, and transport properties. Molecular inorganic chemists, physical chemists, and biochemists have begun to address the question of what happens to molecular properties as larger clusters are formed, and have generated nanoclusters by building up arrays from solution or gas phases atom by atom (1–4). From the other direction, solid state physicists and engineers have focused on the properties of a bulk material as it is subdivided into atomic arrays with increasingly smaller and smaller dimensions by using engineering based directly on solid state atomic lattice substrates (5, 6). Instead of cutting the bulk into smaller pieces, one also can ask what happens when the lattice is expanded and internuclear separations are increased. Nanophase materials chemistry requires a precise definition of the number of atoms, their siting (e.g., bulk vs. surface), the manner in which they are assembled on the surface, and the nature of the interface interactions with their surroundings. It is for these reasons that while the convergence of molecular and solid state chemistry is near, the somewhat diffuse materials synthesis interface between isolated clusters and the infinite solid array is only beginning to be resolved.

With few exceptions, the isolated nanocluster or nanoarray of atoms is only part of the story. For most practical applications, the nanoclusters must be incorporated into a processable matrix. This combination of a host matrix and the guest nanoarray defines a *nanocomposite*, a material consisting of two or more phases with different physical properties that are interfaced at nanoscale dimensions. The nanocomposite can be constructed by (a) monolayer engineering on selected substrate hosts, (b) direct synthesis as in clathrates, (c) nanophase synthesis within a three-dimensional (3-D) porous host, (d) creating both host and guest then diffusing (via gas or melt) the guest into the empty host, or (e) ion or molecular exchange. The figure of merit parameters that might be used to optimize a nanocomposite are defined by the property of interest or the intended application.

The importance of the host–guest interface for synthesizing nanoclusters or arrays has been noted above. This interface is a two-way street, which suggests an alternative approach to designing materials. Instead of using the host as a self-organization governing parameter to define the nanocomposite properties through variation of the guest topography, the *guest can be used to modify the electronic and structural properties of the host surface*. This can be particularly effective for 3-D host surfaces. In this context it should be noted that solid state structural chemistry is commonly viewed from a static point of view using matrix algebra. Because 3-D porous materials have a unique interconnectedness, large surface areas, and flexibility, Andersson et al. (7) suggested that it is more appropriate to treat porous hosts as minimal surfaces using calculus and differential geometry. Dynamic processes, such as phase transitions, diffusion, and ionic conductivity, are naturally defined in terms of the surface continuum by this approach. Heats of absorption are shown to be directly proportional to the surface curvature for various hydrocarbons. This is an enticing visual model to use in thinking about the consequences of the mechanism by which a guest modifies the properties of a 3-D extended surface.

This article presents a selected review of *nanoscale inclusion chemistry using 3-D periodic hosts with an emphasis on optical properties*. Inclusion chemistry is defined in the context of the above discussion as the interaction between a 3-D host surface with one or more types of guests. It is an area receiving increased enthusiasm and interest because of the basic research concepts and challenges that remain to be explored. The host is in effect a solid state inorganic "molecular recognition" template. Ideally, this packaging would make it possible to:

Selectively modulate the host framework electronic or optical properties with guest atoms or molecules.

Impose selected order–disorder constraints on the self-organization process.

Modify internanophase behavior by varying the host dielectric constant and guest concentration.

Generate electronically or coordinatively unsaturated atomic assemblies.

Synthesize nanocomposite materials in which the host and guest interact in a synergistic or combinatorial fashion to give tunable or new properties.

B. Examples of Optical Applications

1. Quantum Confinement

Nanocluster materials already have had a significant impact in the area of photonic–electronic devices. The miniaturization of electronic and optic devices has revolutionized response times, energy loss, and transport efficiency. In addition, the presence or absence of a few atoms and the geometrical disposition of each atom can significantly modify electronic and photonic properties as one approaches the nanosize regime. This control can be further supplemented by "packaging" assemblies of atoms or molecules into thin-film or nanocomposite bulk materials to define surface states, cluster environment and geometry, intercluster interactions, and consequently, a wide tunable range of optical and charge carrier responses.

One specific example attracting commercial interest is optical data storage (Fig. 1). In writing an optical disk it is desirable to obtain the highest possible resolution and optical density. Laser beam collimation is one technique used to optimize the optical density. Unfortunately, collimation is limited by diffraction effects. In addition, the intensity of the laser beam is not homogeneous in cross section, which also restricts the resolution and sharpness of reproduction. Nanosized semiconductors display a peculiar nonlinear optic property: They will absorb light if it is not too intense, but will transmit light if the number of photons surpasses a certain threshold value. By using a thin-film mask containing the semiconductor cluster during writing, only the center portion of the beam, which has a photon flux above a certain intensity cutoff, is transmitted, resulting in a dramatic (~50%) improvement of both optical density and recording quality. Using shorter wavelengths could further improve the resolution. Fortunately, the optical absorption and emission bands of a semiconductor are shifted to shorter wavelengths if the semiconductor atoms are in an appropriately small cluster. These effects are the consequences of the electrons in the semiconductor being quantum confined. Obviously, the desired size of the cluster is the first property that needs to be considered in creating a nanocomposite containing the above semiconductor nanoclusters. In principal this can be arbitrarily adjusted.

Potential applications of quantum confined materials have been demonstrated to be feasible in the areas of photocatalysis (8), phase conjugate optical systems, optical switching for parallel data processing, resonant tunneling and field effect transistors, low-gain lasers and frequency mixing (9, 10). The primary limitation is the materials synthetic chemist's ability to create and package nano-

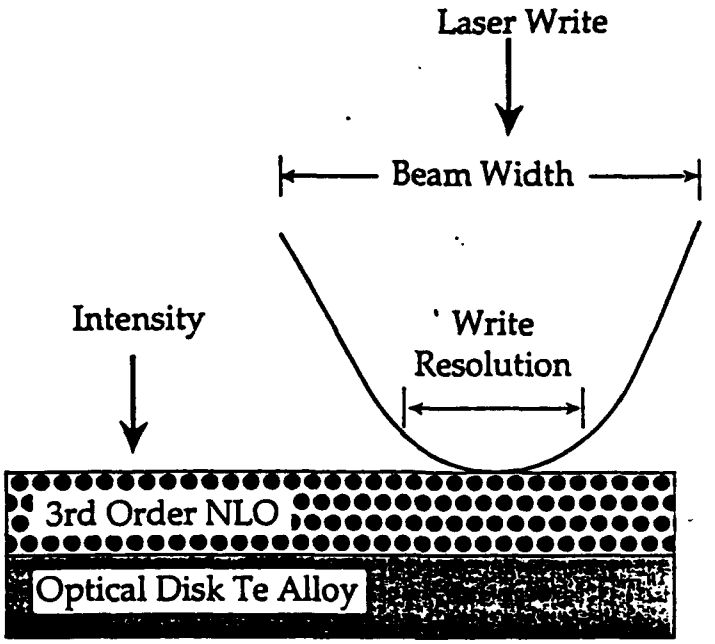

Figure 1. Optical disk data storage using quantum-confined semiconductor clusters.

phases in such a way as to obtain a uniform precise size, intercluster separation, optical density, and suitable processability.

2. *Off-Resonance Nonlinear Optics*

Nonlinear optics is concerned with how the electromagnetic field of a light wave interacts with the electromagnetic fields of matter and of other light waves. The interaction of light with a honlinear optical material will cause the material's properties to change, and the next photon that arrives will "see" a different material. As light travels through a material, its electric field interacts with other electric fields within the material. These internal fields are a function of the time dependent electron density distribution in the material and the electric fields of the other light waves, if, for example, two or more light sources are used. In a nonlinear optical (NLO) material, strong interactions can exist among the various fields. These interactions may change the frequency, phase, polarization, or path of incident light. The chemist's goal in the field is to develop materials that control this mediation so that one can modulate or combine photons (wave mixing). In addition, it is necessary to fine tune both the magnitude and response time of the optical processes.

Inclusion chemistry can be and currently is used in this field in several ways. For example, ion exchange inclusion chemistry in the potassium titanyl phosphate structural field is an effective way to create optic wave guides and electrooptic switches (11). It also can be used to enhance or decrease the second-order harmonic generation (SHG) of the photons, that is, frequency doubling of an incident laser beam. These topics are discussed in more detail below. A second use of inclusion chemistry is to align polar molecules within a polar host or by Langmuir–Blodgett engineering to give poled layered superlattice structures. The enhancement of the thermal and photostability of organic NLO molecules by packaging in inorganic hosts may ultimately prove to be the most important role of inclusion chemistry in practical applications.

Again, it should be emphasized that a precise synthetic definition of the number of atoms or molecules, their siting (e.g., nanophase bulk vs. surface), topography, orientation, and the manner in which they are assembled on the 3-D host surface to form a nanocomposite array is required in order to take maximum advantage of the unique properties associated with nanophase composites. A compromise using porous glasses or polymer supports is sometimes commercially necessary for processability or materials cost advantage, and for some applications the figure of merit criteria can be met with this in mind.

C. Some Nanoscale Hosts

As previously stated, this paper is concerned primarily with 3-D inorganic periodic hosts. Porous glasses, organic media, and layered materials play an important role in nanocomposite inclusion chemistry and some comments concerning their use are briefly presented.

1. Glasses and Disordered Media

Porous glasses (12), polymers (13, 14), micelles (15), and colloids (16) have been used as host matrices for encapsulating atomic arrays. Specific examples include the formation of PbS particles on ethylene–methacrylic acid copolymers (17), and glass matrices around colloidal solutions of CdS (18). In all of these systems, however, the crystallinities, pore sizes, and ultimate cluster geometry are not well defined. Nevertheless, porous glasses are promising in that they offer the advantages of providing a large range of pore sizes, ease of optical characterization, and the potential for use as thin monoliths in optical devices. Photo and thermal stability are crucial if the nanocomposites are to be used in laser device applications. In optical computer or optical switching applications, for example, the nanocomposite should be able to perform trillions of switching operations per second for years at a time. As inorganic hosts, porous glasses have been demonstrated to greatly increase the lifetime of organic dye lasers,

which have been built into their pores (19). This is an important property of the inorganic host–organic guest combination that will undoubtedly be pursued further. Several types of sol-gel derived glass have been used in attempts to vary the size of the particles that are produced. In addition to the sol-gel derived glasses, commercial Vycor® (Corning Glass) has been used. Vycor® is significantly stronger than the sol-gel derived glass since it is synthesized via a high temperature acid leaching process of borosilicates. The high temperature imparts mechanical strength to the glass.

2. *Layered Nanoscale Synthesis and One-Dimensional Confinement of Ordered Arrays*

Sophisticated techniques currently are available to obtain one-dimensional (1-D) nanocomposites consisting of atomic or molecular monolayers (-5 Å) by molecular beam epitaxy (MBE), electrochemical, atomic layer epitaxy (ALE) (20) and Langmuir–Blodgett film synthesis (21–23). Both MBE and ALE allow for the fabrication of ultrathin (monolayer) semiconductor layers, and have lead to the design and creation of 1-D quantum confined materials. Figure 2 shows how carrier confinement is achieved by sandwiching a GaAs semiconductor layer between two wider-bandgap semiconductor epitaxial layers (24–26).

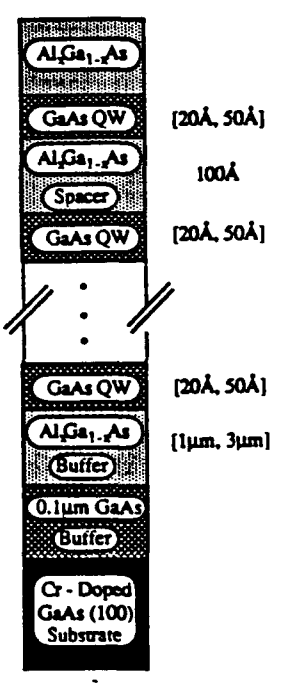

Figure 2. Molecular beam epitaxy derived quantum superlattice (24).

The superlattice layered structure approach is an important step towards achieving the degree of sophistication required to obtain a periodic array of quantum confined planes of atoms. The development of photonic transistors or other electronic device analogs, however, requires two-dimensional (2-D) (quantum wires) and 3-D (quantum dots) confined structures. Some ingenious approaches to this problem include using tilted and serpentine superlattices with the goal of creating lateral surfaces for 2-D and 3-D confinement with boxes or walls with dimensions less than about 100 Å.

3. *Three-Dimensional Surfaces and Periodic Packaging*

In MBE and ALE nanostructure synthesis, a 2-D layered substrate is used. A natural extension of quantum confinement generated from 2-D surface construction is prelateral patterning in 3-D. Ideally, the resultant nanocomposite would have the following properties:

Size and topographical uniformity of nanophases.
Supra-lattice 3-D periodicity as defined by the host.
Tunability with respect to atomic modification of
  Topography.
  Nanophase dimensions.
  Surface states defined by the guest–host interface.
  Intercluster interactions.
Thermal and optical stability.
Optical transparency.

The basis for this approach is that instead of a 2-D substrate surface, one uses a 3-D surface defined by a periodic array of channels and/or cages. With such a 3-D crystalline template one can strive to package assemblies of atoms into quantum wires or dots that are unisized with identical geometries and have 3-D periodicity.

Molecular sieves and zeolites are examples of possible 3-D substrates consisting of periodic crystalline porous frameworks with open channels and cages. They have extremely high-internal surface areas, as much as 700 $m^2\ g^{-1}$ and as high as about 50% void space so that high concentrations of nanoclusters and optical densities are possible. Clusters and molecules can be incorporated within these cages and channels either directly during synthesis, by "ship in the bottle" synthesis within the host, or by gas phase or melt inclusion into an empty host. The thermal stability of these frameworks depends on the framework composition, but in some cases it is over 1000°C.

A limitation of zeolite structures is the relatively small cage and pore sizes. The 120 atom 26-hedron cages of zeolites RHO and Y provide possible cluster diameters to about 11–13 Å. The development of new larger pore molecular sieves is being actively pursued by numerous groups using Hoffman and 3-D linked molecular rod complexes (27, 28) for the building blocks of open framework structures, new approaches to molecular sieve synthesis, and open frameworks containing both four- and six-coordinate metal ions. The scientific community can expect to have available stable 3-D periodic molecular sieves with dimensions up to 100 Å in the not too distant future.

In this chapter we will usually reserve "zeolite" to refer to aluminosilicate porous hosts, "molecular sieves" to consist of any other porous hosts that can be emptied and used to selectively absorb molecules, and "open framework" structures as those which, while possessing sizeable channels and cages, cannot have the template removed or be ion exchanged without loss of structure. Clathrosils and clathrate structures in general are another important category in which the guest template molecule is permanently included during synthesis into closed cages. Bilayer inorganic materials with mismatched layer lattices form ordered tubular structures with channel dimensions between 20 and 100 Å and have been used to synthesize metallic wires (29–31).

Modification of host electronic properties can be carried out by reversible ion and gas exchange with small molecules (NH_4^+/NH_3 and H_3O^+/H_2O). Defect pyrochlores (32), such as $K(H_2O)_y[NbWO_6]$ (33), and conducting transition metal oxides (e.g., hexagonal WO_3^{x-}) or sulfides (e.g., $Mo_6S_8^{x-}$) fall into this category (34). The potassium titanyl phosphate, $KTiOPO_4$, structure (35–37) also can be modified for nonlinear optic applications by inclusion chemistry and is discussed below.

D. Guests

This chapter focuses on semiconductor inorganic clusters and organic molecules with large hyperpolarizabilities, that is, guests that have large nonlinear responses. The use of simple atomic guests for surface modification in framework active hosts also will be described.

II. HOST COMPOSITION AND TOPOGRAPHY

There are numerous review articles and books (38–41) on zeolites and molecular sieves that give a comprehensive review of these hosts. The following section gives a brief overview with selected highlights describing some recent advances in the field.

A. Zeolites

Topologically, the 3-D surface of a zeolite can be constructed from corner shared MO_2 tetrahedra. Zeolites, in their narrow definition, are naturally occurring or synthetically made materials whose chemical composition can be described as $[(M/Al)O_2]_x \cdot [SiO_2]_y$, where "M" represents a monovalent organic or inorganic cation. Polyvalent cations also can be used as templates with appropriate adjustments in charge and mass balance. By using large organic and inorganic templates during synthesis these monolayers interconnect into polyhedral or tubular configurations to form cages and channels. Figure 3 shows an

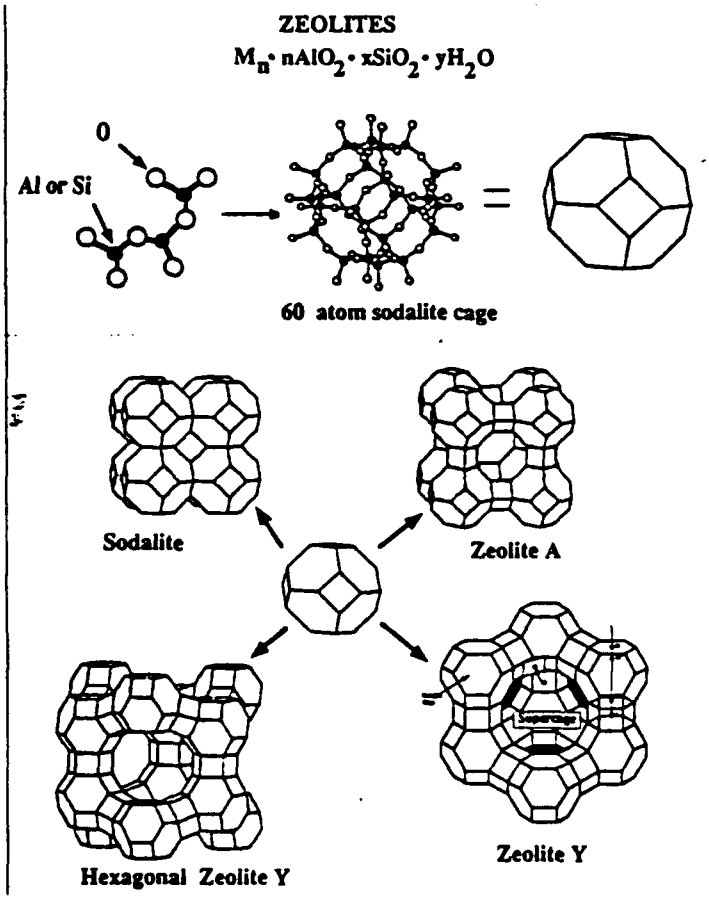

Figure 3. Aluminosilicate members of the sodalite family of zeolite structures. The polyhedron are drawn with tetrahedral metal atoms at the vertices, oxygen atoms are omitted.

example of condensation of the AlO_2^- and SiO_2 units into a 60-atom (silicon, aluminum, and oxygen atoms) sodalite cage, which geometrically is a truncated octahedron. The upper-right-hand portion of Fig. 3 shows only the 24 metal atoms that make up the sodalite cage. The 36 oxygen atoms connecting these metal atoms (middle, *top* of Fig. 3) make up the remainder of the 60 atoms in the polyhedron. In deference to current research activities on 60-atom cages (42), this structure might be considered as a saturated inorganic polyether Buckyball isomer.

The usual convention is to designate the pore openings by the metal atoms only. Thus, the term "6 ring" is used to describe the hexagonal faces shown for the sodalite cage in the upper-right-hand corner of Fig. 3. The reader should be aware that these are, in fact, 12 atom ring openings with alternating metal and oxygen atoms. Similarly, the "4 rings" define 8-atom (metal + oxygen atoms) ring openings. In the remainder of this chapter we will retain the usual zeolite molecular sieve convention of denoting these pores by the metal atoms only (i.e., as 6 and 4 rings).

This simple cage structure is an important fundamental building block and can be used to generate different porous zeolite structures by structural architecture based on putting together "clusters of cages," as shown in Fig. 3 for sodalite, zeolite A, zeolite Y, and the hexagonal form of zeolite Y. In these structures, the oxygen atoms coordinated perpendicular to the surface of the truncated octahedron can be part of another cage (sodalite) or serve as connections to other cages (zeolite A and Y structures). The net result is a periodic, 3-D crystalline lattice of cages and channels (Fig. 4). As illustrated, zeolite Y has two types of cages available for cluster formation, the smaller 6-Å sodalite units and the larger 13-Å alpha cages (Figs. 3 and 4). For the purposes of this discussion there are five sites (I, I′, II, II′, III) that are available for cation siting within the sodalite and supercages. It is important to note that the ion exchange process can yield very different siting of cations depending on temperature, pH, solvent versus melt ion inclusion, other extra-framework ions, calcination, and loading levels.

A large variety of cages are possible. Excluding the intercage interconnecting oxygen atoms, the cage (point group O_h) for zeolite RHO ($M_{12}Al_{12}Si_{36}O_{96}$, M = monovalent cation) is defined by 120 framework Si, Al, and O atoms (Fig. 5). In this zeolite the void space "outside" the cages has exactly the same geometry as that defined by the cages themselves. Every atom in this framework is equally accessible on both sides of the monolayer surface, which defines the cage network. It is in every sense a 3-D surface with a surface area of >700 m^2/g^{-1}.

The zeolite cage and channel structures have been extensively summarized by Smith (43) and are illustrated in Figs. 6 and 7. There are a relatively small

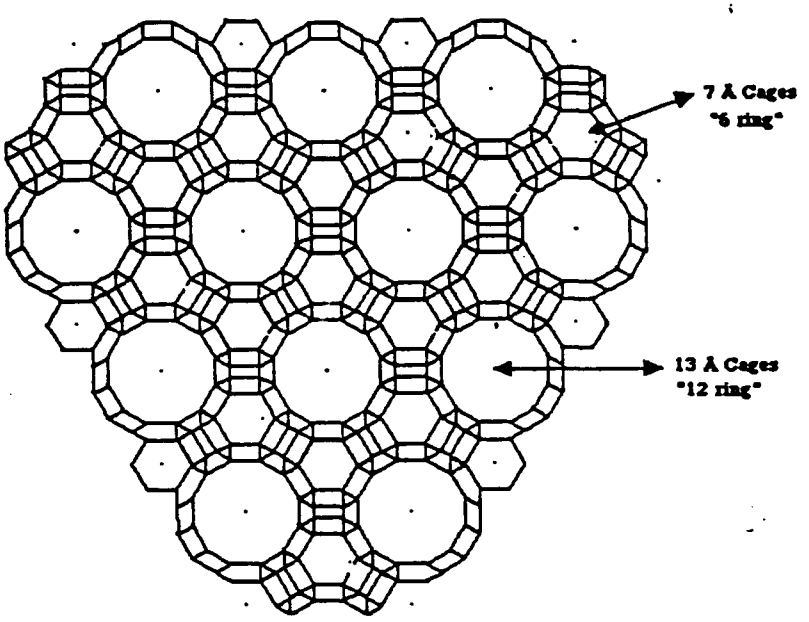

Figure 4. (111) plane of zeolite X or Y showing 13 Å α (supercage) and 7 Å β (sodalite) cages.

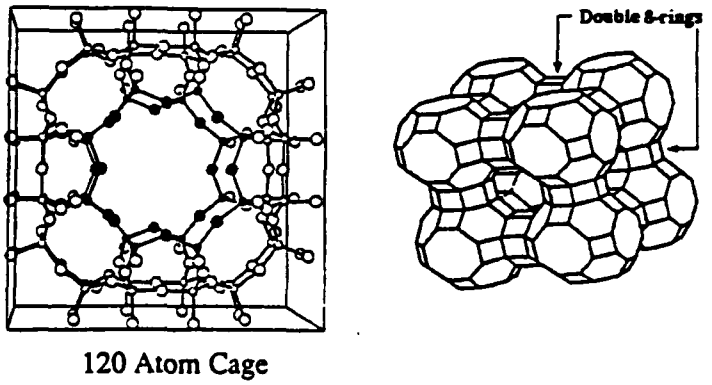

Figure 5. 120 atom cage structure of zeolite RHO in its highest symmetrical configuration, space group *Im* $\overline{3}m$. *Note*: two sets of noninterpenetrating pore systems separated by a monolayer of aluminosilicate atoms.

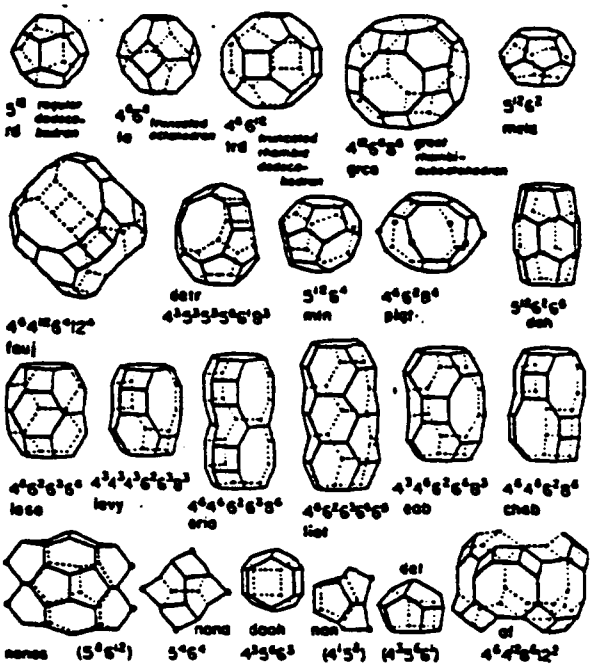

Figure 6. Zeolite structure cages. The nomenclature is (size of ring)^(number of rings), for example, 5^{12} implies twelve 5-rings make up the polyhedron (43).

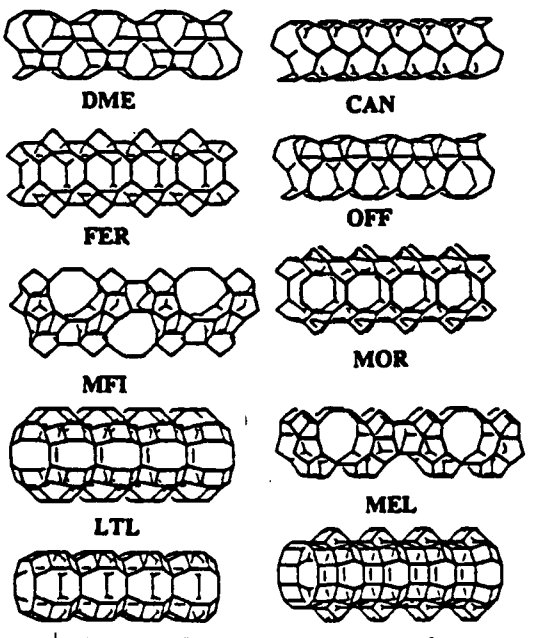

Figure 7. Zeolite structure channels (43).

number of noncentrosymmetric zeolite structures with disordered Al/Si siting in the framework.

B. Molecular Sieves and Tetrahedral Atom Open Framework Hosts

The discovery of molecular sieves containing only silicon atoms in the late 1970s (44), aluminum phosphate (45, 46), silicon aluminum phosphates, and metal aluminum phosphates (47–53), in the 1980s were particularly important breakthroughs in the transition from zeolite to molecular sieve chemistry. This opened a window for entirely new channel and cage structures. Some important examples are shown in Figs. 8 and 9. All of the channel AlPO's shown are

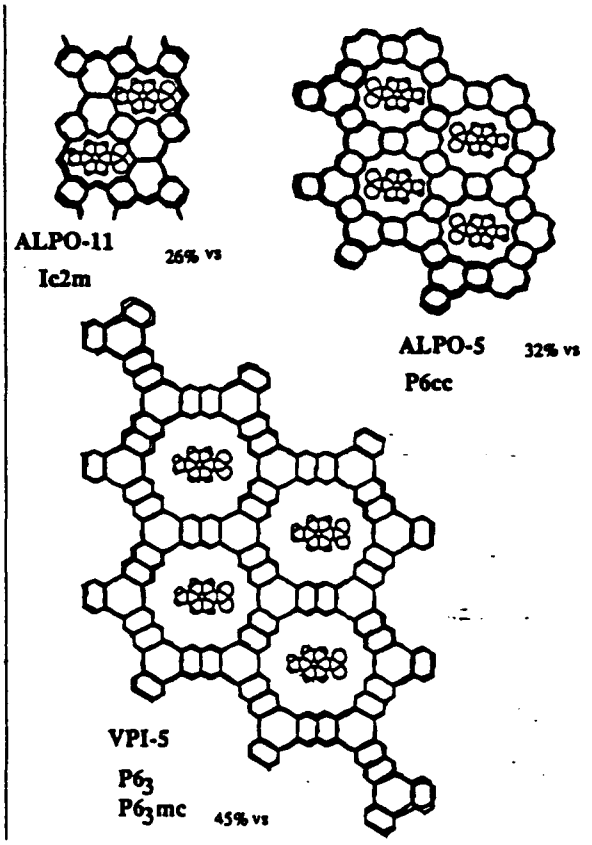

Figure 8. Aluminum-phosphate channel structures for ALPO-5, ALPO-11 (45), *p*-nitroaniline VPI-5 (54a). A molecule of *p*-nitroaniline is included for reference to show the relative differences in channel dimensions. Note that the elliptical shape of the channel of ALPO-11 space groups and percent void space are indicated.

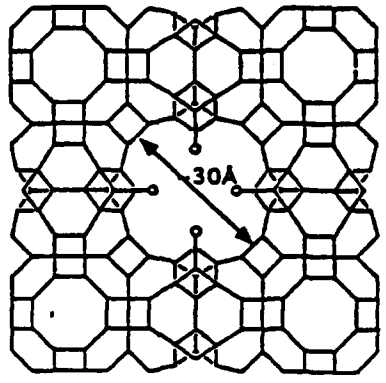

Figure 9. Cage structure of the gallium–phosphate molecular sieve, cloverite. (Reprinted by permission from *Nature*, vol. 352, p. 320, copyright © 1991 Macmillan Magazines Ltd.)

noncentrosymmetric with polar channel axes (Fig. 8). Currently, it is not clear what the ultimate cage and channel diameters might be. Known cages and channels, which make up zeolites, have free diameters of up to 12 Å such as those found in zeolite Y (39, 55). The natural mineral cacoxenite, an iron-aluminum phosphate, possesses 15-Å channels. The largest AlPO channel currently synthesized is VPI-5 (54) with about 13 Å 18-ring openings. This record was recently surpassed by the synthesis of a gallium phosphate, cloverite, which has 20-ring channel openings and a supercage with a diameter of about 30 Å (56) (Fig. 9).

A priori one might think that somewhat larger channel and cage structures would result from using larger atoms in the framework. More specifically, framework atomic radii in $Na_3/(ZnAsO_4)_3 \cdot 4\ H_2O$ (57) are 0.60 Å (Zn^{2+}) and 0.34 Å (As^{5+}) [cf. 0.47 Å (Ga^{3+}) and 0.39 Å (Ge^{4+})] so that one might expect to obtain for a given zeolite structural analogue the largest known pores and channels with the zinc arsenates. Structural parameters are given in Table I for (a) a series of "empty" cage sodalite analogue structures containing three molecules of water, (b) an example of a dehydrated empty cage, and (c) an anhydrous sodalite with a hydroxyl group at the center of the cage. Various framework compositions are indicated.

It is clear that increasing the atomic radii of the framework metal atoms gives neither a larger cage nor a pore opening. This is indirectly evident from the lattice parameters for the cubic unit cells of the sodalite analogue systems, and specifically is reflected in the decrease in the T—O—T′ angles as the atomic radii increase (Table I) (58). The term A is the area of the triangle of oxygen atoms that define the 6-ring pore openings of the sodalite cage. A, and therefore the pore openings, *decrease* in size with increasing atomic radii. Structurally as the T—O bond length increases, the T—O—T′ angle decreases. This accordionlike behavior means that there is little change in the unit cell dimensions

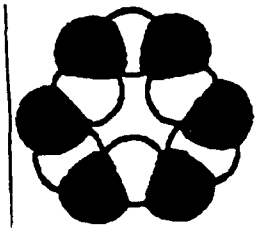

TABLE I

Composition	a(Å)	Θ(T−O−O′)°	A(Å²)	δ Na-Ring (Å)
$Na_3(AlSiO_4)_3 \cdot 4\ H_2O$[a]	8.848(1)	136.2(3)	5.575	1.53(1)
$Na_3(ZnPO_4)_3 \cdot 4\ H_2O$[b]	8.8281(1)	126.1(3)	5.280	1.66(1)
$Na_3(AlGeO_4)_3 \cdot 4\ H_2O$[c]	8.964(1)	129.6(2)	5.399	1.61(1)
$Na_3(GaGeO_4)_3 \cdot 4\ H_2O$[c]	9.003(1)	125.5(2)	5.172	1.68(1)
$Na_3(ZnAsO_4)_3 \cdot 4\ H_2O$[b]	9.0273(1)	123.8(3)	4.741	1.73(1)
$Na_3(AlSiO_4)_3$[a]	9.122(1)	156.3(6)	8.288	0.24(2)
$Na_4(AlSiO_4)_3[OH]$[d]	8.734(1)	132.9(3)	5.37	1.38(1)

[a] J. Felsche, S. Luger, and C. Baerlocher, *Zeolites*, *6*, 367 (1986).
[b] T. M. Nenoff, W. T. A. Harrison, T. E. Gier, and G. D. Stucky, *J. Am. Chem. Soc.*, *113*, 378 (1991).
[c] N. Keder, W. T. A. Harrison, T. E. Gier, C. Zarimba, and G. D. Stucky, submitted for publication, 1992.
[d] S. Luger, J. Felsche, and P. Fischer, *P. Acta Cryst.*, *C43*, 1 (1987).

and a net movement of the oxygen atoms into the void spaces. The results are of interest in light of the argument made by O'Keefe (59) that alumino-silicate structures are determined by T−O bonding and T−T′ nonbonded interactions, not oxygen atom packing, which explains the existence of mineral silicates such as diposide, pigeonite, and clinoenstatite with the same silicon atom arrangement, but differing oxygen atom configurations.

The net empirical charge is kept constant by isovalent substitution as exemplified in an isostructural molecular sieve series containing Al/Si (60), Ga/Si, Al/Ge, and Ga/Ge framework atoms (61). In addition to decreasing the pore and cage dimensions, this substitution accomplishes several things. It changes the average framework electronegativity, the framework electric field, the band structure of the framework, and it modifies the inherent framework polarizability along with the linear and nonlinear optical properties. This has been supported by recent studies of the nonlinear optical response of the four noncentrosymmetric sodalites with the above compositions (61). Second harmonic generation (SHG) measurements performed on the crystalline powders using Ng–Yag 1064-nm radiation showed that substitution of silicon by germanium in $Na_3/(AlSiO_4)_3 \cdot 4\ H_2O$ and $Na_3/(GaSiO_4)_3 \cdot 4\ H_2O$ increases SHG efficiency by a factor of 3, while substitution of aluminum by gallium in

$Na_3/(AlSiO_4)_3 \cdot 4\ H_2O$ and $Na_3/(AlGeO_4)_3 \cdot 4\ H_2O$ increases SHG by only 30%. It can be concluded that substitution at a charge site (AlO_2) introduces less polarization and NLO response than at a neutral site (SiO_2). There is only one nonzero polarizability tensor element $\chi_{(123)}$ in the *P*43*m* point group so that it can be evaluated using powder SHG measurements.

The parameter δ in Table I is the distance of the sodium atom from the plane of the 6-ring tetrahedral atoms. If $\delta = 0$, the sodium atoms no longer have a single cage identity, and are equally shared between adjacent cages. At that point, as far as the sodium atoms are concerned, the structure is an expanded lattice with no definable sodium atom clusters. We return to this point later on.

It should be noted that from the late 1950s–1988, all synthetic molecular sieve and zeolite materials were based on either Group 13 (IIIA) (Al or Ga) and/or Group 14 (IVA) (Si or Ge) metals. A consideration of tetrahedral radii does suggest that other elements might be used (Table II). Recently, the syntheses of zeolite structural analogues containing elements from Groups 2 (IIA) and 12 (IIB) at temperatures as low as −20°C have been reported (57, 62–65). The molecular sieve chemistry of these new framework compositions is extensive. Using only the sodium ion as a template over a pH range from 1 to 13 gives nine different phases within a narrow temperature range of which five are open framework and one contains the $(ZnO)_2PO$ 3-ring configurations. The ZIPO zeolite X structure analogue can be synthesized at −20°C overnight using mixed templates (e.g., sodium and tetramethylammonium halide) and nonaqueous cosolvents. Organic template phases are equally prolific. 1,4-Diazabicyclo[2.2.2]octane (DABCO) gives seven distinct crystalline phases of which five are open framework structures. The zinc open-framework structural field is expanded further when one considers the organophosphonates and phosphites that have been described by Clearfield and co-workers (66, 67) and Mallouk and co-workers (68).

TABLE II
T_d Corner Shared Molecular Sieve Compositions

Groups			Charge	
IV-V	SiO_2	SiO_2	0	Silicalite
III-V	AlO_2^-	PO_2^+	0	ALPO
III-V	$AlO_2^-(SiO_2)_\delta$	$(PO_2^+)_{1-\delta}$	δ	SAPO
III-IV	$(AlO_2^-)_x$	$(SiO_2)_y$	$x-$	Zeolite[a]
IIB-IV	ZnO_2^{2-}	PO_2^+	1−	ZIPO
II-V	BeO_2^{2-}	AsO_2^+	1−	BEASO
III-III	BO_2^-	BO_2^-	2−	Boralite
IIB-IV	ZnO_2^{2-}	GeO_2	2−	ZIGE

[a] For example, offretite (zeolite) = $(K_2Ca)_{2.5}[(AlO_2)_5(SiO_2)_{13}]$

The geometries of molecular sieve channels (Fig. 6) and cages (Fig. 7) are determined by the cation "template" as well as the kinetics of nucleation and solvation effects during synthesis. Sol-gel based syntheses at higher temperatures (>200°C) tend to give more condensed phases with smaller pore dimensions (69). If the temperature is lowered, excessively long crystallization time may be required, for example, for mordenite synthesis 1 h, 2 days, and 4 weeks at 350, 200, and 100°C, respectively (70); for zeolite X, 6 h at 100°C and 800 h at 25°C (71). With increasing hydrothermal synthesis reaction time one obtains the largest pore materials early in the reaction, then with time increasingly condensed phases (72), so that trying to grow larger crystals by slow crystallization during synthesis is usually unsuccessful. Because of the phase transformations, growth of single crystals greater than 100 mm must be carried out by appropriately changing the kinetics of nucleation of the different phases. By carrying out molecular sieve synthesis at lower temperatures one can hope to accomplish several goals: (a) obtain larger pore structural phases, (b) use the solvent or nonaqueous cosolvents as structural templates, and (c) intercept metastable phases that have a short half-life at higher temperatures.

The precedent for *solvent templating* is indicated by the work of Jeffrey in the late 1960s (73). He demonstrated that one could isolate and structurally characterize gas and ion-pair hydrates at low temperatures. An example is tetra(*i*-pentyl)ammonium fluoride, which crystallizes at 31.2°C with an empirical formula $(i\text{-}C_5H_{11})_4NF \cdot 38\ H_2O$. In addition to the utility of tetraalkylammonium fluorides as cosolvent mineralizers in zeolite synthesis (74, 75), their solvent templating ability should be increasingly effective with decreasing temperature. Other nonaqueous cosolvents should be equally effective. These compositional changes in molecular sieve frameworks can serve to improve conditions for single crystal growth, open up the possibility of obtaining new pore topographies with possibly larger dimensions, and modify the electrostatic field of the host.

The recent synthesis and characterization of "holey" silicon (76a and b), with its unusual luminescence properties, suggests that one might use open framework semiconductor structures for electrooptic applications. An intriguing start in this direction is provided by the recent report of metal sulfide-based microporous solids. The materials initially reported are based on germanium(IV), tin(IV) (76c), and antimony(III) (77) sulfide frameworks, synthesized hydrothermally with organic templating agents.

C. Nontetrahedral Atom Open Framework Structures

Nature has provided numerous intriguing examples of open framework structures containing both four- and six-coordinate metal atoms, only a few of which have been successfully synthesized. The octahedral geometry is in general ex-

pected to be less thermally and chemically stable. A nonaqueous solvent approach with organometallic precursors has been used to synthesize hureaulite and alluaudite, two open framework iron phosphates (78). More recently, Haushalter and co-workers (79) described a large number of reduced Mo(IV)–Mo(V) open framework phosphates. Two interesting members of the iron phosphate and arsenate mineral family are the 30-ring channel (free pore diameter 14.2 Å) cacoxenite ($[Al(Al, Fe)_3Fe_{21}O_6(OH)_{12}(PO_4)_{17}(H_2O)_{24}] \cdot 51\ H_2O$) (80), and the smaller 8-ring channel pharmacosiderite [$KFe_4(OH)_4(AsO_4)_3 \cdot 8\ H_2O$] (81) (Fig. 10). The latter is another example of a cluster of cages; the cages in this case being the M_4X_4 cubane structure (82, 83). These have been synthesized as $M_4Ge_7O_{16}$ (M = Li, Na, K, Rb, Cs, or H); $M_4(TiO)_4(SiO_4)_3$ (M = K, Na, or H); $M_4(TiO)_4(GeO_4)_3$ (M = K or H), and $(K, H)_5(FeO)_4(AsO_4)_3$ (61). In all cases there are 7–8 water molecules associated with the empirical formula.

In fact, coordination numbers higher than four are found even in aluminosilicate zeolite and aluminum phosphate chemistry. Dehydration and calcination followed by rehydration frequently results in the generation of aluminum atom coordination numbers higher than four in aluminum silicates. Both four- and six-coordinate aluminum are found in the structure of VPI-5 (56). Gallium phosphate zeolite structural analogues prepared in the presence of fluoride ion have been shown to contain five-coordinate gallium, with the fluoride atom in the center of double 4-ring cages (84).

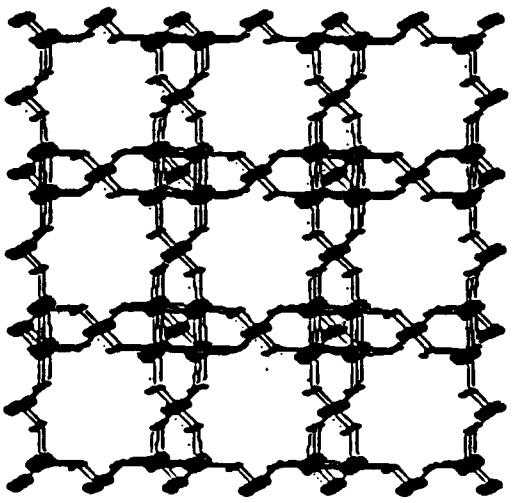

Figure 10. Pharmacosiderite, $Fe_4(OH)_4(AsO_4)_3H \cdot (H_2O)_5$ (81).

Hofmann-type inclusion compounds, for example, the prototype $Ni(CN)_2 \cdot NH_3 \cdot C_6H_6$ (85), with rodlike or aromatic bifunctional bridging ligand groups being used to create scaffolding for guest molecular inclusion, can be made in a variety of configurations with a large range of cavity and pore sizes (27, 86, 87). A recent example is the reaction of PdL (H_2L = 5,10,15,20-tetra(4-pyridyl)-21 *H*,23 *H*-porphine) with excess $Cd(NO_3)_2$ in H_2O—MeOH—EtOH to yield crystals of (PdL) · 2 $Cd(NO_3)_2 \cdot n\ H_2O$, a new type of infinite 3-D open framework. One can envision using these lattices to create nanoengineered redox materials, which take advantage of transition metal and organic bridging ligand electron-transfer properties as modified or utilized by solvent guest inclusion molecules.

D. Other Large Channel Systems

It has been known for some time that varying the degree of misfit between two structurally bonded layers (88–91) will convert planar 2-D layers into a tubular or alternating wave morphology. For example, $Mg_3Si_2O_5(OH)_4$ is structurally formed from a layer of magnesium atoms that is octahedrally coordinated and a layer of silicon atoms that is tetrahedrally coordinated. The Si layer has a smaller repeat dimension than the Mg layer. The mismatch between the two is overcome by bending with the Mg layer on the outside of the curve. The ideal radius of curvature has been estimated to be 88 Å for the strain free composition, $Mg_3(Si_2O_5)(OH)_4$.

Since the strain free radius is determined by the degree of misfit between the Si layer and the Mg layer, substitutions of atoms of different radii can cause considerable variation in pore diameter. Synthetically controlling the composition allows one to tailor fiber bundles to specific radii within which to construct quantum wires. For example, the chemical composition of aluminum substituted materials can be described by the general formula $(Mg_{3-x}Al_x)(Si_{2x}Al_x)O_5(OH)_4$, where $x > 0.125$ gives rise to a planar structure while $x < 0.125$ results in the tubular structure. A Mg/Ge combination gives a planar layer structure, while Si/Al gives a structure of negative curvature from that of Si/Mg. Corrugated and wavelike structures are also feasible with appropriate compositions.

In nature there are a variety of minerals that have planar (lizardite or amesite), alternating waves (antigorite) and cylindrical (chrysotile) morphologies. Electron microscopy studies of chrysotile fibers show that they consist of curled layers that form concentric cylinders with typical dimensions of 220–270 Å for the outer diameters and 70–80 Å for inner diameters (92). It is not uncommon to find a bundle consisting of almost uniformly sized (within a few angstroms) tubular monofilaments. The typical length of the naturally occurring fibers is of the order of several centimeters.

E. Nonlinear Optic Hosts—$KTiOPO_4$ Structural Family

An especially commercially important host for electrooptic applications is the titanyl phosphate $(TiOPO_4)^-$ host lattice of the $KTiOPO_4$ (KTP) structural family. The host-guest properties of KTP make it possible to design and synthesize a large structural field (currently over 50 members) to fine tune and modify optical properties (11). Like all crystalline phases that show second-order nonlinearity, KTP is noncentrosymmetric, crystallizing in the orthorhombic space group $Pna2_1$. The unit cell asymmetric unit is $(KTiOPO_4)_2$ so that there are two unique crystallographic sites for each atom in the atomic formula. The potassium atoms can be reversibly ion exchanged and gas-phase modification of $HTiOPO_4$ with small molecules such as H_2O or NH_3 is readily achieved (93). Because all of these atoms are in general positions, this ion exchange chemistry can be carried out with site selectivity for the two independent guest positions. These sites also can be varied by changing the cation guest. In addition to using this inclusion chemistry, the optical and physical properties can be modified by isomorphous substitution into the host $(TiOPO_4)^-$ framework.

The Ti—O units like together to form a helical chain along [011] with these bridging titanyl oxygen atoms trans for one of the two structurally independent titanium atoms and cis for the other titanium atom. For each titanium atom there is a short (<1.75 Å) "titanyl" Ti—O bond trans to a long (>2.10 Å) Ti—O bond. This long bond is to a titanyl oxygen atom in the trans Ti—O linkage and to a phosphate oxygen atom in the cis titanyl linkage (Fig. 11). The framework TiO_6 chains are linked together by phosphate bridges (*right*, Fig. 11). The open nature of this framework allows cations to diffuse parallel to [001], which is also the polar axis. This ease of diffusion, with ionic conductivities ranging

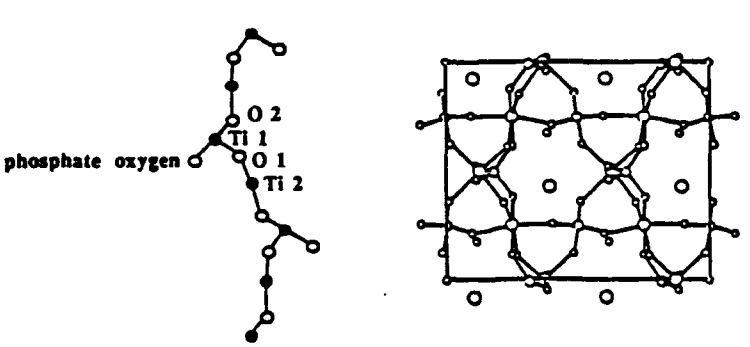

Figure 11. Potassium titanyl phosphate (KTP) structure. Helical chains (*left*) of titanyl (TiO) are linked together by phosphate groups. Ti 1 and Ti 2 are coordinated cis and trans by titanyl oxygen atoms, respectively.

from 10^{-6} to 10^{-10} $(\Omega\ \text{cm})^{-1}$, depending on the method of synthesis and defect chemistry (94, 95) allows both ion exchange (96) and gas-phase desorption and resorption to take place (93).

III. THE HOST-GUEST RELATIONSHIP

The above description of hosts is based on composition and static structure, an implied offer of "this is what you get" to any guest that happens to come along. Fortunately, life is not so simple, and, as suggested above, a much better perspective is a dynamic point of view in which the host and guest properties are considered in relation to the effect that each has on the other. For example, the cavity electric field in zeolite changes with the type of cation that is exchanged into the zeolite and how it is sited. The host "static" structure itself is a zeroth-order approximation that can be strongly affected by the type of guest, the number of guest atoms or molecules, and external environment such as temperature. Perturbation of the host at a specific site is felt throughout the 3-D surface continuum, sometimes leading to a collective response. This section considers some of the properties of the host and guest, which are accessible variables modified by the presence of the guest or host, respectively.

A. Host Variables in Interface Dynamics

1. Three-Dimensional Surface Electric Fields

Whether the goals are to carry out self-organization on a 3-D surface or use guest atoms to perturb that surface, a knowledge of the potential properties of the surface continuum is essential. Efforts to parameterize the potential parameters for inorganic matrices is considerably behind that for organic molecules so that ab initio quantum mechanical calculations of the interaction of an atom or molecule with a 3-D surface are in the initial stages of being tested against experiment (97–106). Some attempts have been made to use a periodic treatment for extended lattices, for example, in the program CRYSTAL (107). Its application, however, has been limited to simple zeolites with an all silica (SiO_2) framework. Furthermore, gradient techniques are not available so that most of the reported efforts have been with finite models.

In general, for the finite model a classical force field:

$$V_{\text{total}} = V_{\text{bond stretch}} + V_{\text{bond angle bend}} + V_{\text{torsion}} + V_{\text{Lennard-Jones}} + V_{\text{electrostatic potential}} \quad (1)$$

is assumed. The electrostatic interaction potential for the framework requires atomic charges as parameters, regardless of the form of potential that is used. Electronegativity equalization, CNDO and INDO semiempirical and SCF-Mulliken have given atomic charges for the silicon atom that range from 0.4 to 1.91 (108–111). For example, the variation in SCF-Mulliken charges for silicon in a given silicate is 0.69–1.1. The interaction of molecules or atoms with the surface is then due to electrostatic and dispersion interactions, typically calculated using Lennard-Jones type of potential. In spite of the uncertainties evident in the literature for obtaining a quantitative formulation and parameterization to describe the potential surface, some optimism is warranted in view of the intense efforts currently being made to experimentally and theoretically establish a predictive model for open cage structures.

Experimentally, it is well established that the electrostatic field within zeolite or molecular sieve cavities are large and can be used in dramatic ways to modify the chemistry (112–116). Some of the earliest estimates of these fields at cation sites in zeolites were made by Dempsey (117) (Table III). The magnitude of these fields was used to explain the reason (a) NO disproportionates as shown below, even though the net free energy for this reaction under standard state conditions is positive, and (b) the ease with which NaCl can be introduced into the zeolite cage 300°C below its melting point (118).

$$4\ NO \longrightarrow NO^+ + NO_2^- + N_2O \tag{2}$$

$$NaCl \xrightarrow{500°C} Na^+ + Cl^- \text{ (mp 801 °C)} \tag{3}$$

A more recent example, which demonstrates the importance of cage potential fields on inclusion chemistry, is shown by the ability to form cation radicals of the polyenes within Na-ZSM-5 (119). The effective emf potential of the zeolite is 1.65 V versus SCE. The most probable source of this effective potential is from the generation of cationic Lewis defect sites by dehydroxylation of the zeolite framework. An important point to be made for this discussion is that electrostatic fields can be large and dominate self-organization and assembly within a zeolite cage.

TABLE III
Aluminosilicate Cage Electric Fields ($V/Å^{-1}$)

	Site II Cation (Å)			Site III Cation (Å)		
Zeolite	1	1.75	2.5	1	1.75	2.5
NaY	2.4	0.94	0.43	3.2	1.3	0.64
CaY	6.4	3.2	1.8			

2. *Framework Flexibility*

Shape selectivity in molecular sieve catalysis and absorption has been extensively studied [see, e.g., (120)] and delineates the precision with which molecular recognition and self-assembly can be achieved. The effect of pore diameter on molecular diffusivity and energy of activation of diffusion is shown in Fig. 12 (121). The exact quantities depend on the topography and polarity of the sorbate species, the potential surface of the molecular sieve, and temperature; however, the general trends shown should be universally relevant in nanoscale self-organization in 3-D channels and cages. The areas of specific interest to this chapter are the nearly vertical regions in which small changes in pore dimensions can cause large changes in diffusivity or energy of activation. Moore and Katzer (122) suggested that for a given molecular diameter, a change of 0.5 Å in the difference between the effective pore diameter and molecular diameter would result in a change of one to two orders of magnitude in the diffusivity. This kind of sensitivity in atomic and molecular recognition is precisely what is needed in order to create the uniformity in size and dispersion of atomic clusters in photonic applications such as that described in the introduction (123). The cage and channel sizes in molecular sieves can be significantly altered by the guest. Conversely, the local geometry of a given cluster, including bond lengths, can be changed by relatively small variations in the cage dimensions. The sodalite cage structure is one of the simplest in the zeolite family and serves as a good example to illustrate these points.

As a 60-atom cage with sufficiently large windows to permit reversible inclusion, it is of some interest to review the molecular and atomic species that

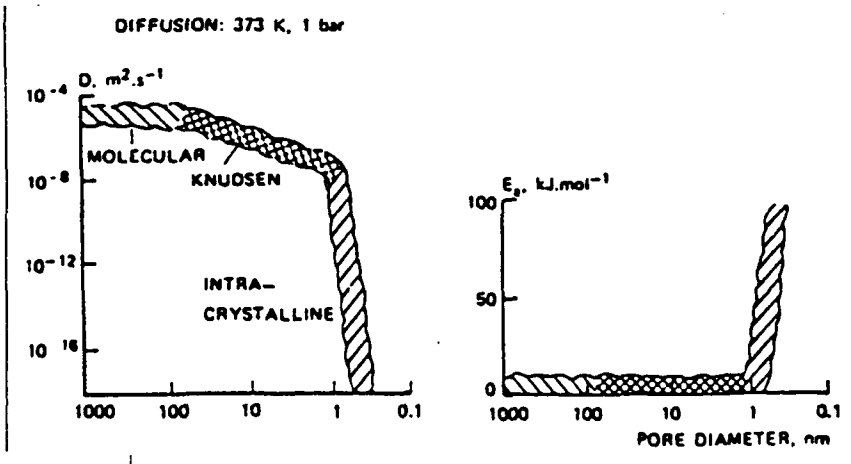

Figure 12. Molecular diffusivity and energy of activation (121).

TABLE IV

Number of Atoms	Examples
3	Na_3 "Empty Cage"
4	Na_4
5	Cd_4Te
5–7	Na_4S_x $x = 1$–3
8	Cd_4S_4
9	Na_4MnO_4
13	$Na_4Al(OH)_4$
15	$Na_3(H_2O)_4$

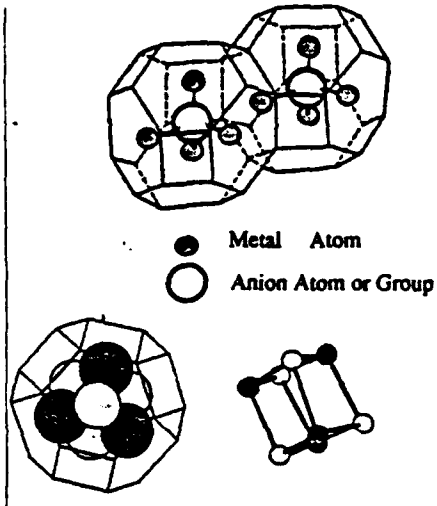

can fit inside this cavity (Table IV). An example is the 8-atom cubane-like cluster formed by cadmium sulfide in the sodalite (β) cages of zeolite Y (124). The compound Na_4ClO_3 is an 8-atom cluster found in the sodalite cage with a different geometry, that is, a cubane-type structure with one oxygen atom missing from a corner site and a chlorine atom at the center (125). The 5-atom M_4X cluster is present as Zn_4S in $Zn_4S(BeSiO_4)_3$ (126) and discussed in more detail below. One can have at least 9 nonhydrogen atoms, or as many as 17 atoms, if hydrogen atoms are included within a sodalite cage.

The term "empty cage" is used here to refer to structures that do not contain atoms *at the center of the cage*. This is denoted in empirical formulas by [ ], for example, $Na_3[\ ](AlSiO_4)_3$ for an "empty" cage containing Na_3, versus $Na_4Br(AlSiO_4)_3$ for a "filled" cage containing Na_4Br. Empty cage structures can be made by direct synthesis or by the reactions indicated below (i.e., starting with a sodalite that has a hydroxide group at the center of the cage) in which sodium hydroxide is removed by extraction to give "empty cages" containing three sodium atoms (127)

$$Na_4[OH](AlSiO_4)_3 \xrightarrow[\text{soxhlet}]{} Na_3[\ ](AlSiO_4)_3 + NaOH \quad (4)$$

$$Na_4[OH]_x[Br]_{1-x}(AlSiO4)_3 \longrightarrow Na_{4-x}[\ ]_x[Br]_{1-x}(AlSiO_4)_3 + x\ NaOH \quad (5)$$

Alternatively, a specified number of empty and filled cages can be synthesized by starting with a material that has some cages containing hydroxide and others

containing the desired atoms. Hydroxide extraction then will leave the desired fraction of cages filled with the cluster surrounded by empty cages.

Numerous other cage geometries and charges are accessible, such as the 4–9 combination, $Na_8[SO_4]/(AlSiO_4)_6$ (128) (an equal number of cages containing 4-atom and 9-atom clusters), the 5-atom mixed cluster of $Zn_3GaAs(BO_2)_{12}$ (129), and clusters designed for ternary metal atom cages as in $[(CH_3)_4N]$-$(MgAl_2P_3O_{12})$ (130).

Upon dehydration of $Na_3/(AlSiO_4)_3 \cdot 4\ H_2O$ there is a dramatic framework displacement of the 60-atom cage. The area of the pore opening increases 80% so that the structure becomes much more permeable. The T—O—T′ angle increases 20° in going from $Na_3/(AlSiO_4)_3 \cdot 4\ H_2O$ to $Na_3/(AlSiO_4)_3$ and the sodium atom moves to within 0.24 Å of the center of the pore opening. This means that 0.24 Å is the displacement required for the Na_3^{3+} cluster identity to be lost and the structure to be transformed into an expanded Na^+ lattice with sodium ions equally shared in the windows between cages. The sodium atoms can be pulled back into a given cage by placing within the cage a charged species such as the hydroxyl ion. The consequence of this is a smaller T—O—T′ angle and a smaller 6-ring pore opening (Table I).

Other ways of varying the framework geometry are shown in Table V. For example, placing a relatively large atomic group such as MnO_4^- (61) at the center of the cage increases the pore size opening and moves the sodium atoms towards the center of the 6-ring opening. Taylor and co-workers (131) carefully modeled this anion size control of the sodalite structure. The metal atoms at the 6-ring sites are also closer to the expanded lattice positions in the sodalite analogue structures, which have small cages because of small atomic radii [0.11

TABLE V
II-VI, III-V, and II, III-V Clusters

Lattice[a]	M—X (Å)	Cage-to-Cage (Å)
Zn_4S B	2.260(3)	6.61
Zn_4S H	2.346(2)	7.03
Zn_4S HG	2.345(3)	7.16
Cd_4S H	2.471(3)	7.31
Cd_4S HG	2.508(4)	7.46
Zn_4Se B	2.368(3)	6.66
Zn_3GaP B	2.202(2)	6.59
Zn_3GaAs B	2.299(2)	6.64
	Bulk	
ZnS 2.34	CdS 2.52	GaP 2.36
ZnSe 2.45	CdSe 2.62	GaAs 2.44

[a] B = Boralite = B_6O_{12}; H = $Be_3Si_3O_{12}$; HG = $Be_3Ge_3O_{12}$.

Å (B^{3+}), 0.27 Å (Be^{2+}), and 0.17 Å (P^{5+})]. With careful diffraction measurements the variation in cell dimensions frequently can be used to monitor guest occupancy.

The most dramatic case of framework flexibility in a 3-D surface is found for zeolite RHO (132–134). Zeolite RHO has an unusual 3-D monolayer surface with a topology that gives equal access to either side of the surface (Fig. 5). Since there are no supporting structural subunits, for example, smaller cages or channels, RHO exhibits atypical framework flexibility with large displacive rearrangements. In the case of other cation-substituted zeolites, charge compensation may produce lattice strain sufficient to promote decomposition of that zeolite under mild conditions. By virtue of its flexibility, the RHO framework is able to distort and relieve the strain imposed by the charge-compensating ions.

The cubic unit cell of RHO for a given aluminosilicate framework composition can be varied from 13.9645(7) to 15.098(2) Å by cation inclusion. The normally cylindrically shaped pore opening at large unit cell sizes is distorted into an elliptical geometry (Fig. 13). The distortion can therefore be characterized by a parameter Δ, which is essentially the difference between the major and minor axes of the ellipse. The parameter Δ varies from 0 to 2.5 Å as the cubic unit cell lattice parameter changes from 15.098(2) Å to 13.9645(7). The pore is defined by "double 8 rings" that is, two 8 rings that are directly connected through oxygen atoms (Figs. 5 and 13). The distortion or ellipticity of the double 8 ring is such that the major elliptical axes of the two 8 rings are orthogonal to each other. For other zeolites, control over ring aperture dimensions is achieved typically using different sized cations as in zeolites 3A, 4A,

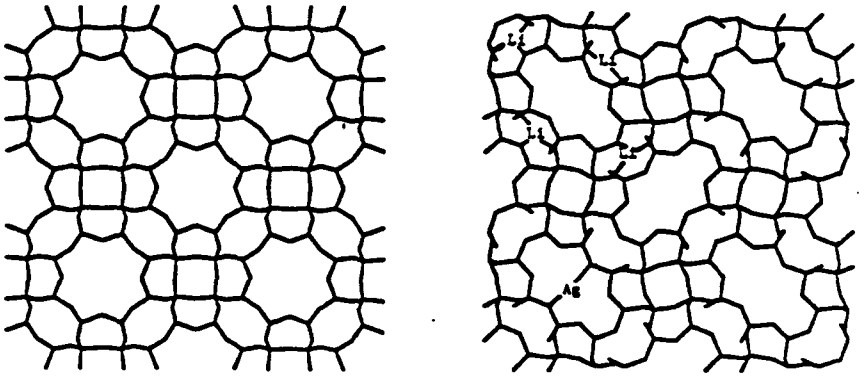

Figure 13. Framework flexibility of zeolite RHO structure. Distortion can be introduced by cation siting at 6 rings (Li) or 8 rings (Ag or Ca). [Reprinted with permission from D. R. Corbin, L. Abrams, G. A. Jones, M. M. Eddy, W. T. A. Harrison, G. D. Stucky, and D. E. Cox, *J. Am. Chem. Soc.*, *112*, 4821 (1990). Copyright © (1990) American Chemical Society.]

and 5A where the cations K^+, Na^+, and Ca^{2+} eclipse the ring opening to varying degrees depending on their size and population. For zeolite RHO, however, it is the framework itself that distorts to modify the cage openings.

This control of cage openings by distortion of the surface continuum can be done in two ways (Figs. 13 and 14). If the cation chooses to site on one of the 8-ring openings as illustrated for Ag^+ in Fig. 13 or, inside the double 8 rings as shown for the tetrahedrally coordinated Ca^{2+} in Fig. 14, the host framework is distorted but the pore is blocked by the cation. If the cation chooses an alternative 6-ring site, however, the framework is distorted in the same fashion while retaining complete pore access. As shown in Fig. 15, the response of the framework is determined by the charge density of the cation, except for the "soft" cations, Ag^+ and Cd^{2+}. As the charge density of the substituted cation increases the unit cell becomes smaller and Δ becomes larger. This remarkable degree of control over pore size opening by framework atom displacement without cation siting within the diffusion pores is unprecedented in molecular sieve chemistry. It is indeed interface control by selective guest siting.

One other challenge for theorists comes out of this study. Theoretical modeling and analysis of experimental data for atomic or molecular absorption and self-organization within a 3-D surface still almost universally assume that the

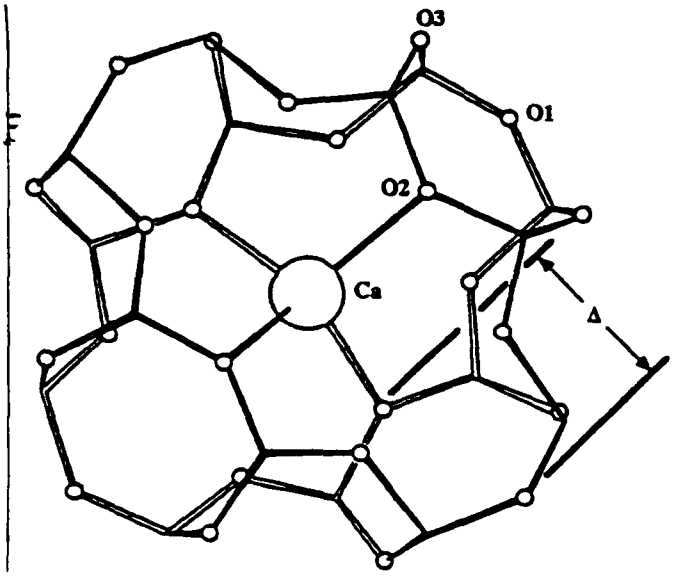

Figure 14. Double 8 ring with tetrahedral calcium atom in the zeolite Ca RHO. [Reprinted with permission from D. R. Corbin, L. Abrams, G. A. Jones, M. M. Eddy, W. T. A. Harrison, G. D. Stucky, and D. E. Cox, *J. Am. Chem. Soc.*, *112*, 4821 (1990) Copyright © (1990) American Chemical Society.]

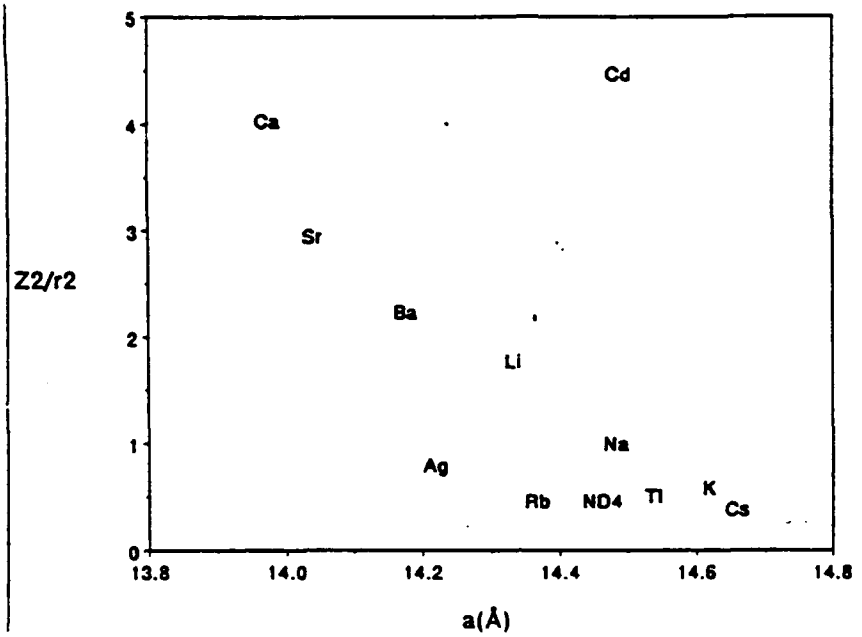

Figure 15. The square of the cation charge density (Z^2r^2) plotted against the unit cell edge for ion exchanged zeolite RHO. [Reprinted with permission from D. R. Corbin, L. Abrams, G. A. Jones, M. M. Eddy, W. T. A. Harrison, G. D. Stucky, and D. E. Cox, *J. Am. Chem. Soc.*, *112*, 4821, (1990). Copyright © (1990) American Chemical Society.]

host framework is rigid and that the bond lengths of the atoms within the framework are invariant with absorption (105, 135). This system presents a unique opportunity to examine the implications of this assumption with a fixed framework composition. Figure 16 shows the variation of the average T—O bond length (T = Si or Al) versus average T—O—T angle. The average T—O—T angle varies from 130 to 150° with an associated small but significant change of 0.02 Å in average T—O bond length. The RHO example of framework distortion is an exceptional example of the reality that guest-host interactions are key variables in controlling chemistry, orientation, and self-organization in 3-D inclusion chemistry.

3. *External Tuning of Host Response by Temperature, Pressure, and Electric Fields*

Host composition, topography, dielectric properties, and flexibility are in some cases a sensitive function of the external environment. Dehydroxylation or solid state phase transitions can change composition. In the case of ferroelec-

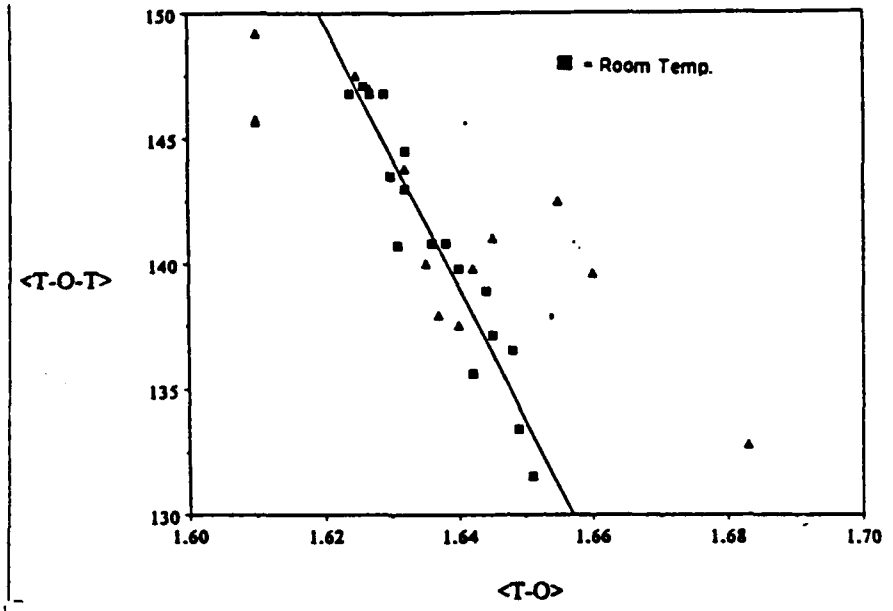

Figure 16. Effect of framework distortion on mean bond length and mean bond angle for zeolite RHO. [Reprinted with permission from D. R. Corbin, L. Abrams, G. A. Jones, M. M. Eddy, W. T. A. Harrison, G. D. Stucky, and D. E. Cox, *J. Am. Chem. Soc.*, *112*, 4821, (1990). Copyright © (1990) American Chemical Society.]

trics framework displacements as a function of temperature lead to a paraelectric phase transition (136). Abrahams and co-workers (137) have studied a large number of ferroelectrics and established that the Curie temperature T_C is proportional to the square of the displacements of the atoms from their positions in the prototypic high-temperature phase. An intriguing pressure driven sequence of the potassium titanyl phosphate phase transitions, ferroelectric → antiferroelectric → paraelectric has been reported by (138). The Raman spectroscopy studies show a first-order transition at 55 kbar, which is driven by an A_1 phonon mode at 56 cm^{-1} for the ferroelectric → antiferroelectric transition and an antiferroelectric → paraelectric transformation at 90–100 kbar. I initiated the structural mapping of this mode with Bob Hazen of the Carnegie Geophysical Laboratory. Our results to date show a unique softening of the lattice as the phase transition is approached, which is reflected in the angular displacement of a titanium octahedron with respect to a phosphate tetrahedron. For example, a single Ti—O—P bond angle changes 6.1° between atmospheric pressure and 10 kbar. The next largest angular distortion is 1.9° between titanium octahedra, while all other angular changes are less than 1°.

The host–guest interface relationship is also clearly evident in the external pressure response of zeolites. The compressibility of zeolite 4A to 40 kbar is dependent on the relative sizes of the hydrostatic fluid molecules compared with the structural channels in the zeolite framework (139, 140). Compression in water is normal, with no observed phase transitions. Compression in alcohols is twice as great as in water, and three volume discontinuities were observed. These volume changes in alcohol were rapid with increasing pressure but sluggish in reverse. High-pressure "phases," all of which are dimensionally cubic, are progressively more compressible at high pressure. These unusual high-pressure phenomena, which indicate significant interactions between zeolite 4A and the hydrostatic media, are consistent with differences in zeolite adsorption of water and alcohols.

The changes in the X-ray diffraction pattern during the deammoniation of NH_4RHO (Fig. 17) (141) and unit cell parameters of Cd^{2+} RHO due to the resiting of cadmium ions in zeolite RHO as a function of temperature (Fig. 18) (134) are not unique. Diffusion activation energies, framework displacement and reconstruction all need to be considered with temperature as part of the synthesis phase space.

The ultimate success in developing nanocomposite materials based on 3-D inclusion will depend on the ability to create homogeneous nanophases throughout the bulk of the material. Direct synthesis with loaded precursors is one approach to alleviating this problem. For example, in the synthesis of semiconductor clusters with organometallic precursors, the siting and loading of the precursors is critical (142). Alternatively, it is necessary to control self-assembly kinetics and diffusion both in and out of the host. This, in turn, is a sensitive

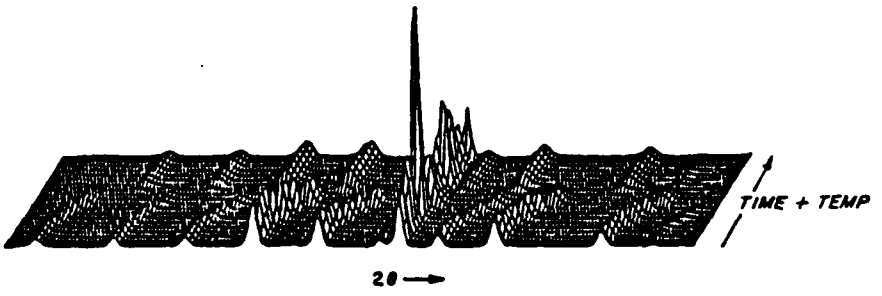

Figure 17. Structural variation of zeolite RHO during deammoniation. [Reprinted with permission from D. R. Corbin, L. Abrams, G. A. Jones, M. M. Eddy, W. T. A. Harrison, G. D. Stucky, and D. E. Cox, *J. Am. Chem. Soc.*, *112*, 4821, (1990). Copyright © (1990) American Chemical Society.]

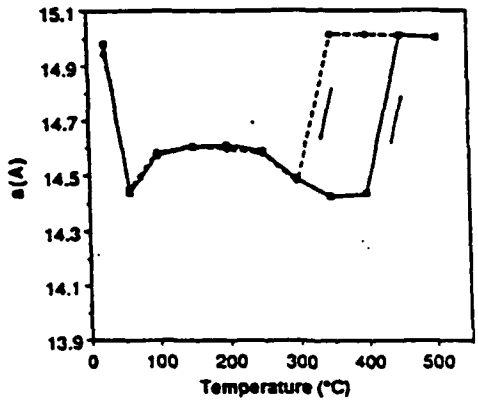

Figure 18. Change in unit cell parameters of cadmium RHO during heating and cooling. [Reprinted with permission from D. R. Corbin, L. Abrams, G. A. Jones, M. M. Eddy, W. T. A. Harrison, G. D. Stucky, and D. E. Cox, *J. Am. Chem. Soc.*, *112*, 4821, (1990). Copyright © (1990) American Chemical Society.]

function of the host–guest interaction and host surface flexibility as a function of temperature.

Electric fields are commonly used in poling ferroelectrics and controlling domain dipole orientation. Similar responses may be useful in inclusion nanocomposite ferroelectric and NLO materials. Recently, electric field alignment of small *crystals* of the polar molecular sieve, $AlPO_4$-5, has been described (143) using an electric field in the kilovolt per centimeter ($kV\ cm^{-1}$) range. The aligned crystals were then fixed in an epoxy resin with suggested potential applications as molecular sieve membranes, NLO and media for aligned organic polymers.

4. Guest Modification of Host Electronic and Optical Properties

This is described in more detail in Section IV (Nanocomposite Synthesis and Properties). The structural and bonding interactions, which are introduced by the presence of the guest at the host–guest interface, can be used to modify the host electrooptic properties. Selective siting, guest coordination preferences and the strength of the guest–host bonding can all be used as important tunable parameters in the design of electrooptic materials.

5. Host Surface Reconstruction and Modification

The host can also respond to the guest through framework reconstruction and chemical bond formation. The idea here is to use the host framework as scaffolding on which to carry out self-assembly or as a templating guide for ab-

sorbed molecules. Functionalization of the framework can be carried out by silanation (144, 145) phosphorylation (146), and condensation reactions with metal halides, such as $Cl_2(thf)GeMo(CO)_5$ (147). This is to be contrasted with the use of guest ions to guide or direct self-assembly by guest–guest coordination (148, 149).

B. Guest Variables in Interface Dynamics

In the preceding discussion, examples were given of how the host responds to the guest. How can the host be used to alter molecular or atomic properties, that is, how can guest properties and behavior be modified by the host? Several are obvious, or have been mentioned above:

Pore size constraints to control molecular diffusion.

Provide a large electrostatic field that promotes heterolytic dissociation chemistry.

Restrict possible transition state configurations for guest reaction chemistry.

Absorption site selectivity that differentiates molecules on the basis of their acid–base or hydrophilic–hydrophobic properties.

Molecular dipole orientation.

Provide passivation of coordinatively or electronically unsaturated atomic guest surfaces to give metastable guest species, which exist on a time scale without analogue in the absence of the host.

Modification and definition of guest electronic states, for example, quantum confinement.

1. Exterior Surface–Interior Surface Considerations and Pore Size Constraints

Even though the exterior–interior surface area ratio can be several orders of magnitude, zeolite catalytic selectivity can be greatly improved by passivating the exterior surface to eliminate nonselective reactions in zeolite catalysis. For example, the external acidic sites on the external surface of an acid zeolite react irreversibly with $P(OMe)_3$ via a modified Arbusov rearrangement to form surface-bound $MePO(OMe)_2$ (150). This approach can also be used to microengineer pore size openings.

The host can be designed so that the guest will partially slip into the pores on the exterior surface of a molecular sieve crystalline particle, but not enter the pores. This has been used by Mallouk and co-workers (151–154) in a variety of ways. One of particular interest is the multicomponent molecular electron transport chain composed of EDTA (ethylenediaminetetraacitic acid), Zn tet-

rakis(*N*-methyl-4-pyridyl)porphyrin (I), and methylviologen (II), spatially organized by micron sized zeolite L particles. Compound II ion exchanges into zeolite L while the bulkier I adsorbs only onto the outer surface in an approximate monolayer. At pH 4.0, EDTA is strongly adsorbed onto the I-coated surface. When the composite is prepared from internally platinized zeolite L particles, hydrogen is evolved photochemically from water. The rate of hydrogen evolution depends on the II loading, no H being evolved when there is less than approximately 0.4 II ions per large cavity of the zeolite structure. The triplet excited-state reactivity of I is suppressed by a 200-mV positive shift of its redox potentials caused by adsorption onto the zeolite surface.

In related studies, covalently linked tris(2,2′-bipyridine)Ru(II)-*N*,*N*′-dialkyl-2,2′-bipyridinium ($RuL_3^{2+}-2\ DQ^{2+}$) complexes were ion exchanged onto the surface of zeolite Y and L powders and studied by flash photolysis–transient diffuse reflectance spectroscopy in aqueous suspension. When the zeolites are loaded with a secondary electron acceptor *N*,*N*′-dibenzyl-4,4′-bipyridnium (BV^{2+}), a $Ru^{3+}-BV^{2+}$ transient is formed in 17.5% quantum yield within 100 ns and decays with a lifetime of 37 ± 5 mus. Electron transfer from the RuL_3^{2+} MLCT (metal-ligand charge transfer) state to 2 DQ^{2+} occurs within 5 ns, followed by electron transfer from 2 DQ^{2+} to BV^{2+}. These data suggest that the smaller 2 DQ^{2+} end of ($RuL_3^{2+}-2\ DQ^{2+}$) protrudes into the pores on the zeolite outer surface, making close contact to BV^{2+} molecules inside the zeolite.

In carrying out nanochemistry within the zeolite host, it is useful to know the exterior surface composition. For transition metal exchanged zeolites, exterior surface composition can be tested by simple redox reactions. Platinum can be exclusively deposited on the internal surfaces of zeolite L, using $Pt(acac)_2$ (where acac = acetylacetonate) while a cation-exchange technique using $Pt(NH_3)_4^{2+}$ and subsequent reduction by H_2 or aqueous BH_4^- does not show this selectivity. Catalytic conversion of $Fe(CN)_6^{3-}$ to $Fe(CN)_6^{4-}$ by H_2 only occurs with zeolite L, which is platinized using $Pt(NH_3)_4^{2+}$ and has platinum on the outside of the zeolite and not with L platinized using $Pt(acac)_2$ (155).

The use of zeolite external surfaces as 2-D templates for the self-assembly of polar or organic templates has been recently demonstrated. Atomic force microscopy has been used to map the periodic pore openings on zeolite surfaces and the subsequent absorption of neutral, organic molecules (*t*-butanol), via their polar head groups at channel entrances. Such absorbed molecules could not be rearranged by the AFM tip when used in an imaging mode. Ionized molecules (*t*-butyl ammonium ions), however, could be rearranged when a sufficiently large force was applied to generate a pattern with a room temperature lifetime of at least 30 min (156). The molecule-by-molecule arrangement on and within zeolite surfaces to generate vectorial electron-transfer chains is clearly feasible.

2. *The Host-Guest Interface and Self-Organization*

The key to the self-assembly of molecules or atoms within a 3-D surface is the nanoscale inclusion chemistry at the host-guest interface relative to that associated with guest self-organization (bulk) and guest cluster intrasurface forces. In the case of mercury inclusion, guest intrasurface forces are relatively strong and loading can only be done at high pressures (157), or by breaking the Hg surface structure through alloying with a guest ion such as Ag^+ (158). The self-organization of molecular and atomic clusters within a porous host is a nucleation process with added constraints on the cluster surface introduced by the host geometry and chemistry. A short overview of the factors that must be considered follows.

The thermodynamics of nucleation for the gas-phase self-assembly of a spherical cluster are illustrated in Fig. 19. For any process to proceed spontaneously, the free energy for the change, ΔG_n, where n refers to the nucleation, must be < 0. Since the disorder of the system is decreased during nucleation, the entropy contribution to the free energy change will be unfavorable (<0) and become increasingly so with increasing temperature.

The driving force for the nucleation is the attraction of the atoms or molecules for each other. Ordinarily, this attraction is three dimensional, and has associated with it a decrease in free energy per unit volume, $-\Delta G_v$. For a spherical cluster of radius r, the gain in free energy is then $-(\frac{4}{3})\pi r^3 \Delta G_v$. Opposing this is the cluster surface energy, which makes a positive contribution to the free energy of nucleation. One way to view this effect is that the atoms at the surface interact more strongly with their neighbors than do the atoms in the bulk. In a sense the surface must be weakened and rearranged in order to continue the cluster growth. Denoting the surface free energy change per unit area of the cluster as ΔG_s the net change in free energy during nucleation is

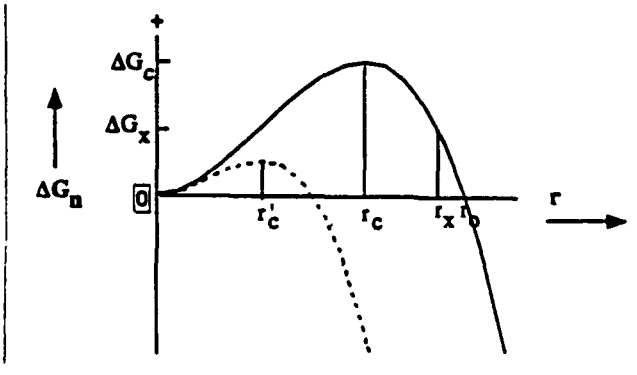

Figure 19. Variation of free energy of nucleation with cluster size.

given by

$$\Delta G_n = 4\pi r^2 \Delta G_s - (\tfrac{4}{3})\pi r^3 \Delta G_v \quad (6)$$

This relationship with $\Delta G_s = \Delta G_v$ is plotted in Fig. 19 (solid line) and reveals several key points. The most important one for our purposes is the critical role that the surface plays in the process of forming a cluster. Initially, the overall free energy for the nucleation is positive, but with increasing radius of the hypothetical spherical cluster, ΔG_n passes through a maximum ΔG_c when the cluster has a radius r_c. As the radius increases, ΔG_n decreases to zero and first becomes negative for $r > r_0$. The significance of this can best be seen by considering the fate of a small cluster with radius r_x. Thermodynamically, this cluster is unstable since $\Delta G_x > 0$. If it were to start to dissolve, however, its radius would decrease and the free energy would become even greater so that it is *kinetically stable*. We conclude that clusters with a radius $r > r_c$ are going to continue to grow. Nuclei with radii $r_c < r_x < r_0$ are called metastable since they require an activation energy $(\Delta G_c - \Delta G_x)$ for their dissolution. Clusters with radii $r < r_c$ are unstable since there is no barrier to their dissolution. Clusters with radii $r > r_0$ are over the hill, that is, stable, since growth to larger clusters is then both kinetically and thermodynamically favored.

One way to stabilize clusters with a smaller radius is shown by the dashed line in Fig. 19. Here the bulk interactions are increased relative to those at the surface, $\Delta G_v = 2\,\Delta G_s$, while for the solid curve it is assumed that $\Delta G_v = \Delta G_s$. Clearly, if the binding energy between atoms in the bulk is increased relative to the surface energy, smaller clusters will be more stable. Another alternative is to "package" the clusters. Chemically, this means that as a cluster is forming the atoms on the surface of the cluster will be capped and passivated with respect to further growth. Thermodyamically, this can be expressed by the addition of another free energy term, $-\Delta G_c$, to the nucleation free energy (Eq. 1) to give:

$$\Delta G_n = 4\pi r^2(\Delta G_s - \Delta G_c) - (\tfrac{4}{3})\pi r^3 \Delta G_v \quad (7)$$

This is accomplished in practice by adding a passivating reactant to the nucleation media (arrested precipitation) or by growing the clusters within a protein or inorganic cavity, the walls of which contain the passivating groups. Another way to view this is by considering the surface as a template for nucleation. In 2-D this is referred to as epitaxial growth, while in 3-D it is sometimes called more euphemistically "ship-in-the-bottle" chemistry.

3. *Nanocluster Guests and Quantum Confinement*

The first question that needs to be addressed in packaging a nanocluster guest is obviously the desired size of the cluster. Because of the many potential applications in electrooptics, semiconductor clusters in which the electrons are

"quantum confined" are highly desirable. A brief definition of quantum confinement is therefore in order.

An important consequence of 3-D packaging of atom arrays for which there is inherently a small energy separation between ground and excited states is the spatial localization of charge carriers. Quantum confinement arises when a photon with energy equal to or greater than the energy gap ($h\nu > E_g$) of a semiconductor induces an electronic transition from the valence to the conduction band (159). Spatially, the electron moves from an atomic site through the lattice via the conduction band orbitals. The positive charge left behind is appropriately called a hole and is weakly bound to the electron over relatively large distance (~ 100 Å). This bound electron–hole pair is called an exciton. It is easier for the electron to delocalize through the lattice if the valence and conduction bands are close in energy since thermodynamically there is not as much to be gained for the electron to recombine with another hole. For this reason the distance of the electron from the hole is inversely proportional to the band gap, E_g.

To a first approximation the exciton can be viewed as the analogue of a simple Bohr hydrogen atom. The electron orbits around the positive charge in the lattice at distances on the order of 20–300 Å depending on the band gap. Quantum confinement occurs when the individual clusters of the semiconductor are the same size or smaller than the exciton radius. The electron finds that it is not free to move as far away from the hole as it would like and the motion of the weakly bound electron–hole pair becomes quantized. The size of the cluster required for quantum confinement in a small bandgap semiconductor such as InSb ($E_g = 0.23$ eV) is on the order of 1400 Å since the exciton electron–hole separation is about this large, while that for a large band gap semiconductor, like CuCl ($E_g = 3.5$ eV), is only about 8 Å. In general unusual optical and electronic properties will be evident at or below these respective radii for these materials.

IV. NANOCOMPOSITE SYNTHESIS AND PROPERTIES USING THREE-DIMENSIONAL SURFACE CONFINEMENT

Nanocomposites based on 3-D host frameworks have been synthesized by (a) direct synthesis, (b) ion exchange chemistry, (c) gas-phase inclusion and subsequent nucleation within the host, (d) liquid-phase inclusion of the guest, (e) gas- or solution-phase inclusion with one or more precursor guest reactants and topotactic synthesis of new guest species within the host, and (f) a combination of (b) and (e). This section focuses on examples of the following types of materials obtained by these synthetic approaches using nanoscale inclusion chemistry: (1) charge carrier cluster guests, (2) oriented and packaged organic NLO active guests, and (3) nonlinear optic framework active hosts.

A. Charge Carrier Cluster Guests

1. Sodalite Based Hosts

The sodalite crystal structure is usually a cubic close packed array of truncated octahedral cages, however, lower crystallographic symmetries including tetragonal, hexagonal, and orthorhombic can be obtained by appropriate framework atom substitutions. Using different atomic group compositions also modifies the cage size, cage electric field, and dielectric properties. Examples of sodalites are known with element compositions from all of the group combinations shown in Table II. Note that the formal sodalite cage charge varies from 0 to −6.

The cages can be considered as potential wells with barriers between the cages dependent on framework dielectric properties (i.e., framework charge and atomic composition). The sodalite cage can be used to build up a 3-D lattice (Fig. 3) by sharing 12 atoms $(Si,Al)_6O_6$ "6 rings" to give a close packed array of truncated octahedra cages (*sodalite*), by coupling with oxygen atoms between the 8 atom $(Si,Al)_4O_4$ "4 rings" (*zeolite A*), or coupling with oxygen atoms between the 6 rings (*zeolite Y*) so that intercage separation is greatly increased. The intercage separation of the close packed sodalite structure also can be changed by varying framework composition. In the following discussion, we review how the cage electric field, the cage geometry, and the intercage separation influence control cluster properties.

a. Alkali Metals. One of the simplest, but most intriguing clusters is synthesized by gas-phase sorption of sodium atoms into the zeolites made up of sodalite cages, for example, Na—Y, Na—X, and sodalite (160, 161). As the sodium is absorbed, into sodalite, the color changes from pale blue, bright blue, blue, deep violet, and finally black. The synthesis temperature for sodium inclusion is between 250 and 500°C. The stability of the fully loaded sodalite is remarkable. Above 500°C, thermogravimetric analysis shows loss of one sodium atom per sodalite cage, a reversible process. Once the metallic sodium is in the sodalite cage no significant change in color is observed with 48-h soxhlet extraction with methanol or 12-h extraction with water. Longer extraction with water causes the sodalite to become progressively violet, red, pink, and ultimately white with a corresponding increase in alkalinity of the water. This ability to form and store reactive species or enhance the lifetime of organic molecules by inorganic packaging is an important attribute for potential technological applications.

Electron paramagnetic resonance (EPR) studies of the sodium sodalite confirm that the electron is delocalized over four sodium atoms in a tetrahedral Na_4^{3+} cluster (162–165). Furthermore, Fourier transform electron spin echo envelope modulation (e.s.e.e.m) spectra show modulations due to the 24 neigh-

boring sodium atoms at a distance of 5.7 Å in adjacent cages (166). From the separation of the hyperfine lines the percentage "atomic character," which is a measure of the occupation of the metal cation ns orbital, is estimated to be 41% for Na_4^{3+} and 80% for K_4^{3+} in sodalite. The increased occupancy for the potassium cluster is attributed to the fact that this cluster is more compressed within the cage (162). The empty cages can also be regarded as defect lattice sites, which can serve as deep traps to capture electrons excited from the valence band to the conduction band. This property has made them useful in cathodochromic and photochromic applications (167–171).

In the larger pore X and Y zeolites the same Na_4^{3+} cluster is formed, however, the color is red. Synthetically, the cluster can be generated by gas-phase inclusion of sodium or a more electropositive element (163) than sodium into the ion exchanged Na-zeolite X or Y, radiation of the ion exchanged Na-zeolite without addition of sodium vapor (172), by treatment of the ion exchanged Na-zeolite with europium metal dissolved in liquid ammonia (173, 174), or by ethanol inclusion of sodium azide followed by controlled thermal decomposition (175). Color centers introduced into the normally optically transparent halogen chlorosodalite, $Na_4Cl(AlSiO_4]_3$ by radiation treatment are thought to be due to the presence of cages with *p*-type defects, that is, $\{Na_4[\ ](AlSiO_4]_3\}^{+1}$. Inclusion synthesis in the larger pore zeolite Y or X gives in addition to the Na_4^{3+} cluster, a larger blue Na_6^{5+} cluster in the supercage at higher loadings as evident by a 19-peak EPR spectrum. It is suggested that these sodium atoms are on the III sites (Fig. 3) in the supercage. Westphal and Geismar (163) synthesized a large variety of alkali metal clusters (type AB_3^+) synthesized by reaction of alkali metal A (Li, Na, K, Rb, or Cs) with the cations B (alkali, alkaline earth, and rare earth metals) of zeolite Y.

The UV–vis absorption spectrum of the Na_4^{3+} sodalite is dominated by an electronic transition between the internal Stark effect broadened ground and first excited state of the Na_4^{3+} cluster. No quantitative measurements were previously reported for the optical properties of this phase, however. In a recent experiment to understand the sensitivity of the absorpton spectrum to the charge distribution on the cage framework, a high-vacuum (10^{-8} torr) apparatus for metal vapor deposition was used to diffuse sodium atoms into the "empty" $Na_3[\ ](AlSiO_4)_3$ sodalite cages and form a series of samples containing different concentrations of Na_4^{3+} clusters (61). At low sodium atom loadings the neighboring cages contain Na_3^{3+} empty cages as opposed to the $(Na_4Cl)^{3+}$ filled cages adjacent to the *p* site $\{Na_4[\ ](AlSiO_4]_3\}$ + vacancies (F centers) in irradiated $Na_4Cl(AlSiO_4]_3$. The absolute absorbance of samples containing approximately one Na_4^{3+} cluster per 50, 10, 4, 2, and 0.67 empty cages contain a prominant peak centered at 628 nm (Fig. 20*a*). This value corresponds to the first excitation band for one Na_4^{3+} cluster per 50 empty cages (Fig. 20*b*).

An absorption maximum of λ_{max} = 530 nm for the Na_4^{3+} cluster of the chlo-

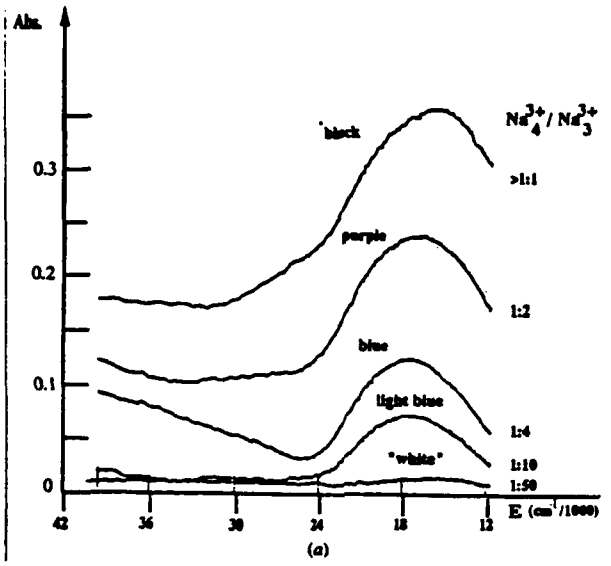

Figure 20(a). Diffuse reflectance spectra of the Na doped $Na_3[AlSiO_4]_3$ sodalite in the 220–850-nm region. The ordinate is given in the absorbance units calculated as $-\log(I/I_0)$, where I is measured intensity of the light reflected from the sample and I_0 is the intensity of the light reflected from the $BaSO_4$ reference powder.

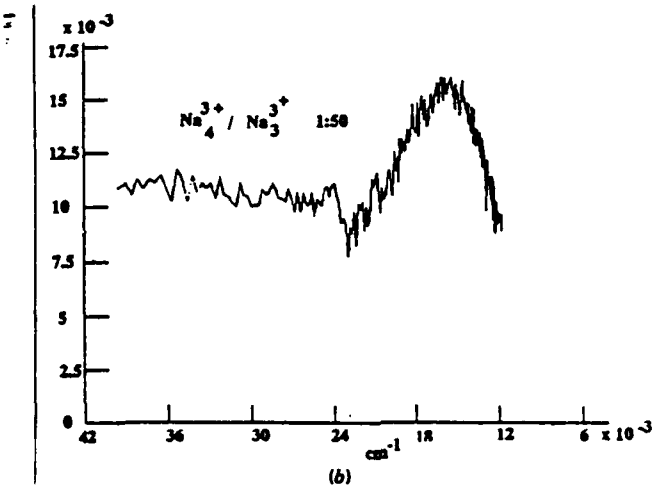

Figure 20(b). Experimental absorption spectrum of the excess sodium in $Na_3[AlSiO_4]_3$ sodalite in the case of "infinite" dilution ($Na_4[AlSiO_4]_3/Na_3[AlSiO_4]_3$ ratio = 1:50). The spectrum is that of the "white" sample shown in Fig. 20*a* with the ordinate expanded by factor of 20.

rine defect sites in $Na_4Cl(AlSiO_4)_3$ is about 100-nm blue shifted from that in the empty cage sodalite. A straightforward explanation for this observation follows from a back-of-the-envelope particle in a box approximation (161, 163). The electron is delocalized in a nearly spherical cage. At a 95% probability of finding the electron in a sphere with a diameter of 6.8 Å, λ_{max} = 500 nm. If the sphere is larger, λ_{max} will substantially increase, for example, for a sphere of 7.6 Å, λ_{max} = 628 nm. Recall from Table I that the unit cell edge for $Na_3[\ ](AlSiO_4)_3$ is 9.122 Å with δ, the distance of the sodium from the 6-ring window being 0.24 Å. For $Na_4Cl(AlSiO_4)_3$, a = 8.879 Å and δ = 1.11 Å (176). This cage coordination effect accentuates the decrease in unit cell size in going from the empty to the chloride filled cage so that the sodium atoms are about 1 Å further into the cage in the chloride sodalite, giving a substantially smaller potential surface for the electron in the cage cavity. It should also be noted that we are dealing with an infinite surface. One cage does not change its geometry unless the surrounding cages cooperatively follow suit. Taylor and Henderson (176) parameterized this nicely in terms of the unit cell dimensions and framework atom tetrahedral tilt angle. At low concentrations of F^- centers the location of the sodium atoms at the vacancy site and the adjacent filled cages are therefore likely to be very nearly the same. The result is an interesting way to tune optical spectra!

Several other questions remain. The particle in a box picture is an oversimplification since the actual probability for delocalization in the cage will depend on the framework atom (Si/Al/O) charges. As pointed out in Section III.A.1, while it is generally accepted that electric fields within sodalites are large and some experimental data exists to verify the magnitude of these fields at cation sites, there is currently little consensus on the potential field of the framework itself. How does the cage electric field affect the optical absorption spectrum?

Time dependent calculations for an electron in the presence of charged atom pseudopotentials to determine the potential well and intercluster coupling for Na_4^{3+} clusters in $Na_{3+x/1-x}[e^-]_x(AlSiO_4)_3$ can be carried out rigorously for this 1 e^- problem (177). The electron dynamics is treated explicitly and the light coupled to the system through the electron dipole operator. This formulation provides the spectrum for the excited states in one calculation. The hypothetical 4-atom Na_4^{3+} cluster in free space would show a single absorption line at approximately 3.2 eV. This line is split into a multiplet by the sodalite cage electric field and by higher energy transitions to the framework states.

As noted in the discussion above, semiempirical calculations (113, 178–180) have been carried out to determine the cage and framework potential of aluminosilicates, with widely varying results for the implied framework atom charges. The optical properties are clearly a sensitive function of charge as shown in Fig. 21 for theoretical results obtained using recently published cage electric field parameters (100, 181, 182) with a fixed polarization direction and

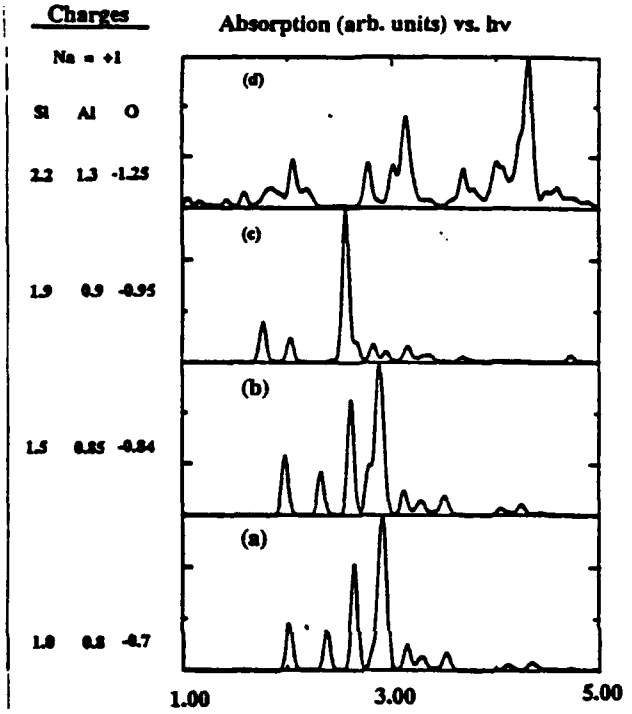

Figure 21. High-resolution absorption spectra of sodalite with the indicated charges for the framework ions.

zeolite orientation. The results can be put in the framework of the probability, P, of finding the electron within the cage volume. For charges Si = +2.2 and Al = +1.3, P is only 0.05. Upper atomic charge limits from these calculations for the sodalite cage are Si < +2 and Al < +1. If the framework charges were higher, the cage electron would be delocalized over the framework. Note that the degree of splitting of the energy bands is determined by the strength of the electric field. The barycenter of the absorption spectrum is determined by the extent of delocalization, which as discussed previously is set by the size of the cage. The theoretical modeling clearly predicts a very strong dependence of absorption band structure on the framework electric field and small displacements of the sodium ions.

In the introduction, the ability to identify and control intercage coupling was stated to be essential in 3-D packaging. Can we learn anything about the potential barriers for intercage electron interactions for an aluminosilicate framework? The spectrum corresponding to the lowest concentration ratio (1:50) is shown on an expanded scale in Fig. 20*b*. This defines the absorption spectrum

of an isolated Na_4^{3+} color center. This localized color center absorption can be normalized and substracted from each of the higher loading curves in Fig. 20*a* and leads to the following observations.

An additional band appears with short wavelength onset in the UV region of the spectrum ($-38{,}000\ cm^{-1}$) as soon as the increasing concentration of sodium atom leads to the formation of Na_4^{3+} clusters in adjacent cages. This leaves the blue portion of the visible spectrum mostly unaffected. This absorption occurs at a cluster concentration that corresponds to the formation of at least one pair of neighboring cages with Na_4^{3+} clusters. Another geometric view of this is as a 3-D network of quasi-1-D chains formed by adjacent cages containing Na_4^{3+} clusters. Calculations of these potentials through different cross sections of the cage walls show unambiguously that as expected the lowest energy path for electron transfer is through the 6 rings of the cages.

The absorption band expands into the IR region with a strong continuous absorption throughout the entire 200–850-nm region as more of the 14 nearest neigbor (eight via 6 rings and four via 4 rings) cages are filled around a given Na_4^{3+} cluster cage, leading at the end to a black metallic material. Although no conductivity measurements were performed on the alkali metal doped sodalites, the sodalite EPR spectrum consisting of the 13 peak hyperfine structure characteristic of the isolated Na_4^{3+} clusters collapses with the increase of the excess Na to a single line characteristic of a metallic sample (161). This result, together with the observed spectral changes described above, suggest a sharp Mott insulator to metal transition (183). It is clear that intercage cluster interactions are responsible for the IR absorption with increasing sodium atom loading and reflect the supracluster band structure.

b. I-VII Clusters. Silver halide sodalites can be synthesized by silver ion exchange of sodium halo-sodalites using a $AgNO_3/NaNO_3$ melt (184). The silver exchange can be stoichiometrically controlled so that, for example, there is a statistical distribution of one silver atom for every eight cages up to one silver bromide for every cage, $Ag_4Br(AlSiO_4)_3$. Alternatively, one can use the chemistry given in Eq. 2 so that after dehydroxylation the cages contain a specified mixture of Na_4Br and Na_3 units in the cages. Stoichiometric silver atom exchange then gives the corresponding ratio of Ag_4Br and Ag_3 clusters. This makes it possible to control the distance between Ag_4Br units, to adjust the extent of electronic and vibrational coupling between clusters and to monitor the change in going from an isolated Na_4Br to Ag_4Br unit (185). The loading process can be directly monitored by changes in the unit cell dimensions, far-IR, and UV–vis absorption spectra.

Structural refinement of the Na_3AgBr sodalite with adjacent cages filled with Na_4Br shows an interesting effect. The Ag—Br interatomic distance is greatly shortened [2.32(4) Å] from that of the fully loaded Ag_4Br structure [2.671(2)

Å]. Due to more extensive covalent bonding of AgBr compared to NaBr the Na_3AgBr aggregate behaves like a slightly perturbed AgBr molecule with nearby Na^+ ions. In the fully exchanged Ag_4Br sodalites, the Ag—X (X = Cl, Br, or I) distances are about 8% shorter than in the rock salt bulk materials. The intercage Ag—Ag distances are 25–12% longer (Cl^- to I^-) than in the bulk structure. Vibrational coupling between clusters is observed with correlation couplets for both metal and halide atoms with intensities that vary as required during substitution. Intercage coupling can be followed in the UV–vis spectra (Fig. 22) as adjacent cages are statistically filled. The absorption lines go from a very sharp single line for the isolated Ag—Br molecular fragment at low loadings (similar to the gas-phase values of 230 and 320 nm for the AgBr monomer) to the component bands for the Ag_4Br^{3+} isolated cluster to the broader

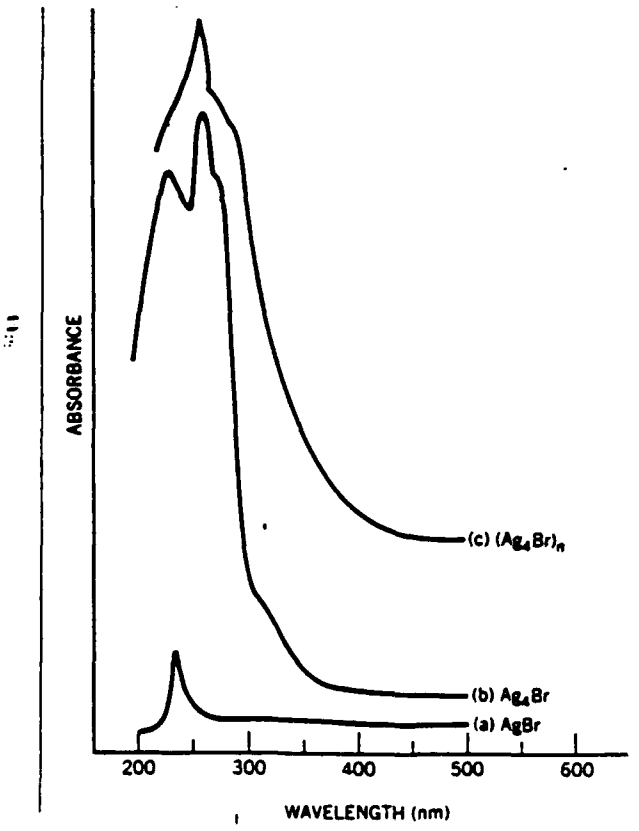

Figure 22. UV–vis spectra showing the progress from the isolated AgBr molecule to the isolated Ag_4Br cluster and to be the extended $(Ag_4Br)_n$ supralattice.

bands for the fully loaded and intercage coupled system that makes up the expanded supralattice. This is an unusual example of being able to observe the change in optical absorption properties for structurally characterized species at specified 3-D lattice separations. The results also show the origins of the Br − (4*p*), Ag^+ (4*d*) mini-valence band and Ag^+ (5*s*) mini-conduction band as AgBr units are added to the structure. Optical absorption data confirms the increased tunneling efficiency and intercage coupling as the distances between centers of the cages decreases in the I^- to Cl^- sequence. Another interesting feature is evidence of a percolation threshold as seen in an abrupt change in the unit cell parameters and FT far-IR cation translatory modes as a function of loading.

The structure of both the frameworks and the clusters within the cages of sodalite structural analogues can be precisely determined. In this connection, it is of interest to note that a comparison of the optical spectrum of Ag_4Br in $Ag_4[Br](AlSiO_4)_3$ and $Ag_4[Br](BePO_4)_3$ (65) reveals a distinct red shift (~70 nm) in the optical spectrum in the latter. This is consistent with the cages being closer together {cage center–cage center 7.328(1) Å $Ag_4[Br](AlSiO_4)_3$ vs. 7.17(1) Å $Ag_4[Br](BePO_4)_3$}; and, as noted above, with the silver atoms in the smaller BePO cages being closer to the center of the 6 rings and therefore to the expanded lattice configuration. These considerations, however, may be secondary to changes in the framework electric field that are obtained by substituting Be for Al and P for Si. This is an example of the composition substitution shown in Table II, giving larger local gradients in the cage electric field.

c. II-VI and III-V Clusters. The net cage charge of an aluminosilicate sodalite cage $(AlSiO_4)_3$ is −3 so that once that charge is satisfied by three monovalent cations, in principle any neutral atom or species might be included within the cage with siting at the vacant 6-ring window and the center of the cage. The primary limitation is the pore size, the 6-ring window in the sodalite cage having a free diameter of about 2.2 Å. This does, however, permit the direct inclusion of many gaseous atoms and it is possible to synthesize aluminosilicate sodalite cages containing Na^{3+} ZnS (186, 187) by vapor-phase deposition. This is an interesting situation where one has a supramolecular lattice containing ZnS atoms and the direct analogue of the Na_3AgBr cluster described in Section IVA.1.b.

Increasing the cage charge to −6 using cage compositions such as $(BeSiO4)_3$, $(BeGeO4)_3$, or $(B_2O_4)_3$ should facilitate incorporating atoms in higher oxidation states. Unfortunately, there is no obvious way to synthesize empty cages such as $Zn_3[\ ](B_2O_4)_3$. Direct synthesis, however, does give the compositions shown in Table V (188). The III-V mixed clusters, Zn_3GaP and Zn_3GaAs are novel new members of the sodalite structure family. The 60-atom cage in these structures has the same acentric point group symmetry 43*m*, the same as that of bulk ZnS or GaP. The tetrahedral Zn_4S fragment is the first coordination sphere of

the sulfur atom in the bulk ZnS structure, so that the result for the extended structure is a supralattice of Zn_4S (Fig. 23) clusters.

Cage control of the first coordination sphere geometry is evident. The cage-to-cage distance is also the cage diameter. The Zn—S distance in $Zn_4S(B_2O_4)_3$ is 0.08 Å less than that in the bulk, but when the cage size is increased from 6.61 to 7.03 Å or larger, the Zn—S increases with cage size to 2.345 Å, which also happens to be the bulk Zn—S distance. The $(B_2O_4)_3$ cage constrains all of the cluster first coordination distances when compared with those of the bulk. The relative bond energies for Ga—O(framework)/Ga—P(As) versus those for Zn—O(framework)/Zn—S(Se) may be responsible for the greater shorter distances in gallium derivatives. In any case, both cluster and intercluster geometry can be varied precisely by the open framework surface of the sodalite structure analogues.

Framework substitution chemistry also changes the intercage distance and the expanded lattice nature of the cage by virtue of the siting of the zinc atoms. For example, with a large anion, Se or Te, at the center of the sodalite cage, the Zn atoms are forced more towards the ultimate limit of being positioned at the center of the 6-ring openings. At that point the system becomes an expanded semiconductor lattice with all Zn atoms equally spaced from all X atoms at the centers of the cages. In the structure of $Zn_4S(B_2O_4)_3$ a 1.05 displacement of the Zn atoms is required to remove the Zn_4S cluster identity.

Although the sodalite cages are relatively small and limit the size of the clusters that can be examined, they provide an opportunity to investigate and precisely model 3-D packaging. One can grow single crystals as large as a centimeter of several of these compositions. The large structure field has lattice parameters varying by as much as 20% and formal cage charges from 0 to −6. The 6-ring pores are sufficiently large so that gas- and ion-phase inclusion

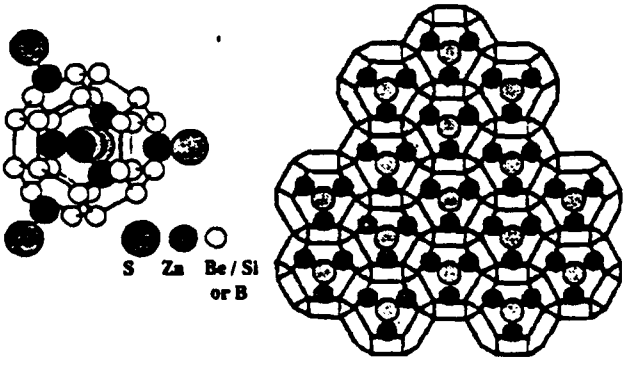

Figure 23. Expanded supralattice of five-atom clusters in sodalite analogue structures.

chemistry can be used to modify the framework and synthesize clusters. As noted above, these are noncentrosymmetric crystal structures with second-order NLO properties. The high optical density has been demonstrated to give exceptional sensitivity and resolution in cathodochromic device applications (167). In the most common space group ($P43n$) for this structural field there is only one susceptibility tensor element, $\chi_{(123)}$, which can be determined directly from powder data and used to evaluate structure–property relationships. Further optical characterization of these materials should provide some interesting insights into intercluster coupling and electrooptic properties of II-VI, III-V, and III-V/VI supracluster nanophases.

2. *Larger Cage Packaging*

a. II-VI and III-V Clusters. The sodalite cages can be interconnected in several ways to give different cage structures, for example, zeolite X has two types of cages available for cluster formation, the smaller 7-Å sodalite units and the larger 13-Å alpha cages (Fig. 3). There are five sites (I, I′, II, II′, III), which are available for cation siting within the sodalite and supercages. The II-VI and I-VII quantum confined clusters can be synthesized by ion-exchange methods, followed in the II-VI case by treatment with H_2S or H_2Se. It is important to note that the ion-exchange process can yield very different siting of cations depending on temperature, pH, solvent versus melt ion inclusion, other extra-framework ions, calcination, and loading levels. This process must be systematically controlled along with the conditions for treatment with H_2S or H_2Se in order to obtain materials that can be consistently reproduced and that contain monosize clusters (4, 124, 189–192).

At a low loading level of CdS in zeolite Y isolated CdS molecular units are formed with an absorption peak around 290 nm and no emission even at 4.2 K. At higher loadings, X-ray powder diffraction, EXAFS, and optical absorption data show that 8-atom $(CdS)_4$ clusters can be uniquely located within the sodalite cages (66–70). The discrete $(CdS)_4$ cubes within the small sodalite units of the CdS zeolite Y structure begin to interconnect as the loading density within the zeolite rises. The Cd atoms point toward each other through the double 6 rings linking the sodalite units with a Cd—Cd distance of 6.2 Å. As this 3-D interconnection proceeds, the corresponding changes in optical properties indicate a progression toward a semiconductor supercluster with behavior intermediate between that of the discrete CdS cubes and bulk semiconductor. If the clusters are loaded into the sodalite cages of zeolite A (Fig. 3), clusters are oriented with their faces parallel across double 4 rings at a separation of about 7.3 Å. The absorption edge is corresponding blue shifted. The transition from clusters to aggregates upon increasing CdS loading is not continuous but rather abrupt, as judged from optical absorption and emission spectra. This suggests

that the aggregation of the individual clusters inside the zeolite may be a percolative process.

When fully loaded, the quantum superlattice shows an exciton shoulder near 340 nm and emits at low temperature. Neither heating nor increasing CdS concentrations can further shift this exciton shoulder to the red. In contrast to this, when CdS is on the exterior surface of the zeolite crystallite a continuous red shift of the absorption threshold towards the bulk value is observed, paralleling the behavior of CdS colloids.

Another method used to control the individual cluster topology is through diffusion of organometallic precursors that are sterically restricted to large channels or cages, and then coreacting these thermally or photochemically (149) to accomplish cluster synthesis. For example, in zeolite Y the organometallic precursor molecules are too large to enter the small sodalite cages and cluster formation can selectively take place in the supercages. Either of these methods requires that one carefully consider the role of the host cage or channel walls and how they will ultimately define the quantum confined structure.

The importance of this in zeolite cluster information is evident in studies of adsorption isotherms of dimethyl zinc and dimethyl mercury in zeolite Y with Si/Al ratios of 3.2 (NaY) and 700 (dealuminated Y) going from vacuum (10^{-5} *torr) at −45°C to the vapor pressure of the organometallic at 20°C* (193). The greater reactivity of dimethyl zinc with the molecular sieve framework is shown in the nearly complete irreversibility of its adsorption into NaY. Dimethyl mercury in NaY shows a two step adsorption curve indicating that above about six molecules per supercage, which may correspond to a monolayer of surface coverage, there is fully reversible adsorption. In dealuminated Y, which has essentially zero framework charge, both dimethyl zinc and dimethyl mercury adsorb reversibly. Opportunities clearly exist to use the electric field, charge carrier or insulator, and chemical bonding properties of the molecular sieve internal surface to control both the self-assembly chemistry and the ultimate quantum confinement geometry.

Attempts to use ion exchange as a route to the formation of III-V semiconductors in zeolite frameworks resulted in the loss of crystallinity of the material due to the very low pH required to keep Group III cations in solution as hydrated cations. Alternate methods of anhydrous nitrate and halide melts also failed to give the desired inclusion products, as did methylene chloride solutions of Group III halides as precursors. MOCVD was successfully used in synthesizing GaP inside the pore structure of zeolite Y (191, 192, 194). The course of the reaction of trimethyl gallium and phosphine has been carefully monitored by ^{31}P MASNMR (magic angle spinning nuclear magnetic resonance) and optical spectroscopy as a function of reaction temperature and loading for both NaY and the acid zeolite HY. For example near the optimum reaction temperature in NaY a 25°C change in PH_3 reaction temperature dramatically changes

both the optical properties and the structural character of the end material. In HY, trimethyl gallium molecules are first anchored at room temperature by the elimination of methane to give $[(CH_3)_2Ga]-OZ$, where OZ refers to the zeolite framework oxygen atoms.

The compound GaP has both a direct and indirect band gap with E_g = 466 nm direct, 546 indirect. The absorption spectrum shows pronounced peaks at 350 nm or less, which are blue shifted relative to bulk GaP. The samples, however, also absorb to the red of bulk GaP, which may be due to the transformation of an indirect to a direct band gap in the quantum confined material. These observations and upfield shifts in the solid state NMR are both indicative of size quantization effects. The supercage point group symmetry of the large cage of zeolite Y is $43m$, the same as bulk GaP, which is expected to help in obtaining periodic and local ordering. Extended X-ray absorption fine structure (EXAFS) spectroscopy and synchrotron X-ray diffraction studies identified 26–28 atom $(GaP)_{13-14}$ clusters in the supercages, which were about 11 Å in diameter, corresponding to three coordination spheres around a central Ga or P atom in the bulk structure.

b. II-VII Included Clusters. One intent of this section was to give examples of the different approaches that can be used in the self-assembly of arrays of atoms in 3-D inclusion chemistry. Solution and liquid melt ion exchange, atomic gas-phase inclusion, direct synthesis, ion exchange followed by gas-phase inclusion reaction chemistry, and organometallic inclusion synthesis have been considered. In this and the following sections we consider two additional approaches, molecular gas-phase inclusion and oxidative photochemistry.

There is a long history of salt inclusion chemistry in zeolites (38, 195). The mechanism for the inclusion is an interesting story and the reader is referred to one of the excellent reviews by Barrer (39) on this subject. An example is the inclusion of NH_4Cl, which almost completely dissociates into NH_3 and HCl. The isotherm that is observed upon absorption shows a steep rise after a minimal concentration is reached. This is indicative of a strong interaction within the zeolite between molecules of NH_3 and HCl, but only after critical concentrations of simultaneously sorbed NH_3 and HCl have been reached. This has been quantitatively treated using a Langmuir site model (196, 197). Molybdenum pentachloride has been loaded into an acid zeolite, H mordenite, then decomposed to the Mo mordenite without any loss of crystallinity or adsorption capacity (198). There is no reason that this approach cannot be extended to volatile semiconductor precursor cluster sources.

As background, a layered perovskite compound, $(C_nH_{2n+1}NH_3)PbI_4$ with n = 4, 6, 8, 9, 10, and 12 or a mixed alkylammonium analogue $(RNH_3)_2(MeNH_3)_{n-1}Pb_nX_{3n+1}$ (R = nonyl, decyl, X = I, n = 1, 2; R =

nonyl, decyl, X = Br, n = 1, 2, 3; R = phenethyl, X = I, n = 1, 2) can readily be formed by mixing PbI_2 with the alkylammonium salts (199, 200). These are unusual 1-D quantum confined photonic materials in that they have sharp excitonic optical transitions, with large oscillator strengths, and large third-order optical nonlinearities; photobleaching efficiencies of these excitonic transitions in thin films of the decylammonium–lead–iodide compounds are about 10^{-7} cm^2 W^{-1} at 510 nm (200). In spite of different spacings, the optical spectra are almost the same for these compounds, which means that the interaction between the layers is weak due to the small dielectric constant of the alkylammonium "barrier layer," which strengthens the Çoulombic interaction between an electron and a hole within the PbI_4^{2-} semiconductor layer.

Extension to two (wires) and 3-D (dots) confinement of PbI_2 by gas-phase inclusion in a number of zeolite cages including zeolites A, Y, L, and mordernite demonstrates again the manner in which cage and channel packaging can be used to control optical properties (201–205). As in the cadmium sulfide studies in zeolite Y, a red shift in the absorption edge is observed with increased loading with the ultimate band edge associated with the cluster loaded molecular sieve stopping short of that of bulk lead iodide (2.57 eV). The changes in optical absorption with loading are dramatic, going in zeolite A from a single band at 5.4 eV (B_1) to the successive growth of absorption peaks at 4.7 eV (B_2), 4.2 eV (B_4·), 3.5 eV (B_4), and 3.2 eV (B_5). These are assigned to the formation of clusters containing 2, 4, and 5 PbI_2 molecular units, respectively. The relatively intensity of B_4· to B_4 does not change and is assigned as a higher excitonic state of the four molecule clusters. If a given zeolite cage is cofilled with another cation, the band edge red shifts as more available space is given to the PbI_2 clusters as evident in the peak energies for K (3.20 eV), Na (3.15 eV), and Mg (3.07 eV) exchanged zeolite Y. The lower energy absorption tails are extended in the case of the channel zeolites, mordenite, and zeolite L, perhaps the result of 2-D confinement of the wirelike structure.

Structurally, the ordering of the clusters in zeolite A can be observed by the presence of a superlattice in the diffraction pattern. The periodicity and presence of PbI_2 moities can be directly observed by high-resolution electron microscopy imaging.

c. Tungsten, Molybdenum, and Chromium Oxide Clusters. It is essential in molecular sieve inclusion chemistry that thermodynamic equilibrium is established for the distribution of the guest within the cages or channels without diffusion limitation due to the pores at some part of the system becoming blocked so that a homogeneous guest distribution is not attained. In the case of MOCVD type of approach, where gaseous byproducts migh react with the cluster atoms, this can be a serious limitation. By uniform loading of a gaseous precursor and then using a photon source to dissociate one or more of the precursors, depo-

sition and epitactic growth of quantum confinement within a zeolite can be accomplished at lower temperatures and more cleanly (142, 148, 206, 207). Bulk tungsten oxide has a band gap of 2.7 eV, slightly higher than that of PbI_2. The redox and solid state chemistry of this semiconductor has an incredible diversity leading, for example, to the semiconductor and semimetallic tungsten bronze phases (208).

The simple binary carbonyls of Group 6 (VIB) metals are volatile, have small dimensions relative to the large zeolite pore structures, are easily purified, and can be quantitatively photoconverted to the respective metal oxide materials and gaseous CO_2 with minimal carbon contamination. The intrazeolite photooxidation chemistry of alpha-cage encapsulated hexacarbonyltungsten(0) in $Na_{56}Y$ and $H_{56}Y$, $n\{W(CO)_6\}-Na_{56}Y(H_{56}Y)$, with O_2 provides a novel synthetic pathway to a zeolite alpha-cage located W(VI) oxide, $n(WO_3)-Na_{56}Y(H_{56}Y)$, ($n$ = 0–32). This formulation represents the unit cell contents, which has eight supercages, so that at full loading there are 4 WO_3 units per supercage.

At loadings of less than one WO_3 per supercage the absorption edge is blue shifted from the bulk WO_3 band gap edge to 3.5 eV. When the concentration is more than one WO_3 per supercage, there is an abrupt shift of the absorption edge to a limiting value of 3.3 eV, which is maintained to the highest loading composition of roughly four WO_3 per supercage. The FTIR, MASNMR, XPS (X-ray photoelectron spectroscopy), and EXAFS data suggest first the formation of $(WO_3)_2$ dimers, then $(WO_3)_4$ tetramers as the loading is increased.

The siting and carbonyl displacement chemistry have been extensively studied. Intrazeolite reactions of the tungsten tricarbonyl intermediate with large and small arenes, trienes, and phosphines cleanly yields the respective intrazeolite six-coordinate complexes, and are used to locate the tricarbonyltungsten(0) fragment on the internal surface of the zeolite. The known electrochromic, solid state ion insertion, and electronic–ionic transport of bulk WO_3 make this a particularly interesting cluster system to study.

3. *Large Channel Host Confinement*

There is presently a dearth of crystalline porous materials with cage and channel dimensions between 14 and 100 Å, however, as indicated previously in this chapter, this situation is rapidly changing. The tubular channels of chrysotile asbestos are 15–70 Å in diameter. In nature these are available as single crystals with dimensions of 0.1–0.2 mm in diameter and 10–15 mm in length. The channel sizes can be determined by measuring the conductivity through a single crystal during pressure loading of the channels by a nonwettable liquid, mercury or gallium (209). The scatter in the diameters of the metallic filaments obtained in this fashion is less than 4% (210). Metals loaded into these channels

are characterized by a decrease in melting point of the metal and a limitation of the mean free path of electrons by the walls of the channels. The transition to the superconducting state of mercury becomes diffuse with decreasing diameter of the filaments, with the diffuseness reaching 100% of T_C for filaments that are 5-atomic diameters in width (209). The critical magnetic fields increase with decreasing diameter of the filaments, and reach a value that is three times larger than the paramagnetic field limit for mercury. There is no substantial increase or decrease in T_C with pore size changes, and it appears that as the pore size is decreased the superconducting transition simply becomes ever less noticeable with respect to the rising background of other phenomena.

B. Oriented Organic Nonlinear Optic Guests

1. Background

The existence of polar molecular sieve structures provides access to an additional degree of control of cluster orientation. A noncentrosymmetric host could cause nanoclusters to dipole align rather than have a random or net centrosymmetric orientation. Using the above ideas to vary host framework charge density or dielectric constant, via Si/Al ratio changes or by changing the framework composition, it is possible to define the relative amounts of guest–host and guest–guest electrostatic interactions. For example, guest dipole molecules interact more strongly with one another in a low charge density host than in a high charge density host where guest–host interactions dominate. In a low charge density hosts, guest aggregation or chain formation should occur and lead to bulk dipole alignment. The counterions present in the host can also be used to control guest aggregation. Changing the size of the ions alters the pore size, shape, and also the local electrostatic fields around the ions. The following discussion describes recent work from the author's laboratory on the self-organization of organic guests in 3-D periodic hosts (156, 211–215).

Nonlinear optical properties are determined by the bulk hyperpolarizability tensor, $\chi_{(n)}$, a quantity which, in the second-order case, 2, is very sensitive to symmetry restrictions (9, 216–220). For a material to exhibit second harmonic generation (SHG) it must have a noncentrosymmetric crystal structure. This single restriction dominates any search for new materials for SHG applications. In molecular chemistry the effort is to align molecules so that a net bulk dipole results. This has been accomplished in crystals by using a variety of strategies (221) including molecular asymmetry, chirality, hydrogen bonding, dipole reduction, and changing the counterions in salts (222). Dipole alignment in poled polymer and Langmuir–Blodgett films is receiving considerable attention because of device applications (9).

2. *Host Considerations*

Inclusion chemistry is particularly well suited to accomplish optimization of molecular alignment by careful size and shape matching of host and guest. The first reports of inclusion chemistry as a method of generating nonlinear optical materials, were by Tomaru et al. (223, 224). They showed the *p*-nitroaniline and closely related organic guests exhibited SHG four times urea in the presence of β-cyclodextrin. Wang and Eaton (225) showed shortly thereafter that this was indeed due to inclusion and expanded the field (226, 227) to other hosts [thi- , tris(o-thymotide), and deoxycholic acid] and organometallic guests, mainly of the aryl metal tricarbonyl type.

Inorganic hosts have the advantages of thermal and photo stability over organic hosts. The thermal stability of organic systems is inherently low because of their molecular nature, whereas inorganic hosts can be made stable to over 500°C. Some of this thermal stability will be conferred upon the guest through limitations on motional degrees of freedom within the restricted pore space. More rigid inorganic hosts allow complete flexibility in guest concentration between empty and filled pores. Variation of guest concentration provides a simple method to control guest aggregation and bulk nonlinear optic properties.

Host symmetry is critical for the production of SHG. Guest molecules in a centrosymmetric host can cause a structural rearrangement in the host to give a noncentrosymmetric inclusion material (228), which could produce SHG. A noncentrosymmetric host, on the other hand, could cause guest molecules that normally crystallize in a centrosymmetric fashion to assume the lower symmetry of the host. Noncentrosymmetric molecular sieves with large enough pore openings to incorporate organic molecules include ALPO-5 (*P6cc*) (229), ALPO-11 (*Ic2m*) (230), VPI-5 ($P6_3$) (54, 231), and Offretite ($P\bar{6}m2$) (232), all 1-D channel structures.

A particularly intriguing feature of the aluminum phosphate channel structures are the helical structure directing elements in AlPO-5 and VPI-5. The oxygen atoms of the ALPO-5 channel form a 24-fold helix along the channel (Fig. 24) (43). In the larger channels of VPI-5, adsorbed water forms a triple helix (Fig. 25) (231). The helical arrangement that is characteristic of a translational enantiomorphic form can be expected to play an important role in the self-aggregation of organic molecules within the channel.

The molecular sieves ALPO-5, ALPO-11, and VPI-5 are aluminophosphates with neutral, relatively hydrophobic frameworks. The molecular sieve ALPO-11 has elliptical 6.7 × 4.4 Å 10-ring channels while ALPO-5 and VPI-5 have circular 12-ring and 18-ring channels that are 8 and 12–13 nÅ in diameter, respectively. Framework substitution of aluminum or phosphorus for silicon (to make SAPOs) or other metals can be used to vary the framework charge density

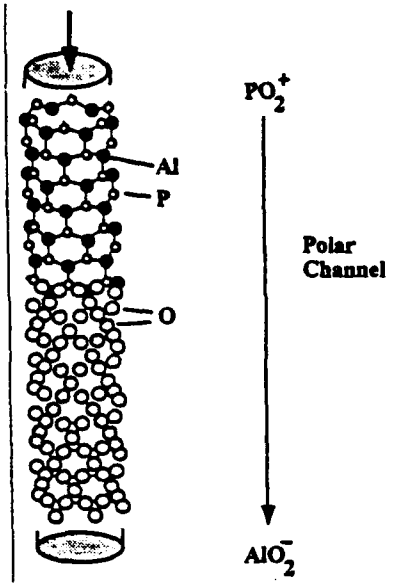

Figure 24. The 24-oxygen atom helical structure that defines the pores of ALPO-5 (43).

in these hosts (76). Offretite, with a formula of $(K_2Ca)_{2.5}[(AlO_2)5(SiO_2)_{13}]$ has a relatively highly charged framework with 6.9-Å diameter 12-ring channels.

In the experiments described by Cox et al. (214) both centrosymmetric and noncentrosymmetric hosts were tried. Significant polar alignment was observed only with noncentrosymmetric hosts. The sensitivity of the SHG measurements was on the order of $10^3 \times$ the signal from a comparable mole sample of quartz and it is possible that exterior surface alignment on some centrosymmetric phases might have contributed a signal below this limit.

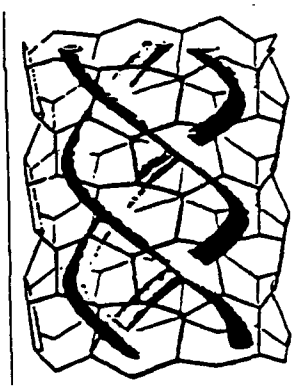

Figure 25. Triple helix of water atoms in channels of VPI-5 (231). (Reprinted by permission from *Zeolites*, vol. 11, p. 310, copyright © 1991 Butterworth-Heinemann, Ltd.)

If molecular dipoles are weakly coupled, as is usually assumed to be the case for hyperpolarizable organic molecules and even for inorganic extended solids, it is possible to arrive at some symmetry conclusions regarding the optimum point groups for obtaining a large nonlinear response from a rigid molecule such as benzene with anisotropic polarizability (233). The question that is addressed is how the molecular second-order polarizability coefficients reenforce or cancel each other. If the space group of the host is the symmetry generator for the composite, the favored hosts and their respective hosts are in order of preference: ALPO-11 (*mm*2), offretite (6*m*2), VPI-5 (6), and ALPO-5 (6*mm*).

3. *Guest Considerations*

Inclusion guests for SHG, which have large nonlinear optic coefficients, are molecules with conjugated electron systems with attached donor and acceptor groups that lead to charge-transfer excited states (234). This enhances second-order nonlinear optical properties because of the large change in dipole moment between ground and excited states (235). Size and shape can be varied by alkylation on nitrogen or on the aromatic ring leaving the electronic system unaffected. Cutoff wavelengths can be shifted into the UV by using pyridine or pyrimidine for the aromatic substrate or toward the red with stilbene or related extended conjugated systems. A variety of organic and organometallic guests were investigated by Cox et al. (214) with some examples shown in Fig. 26. Note that 2-methyl-4-nitroaniline (MNA) has an electrooptic coefficient that is

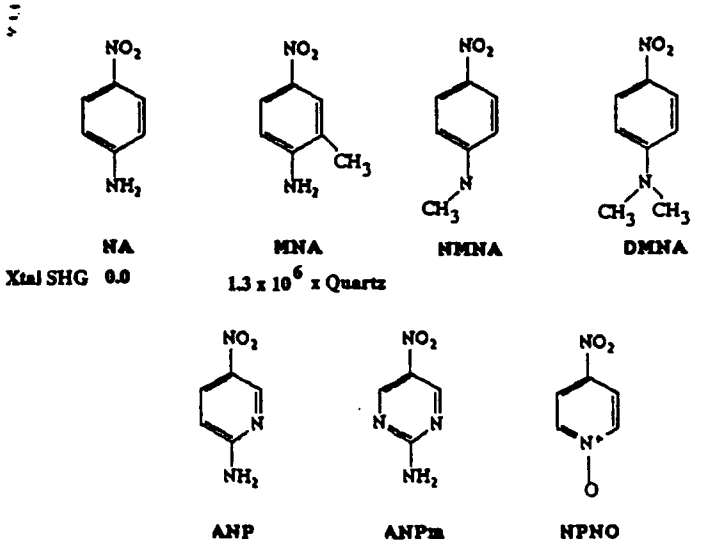

Figure 26. Molecular acronyms for hyperpolarizable organic molecules.

about 270 pm V^{-1}, a powder SHG signal about 22 × urea that is about 600 × quartz (231) and a single-crystal SHG intensity 1.3 × 10^6 × quartz (236). In spite of its excellent SHG response, it is very difficult to grow as a single crystal. In contrast, *p*-nitroaniline (NA) has a SHG signal = 0 in the bulk since it crystallizes in a centrosymmetric space group. Only a few neutral organics with favorable molecular nonlinear optical properties have the required noncentrosymmetric structure to show an SHG signal. This is because large dipole molecules such as these have a strong tendency to pair up with dipoles pointed in opposite directions.

4. *Organic Nucleation in Channels*

The thermodynamic contributions to the self-assembly of organic clusters in molecular sieves are those described in Section III.B.2. The process must be considered from the starting point of absorption on the exterior surface of the crystal, with polar alignment. The imaging of zeolite pores (237) and the self-assembly of polar molecules on the exterior surface of zeolites with siting of the polar molecules at the pore openings has been experimentally observed recently by atomic force microscopy (156). The exterior surface orientation of the organic dipoles is important, since molecular modeling has shown that 180° rotation of the molecular dipole axis to give inversion of the dipole with respect to the crystallographic polar axis is not feasible once the dipole is inside the channels of AlPO-11 and highly improbable for AlPO-5 (Fig. 8). It should also be noted that the organic molecules in a given channel are separated from those in other channels by several monoatomic layers of framework atoms so that interchannel dipole–dipole interactions are small. This, in fact, is fortunate since it diminishes the probability of the organic dipoles from aligning with opposing dipolar orientations.

Once inside the channels the self-assembly of the molecules will be determined by competitive intermolecular interactions and the interactions with the walls. For NA and MNA, the strongest intermolecular interactions will be due to hydrogen bonding (238). In a single crystal of *p*-nitroaniline the molecules align in helical chains as shown in Fig. 27 with an equal number of chains pointing in opposite directions. Important molecule–host framework interactions include (a) hydrogen bonding between the NA or MNA molecules to the host framework oxygen atoms, (b) hydrogen bonding to dangling framework OH groups in the case of VPI-5 (231), or (c) coordination of the amino nitrogen atom or the nitro oxygen atoms to an extra-framework cation for the SAPO, offretite or any other charged framework molecular sieves. The thermal stability of the organics are enhanced after inclusion. Heating NA in ALPO-5 to 100°C under dynamic vacuum does not result in any weight loss except when excess organic, not included within the molecular sieve pores, is present so that this

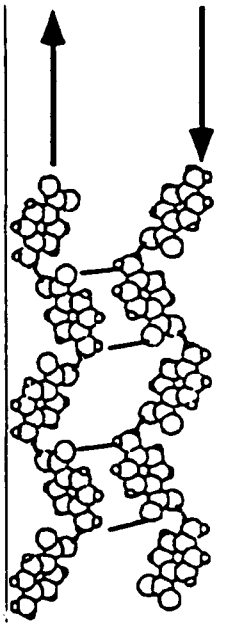

Figure 27. Cancellation of NA helical chain dipole moments for bulk NA nitroaniline. [Reprinted with permission from M. C. Etter, K. S. Huang, G. M. Frankenbach, D. A. Adsmond, in Materials for Nonlinear Optics: Chemical Perspectives, S. Marder, J. E. Sohn, and G. D. Stucky, (Eds.), American Society Symposium Series, 1991, vol. 455, pp. 446–456. Copyright © (1991) American Chemical Society.]

is a good way to clean up excess bulk organic. Exposure to ambient air does not cause displacement of the guest from the ALPO-5 pores but SHG intensities show some diminution in air.

The flexibility of the molecular sieve framework can be used to good advantage in monitoring the loading of the molecular sieves (Figs. 28 and 29). As

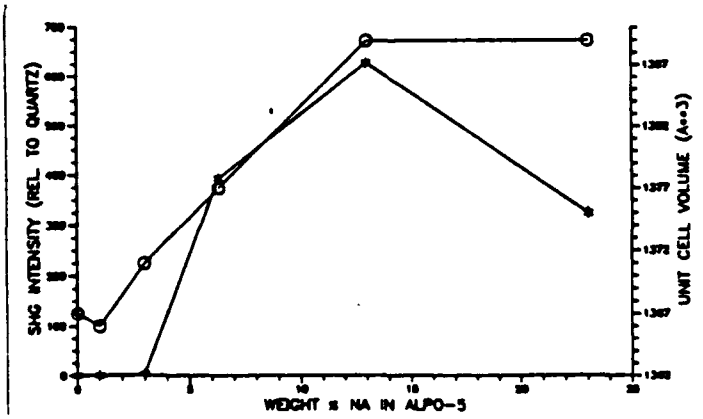

Figure 28. Variation of second harmonic intensity and unit cell with loading of NA into ALPO-5 (214).

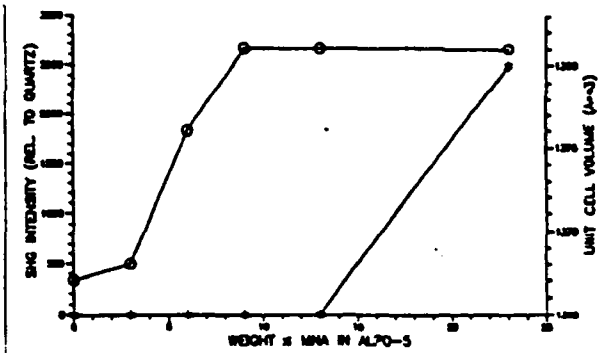

Figure 29. Variation of second harmonic intensity and unit cell with loading of MNA into ALPO-5 (214).

the guest is loaded into the channels of AlPO-5, the unit cell volume increases regularly with loading, demonstrating definitively that the organic molecule is located inside the molecular sieve pores. For loadings beyond that for which the unit cell volume reaches a maximum, it is possible to detect external crystalline organic molecules by X-ray diffraction.

p-Nitroaniline shows a SHG threshold at around 3%. Second harmonic generation then rises sharply to a maximum of more than 650 × quartz at 13% loading. The decrease in SHG after maximum loading is due to scattering and absorption of the second harmonic light generated by the molecules inside of the crystal by bulk crystals on the exterior of the crystal that have no SHG capabilities. Thus the SHG of NA is turned on by self-assembly in ALPO-5. 2-Methyl-4-nitroaniline in ALPO-5 has no SHG until crystals of MNA are present on the exterior surface at the highest loading. The SHG at 13% MNA is less than quartz, about the same as the ALPO-5 host alone. The SHG of MNA is thus turned off by inclusion. Only after the exterior crystals are present is there a second harmonic signal, as expected for bulk MNA. This is a dramatic example of how changes in guest size and shape can be used to design nonlinear optic properties using nanoscale inclusion chemistry.

The overall increase in SHG with NA loading is due, in part, to the increasing number density of NA molecules present. But the more than 10-fold increase in SHG from 3 to 6% loading cannot be attributed to this alone. Furthermore, if NA molecules were being aligned at the 1% loading level for instance, a substantial SHG signal would be observed because the molecular hyperpolarizability of NA is so large. Diluting MNA to the 1% level in an inert matrix such as sodium chloride shows this to be the case.

The SHG threshold phenomenon observed in NA in ALPO-5 is analogous to that observed for the absorption of mercury in a silver exchanged zeolite (158) and the adsorption of NH_4Cl into H-mordenite (197), and implies a strong

intermolecular interaction. At low loadings the guest–host wall interactions dominate and determine the orientation of the molecules. At a particular loading threshold, about 3%, the packing density is such that the intermolecular interactions start to dominate and the molecules in effect reach a critical nucleation size so that their further orientation and growth is determined by the intermolecular hydrogen bonding. The nonlinear effect then turns on. The FTIR measurements verified the above and the absence of significant intermolecular hydrogen bonding for MNA as a function of loading. The conclusion is that the switching off of MNA is due to an inability to form hydrogen-bonds because the added methyl group on MNA restricts its orientation in the ALPO-5 channels.

An interesting opportunity exists for orthogonal self-assembly with 2-D confinement. Taking two molecules, NA and MNA, with diametrically opposed bulk and nanoscale self-assembly behavior, would adding a small amount of MNA to a NA sample disrupt the alignment, or conversely would NA in a MNA sample cause alignment of all the molecules to occur? This was investigated by varying the wt% NA at a total NA + MNA loading of 12% (nearly full) and concurrent, random loading at 6% total NA + MNA. At 12% total loading, concurrent addition of NA and MNA results in the same pattern as adding only NA. No significant alignment of MNA by NA or disordering of NA by MNA seems to be occurring, that is, NA and MNA appear to act independently with NA molecules forming aligned aggregates as if no MNA were present.

At 6% total loading, alignment of MNA by NA is occurring. At a NA level of only 3%, the SHG corresponds to a 5–6% NA loading, so MNA is contributing to the SHG. The difference between 6 and 12% loadings could be due to the extra space available in the host pores at the 6% loading level, which could allow greater conformational freedom for NA and MNA molecules to successfully interact and become aligned. Also, the SHG versus wt% NA curve has a steep slope at the 6% level but is flat at 12% so small changes in the number of aligned molecules would make a big difference at 6% but not at 12%. In any event, the ability to use orthogonal bimolecular self-assembly is demonstrated.

If a chain of NA molecules (Fig. 27) is forced into an ALPO-5 channel, many interatomic distances are less than van der Waals. This chain would fit easily if stretched or straightened out moderately. A simple geometric calculation of the amount of space available within the ALPO-5 pores shows that at 13% NA loading there is 5.3 Å of channel length available for each NA molecule. Molecular modeling confirmed the single chain arrangement in AlPO-5 as shown in the pictorial representation in Fig. 30. The predicted angle that these molecules make with the channel axis is less than 60°, very close to the optimal angle 54.74° for the ALPO-5 point group, 6*mm* (233, 239). The NA chain in the ALPO-5 channel is a stretched-out version of the chain in the pure organic bent O——H—N angles, which would reduce hydrogen bonding com-

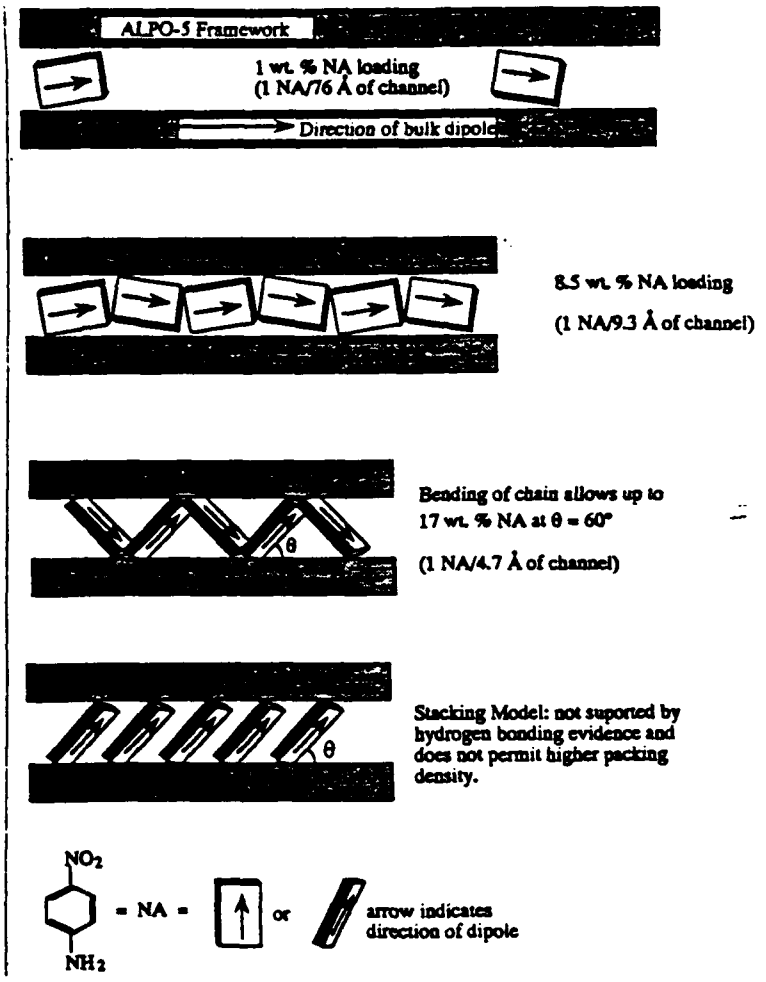

Figure 30. Schematic models for self-assembly of NA molecules into the ALPO-5 channels (214).

pared to the pure organic as observed by FTIR. The critical role of hydrogen bonding for ALPO-5 was also verified by sequential methylation of the amino group, NA (SHG = 1000 quartz), NMNA (SHG = 50 quartz) and DMNA (SHG = 0.9 quartz); however, this is not universally true for all hosts.

If there were only one host, AlPO-5, which was capable of alignment, this exercise would be of limited interest. Fortunately, however, this is not the case (Table VI). By using offretite and SAPO-5, host charge effects can be studied. ALPO-11 has a smaller elliptical channel, but crystallizes in the space group,

TABLE VI

Guest	Host[a]			
	ALPO-5[b]	SAPO-5[c]	ALPO-11[d]	VPI-5[e]
NA	1000(200)	280(70)	500(130)	50(10)
MNA	0.2(0.05)	0.7(0.2)	120(30)	90(20)
NMNA	50(10)	8(3)	37(10)	40(9)
DMNA	0.9(0.3)	0.4(0.1)	110(50)	15(3)
ANP	970(250)	500(50)	140(40)	150(30)
ANPm	3(1)	1.1(0.3)	55(10)	70(20)
NPNO	0.5(0.1)	0.5(0.1)	6(1)	33(5)

[a] SHG data relative to quartz, uncertainties shown in parentheses.
[b] 10–13 wt.% guest loading level.
[c] 12 wt.% guest loading level.
[d] 9–10 wt.% guest loading level.
[e] 20 wt.% guest loading level.

Ic2m, which is a more favorable space group for symmetry directing an NLO response (238, 239). VPI-5 offers the possibility of making at least a double-stranded helix of NA molecules (Fig. 8).

The SHG data in Table VI are representative of the fully loaded samples. The loading dependence of the SHG signal is shown in Fig. 31. In marked contrast to ALPO-5 and SAPO-5, ALPO-11 and VPI-5 align to some extent all of the organics tried. The structural similarity between ALPO-5 and SAPO-5 result in the same pattern of SHG results for the various organics, that is, MNA is turned off, *N*-methylation shuts down the SHG in steps, NA and ANP are turned on, and ANPm and NPNO are not. The results for DMNA and NPNO in ALPO-11 and VPI-5 show that hydrogen bonding is not a necessary condition for alignment. Electrostatic interactions between host and guest and space restrictions within the channels must be enough to counteract the tendency of the molecular dipoles to pair up in opposite directions. The helical symmetry directing properties of VPI-5 and the *mm*2 point group symmetry of ALPO-11 must then control the self-aggregation.

It is much more informative to compare SHG data as a function of loading (Fig. 31). Data for each load point are taken with the same host, so the only variable is the amount of guest. ALPO-5 and ALPO-11 have a similar pattern of increasing SHG with loading with an SHG threshold at about 3% for laser frequencies at both 1.064 and 1.907 μm showed the same pattern. ALPO-11, with its smaller pore diameter, may therefore cause NA to form similar but more stretched-out chains when compared to ALPO-5 (Fig. 31).

VPI-5 shows a distinct maximum in SHG at about 9% NA above which the SHG falls off. The much larger pores of VPI-5 must allow NA molecules to form molecular pairs with dipoles pointing in opposite directions. The maxi-

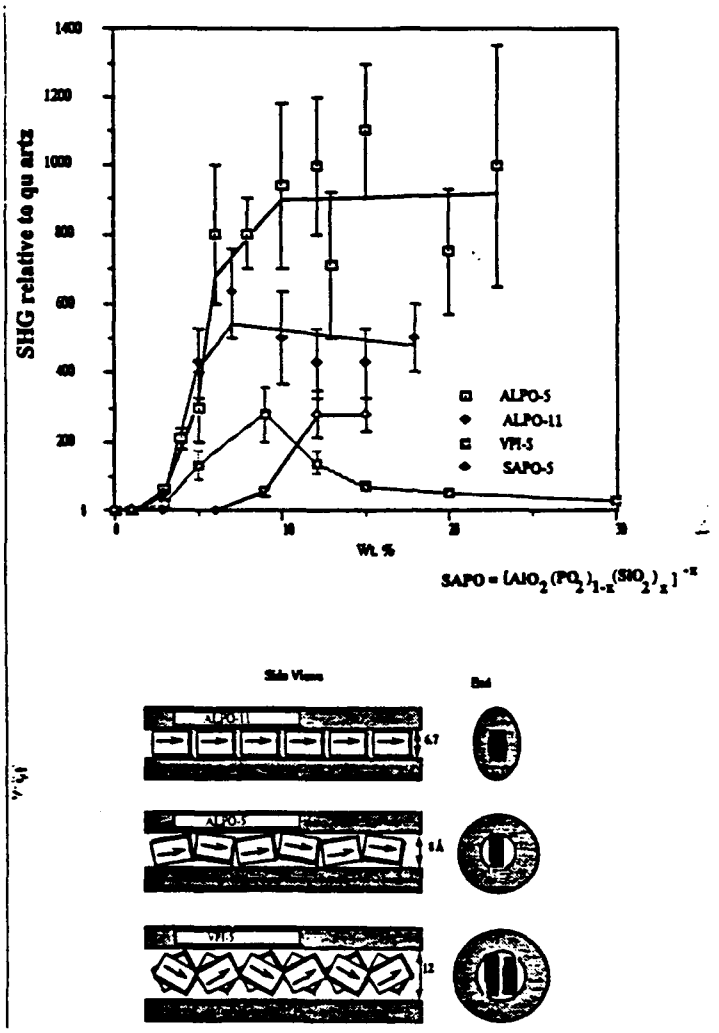

Figure 31. *Top*: Relative SHG intensity versus wt% NA in ALPO-5, ALPO-11, VPI-5, and SAPO-5 (214). *Bottom*: Models that show how NA molecules can fit into the channels of ALPO-11, ALPO-5, and VPI-5.

mum at intermediate loading fits well with a model where chains or aggregates of NA molecules similar to those present in ALPO-5 are forming without pair formation at intermediate loadings. As in the bulk, additional molecules form chains running in the opposite direction causing the decrease in SHG as shown in the schematic representation in Fig. 31.

SAPO-5 loading data presents the first evidence that host framework charge or dielectric constant is an important parameter in these studies. Figure 31 shows that the SHG threshold in SAPO-5 occurs at a much higher loading level than in ALPO-5. *p*-Nitroaniline molecules must be more strongly attracted to the SAPO-5 framework than in ALPO-5, so the intermolecular interactions are disrupted until a high enough loading is reached. One would predict that higher silicon contents in the SAPO-5 would eventually shut off all SHG. The cutting off of alignment by large framework charge and the presence of extra-framework atoms is confirmed for offretite, which although noncentrosymmetric, was not a good host for organic dipole orientation. For NA at least, strong guest–host interactions are detrimental to SHG. This finding represents a new type of conceptual nonlinear optic tuning effect in which changes in host dielectric results in large variations in SHG without changing guest concentration.

These results show how important it is to carry out loading studies in systems such as this. With only one data point, the SAPO-5 and VPI-5 systems seemed similar to ALPO-5. The loading studies clearly demonstrated the effects of framework charge and spatial restraints on molecular aggregation and alignment in molecular sieves.

Numerous other points of interest came from this study. The color of many of the inclusion materials is significantly different than the pure organics. *p*-Nitroanilines and its derivatives are solvatochromic, the lowest energy absorption band of NA moves from 320 nm in methylcyclohexane to 380 nm in DMF (240). Diffuse reflectance UV–vis shows solventlike effects on the cutoff wavelength and absorption maximum in these samples compared to the pure organic. The NA absorption edge or cutoff wavelength is shifted by 30 nm in ALPO-5 and SAPO-5 but not shifted at all by VPI-5 and by only 10 nm by ALPO-11. 2-Methyl-4-nitroaniline shows almost no shifts due to inclusion but the *N*-methyl derivatives have large shifts of up to 60 nm. In ANP, ANPm, and NPNO the shifts are smaller but in the opposite direction. SAPO-5 and VPI-5 both depress the intensity of the lowest energy part of the band in all cases. The mixing of ground and excited states is a major source of enhancement of SHG so, in general, a lower energy electronic transition could contribute to increased SHG. All of the NA samples show large SHG intensities, and the band shift in ALPO-5 and SAPO-5 could be causing some SHG enhancement in these systems.

In summary, three modes of SHG tuning are demonstrated by these materials: variation in loading level, variation in guest structure or composition, and variation in host framework charge or dielectric constant. This allows great flexibility in formulating promising new combinations and opens up many new avenues of organic guest–inorganic host inclusion synthesis of NLO materials. Beyond this, however, the systems are proving to be models for developing a fundamental understanding of nucleation and nanophase synthesis.

C. Nonlinear Optic Framework Active Hosts

1. Background

Besides being a commercially important class of inclusion materials (241–245), the potassium titanyl phosphate (KTP) structural family provides an excellent example of how the guest can be used with selective siting to modify the electronic and structural properties of the NLO active host surface. This is in contrast to the above discussions in which the primary point of interest was the use of the host to control guest self-assembly and aggregation. In Section II.E the structure of KTP is described (Fig. 11). The chemistry of this structural family and its properties have been recently reviewed (11) so that the following presentation is an abbreviated perspective in the context of this chapter on the interface of nanoscale inclusion chemistry. More specifically, we will briefly consider the advantages of using inclusion chemistry in addressing the following points:

The synthesis of combination phases [e.g., $MM'(TiO)(GaF)(PO_4)$] and the creation of NLO materials outside the synthesis phase space [e.g., $Cs_xK_{1-x}TiOPO_4$].

Selective siting and pinning (or depinning) of delocalized excited states by inclusion chemistry.

2. Synthesis Phase Space and Combination Phases

One of the attractive features of inclusion chemistry is the enormous number of ways in which a nanocomposite can be constructed without fundamentally changing the host or guest structure type. Until now we have presented a rather simplified view of a guest and a host. It should be emphasized that many times there is a need for multiple kinds of guests and that it may be useful to consider different parts of the host surface independently from a synthetic and even property point of view. Structurally, this was done in Fig. 11 by describing the $-Ti-O-Ti-O$ helical chain as one unit and the phosphate groups that complete the titanium coordination sphere as another host entity. The guests are defined as usual by the ability to reversibly ion exchange them or in the case of NH_4^+ and H_3O^+ to reversibly remove or add ammonia or water to the host. The reason for differentiating the host structural components is that the long–short bond lengths in the titanyl chain are structure directing. If the titanium is replaced by tin (246–249), the bond lengths are nearly equal and it is experimentally difficult to establish that the space group is indeed noncentrosymmetric and not centrosymmetric. Furthermore, the general consensus has been that the titanyl bond length inequality is directly associated with the large NLO response

of KTP (250, 251) and that the phosphate groups only serve a structural function. From this point of view the structure is a titanyl helical chain with the bridging titanyl oxygen atoms trans for one of the two structurally independent titanium atoms and cis for the other titanium atom. These framework TiO chains are linked together by phosphate bridges (*right*, Fig. 11).

The second useful feature of the $KTiOPO_4$ structure is that as far as the crystal chemistry is concerned the composition is really $(KTiOPO_4)$-$(K'Ti'O'P'O_4')$. The molecular chemist's analogue is a molecule with the same element in two nonequivalent sites. Those atoms can be expected to react differently, have different NMR properties, and so on. Synthetically the composition of these two types of sites can be independently varied. Some compositional changes at these sites that have given isostructures include: (a) substitution of F^- or OH^- for the titanyl oxygen atoms (96), (b) replacement of phosphate by arsenate (252), and (c) substitution of titanium by the other tetravalent ions (11). The cation guest also can be exchanged from sodium through cesium. The result of all this is that it is possible to create combination phases such as $MM'(TiO)(GaF)(PO_4)(AsO4)$ with a high probability that it will be a KTP isostructure (96). If there are h possible host substitutions and g possible guests, the number of possible isostructure NLO materials in the family is

$$HH'GG' = \frac{h!}{2(h-2)!} \cdot \frac{g!}{2(g-2)!} \tag{8}$$

Only a small number of these possibilities have been explored. The approach that has been used, however, is to examine the effect of each type of substitution on the NLO response and on that basis focus the research on those avenues that seem to be the most promising. It is clear at this time that the unsubstituted titanyl chains has by far the largest NLO response. The roles of the other framework atoms and guest cations are still a matter of considerable interest.

For phase matching and effective NLO response (9), it may be desirable to use sodium or cesium atoms, respectively, rather than potassium, that is, NaTP or CsTP. Neither of these two are accessible by the usual hydrothermal or flux routes. In the case of sodium the KTP structural phase space ends at 65 mol% of potassium. The region between 0 and 65 mol% of Na is single phase and consists of a solid solution with the formula $K_{1-x}Na_xTiOPO_4$. The two-phase region between 65 and 100 mol% of Na contains $K_{0.35}Na_{0.65}TiOPO_4$ and α-$NaTiOPO_4$ in varying proportion. The compound β-$NaTiOPO_4$, which has the KTP structure, can be prepared in powder or single-crystal form by treating KTP powder or crystals with a molten $NaNO_3$ flux at 350°C (11). This also works for the synthesis of $Cs_{0.20}K_{0.80}TiOPO_4$. By masking the surface of single crystals this ion exchange chemistry can be used very effectively to create wave

guides (244) by slightly changing the indices of refraction of the bulk material along the light path in the solid.

3. *Selective Siting and Pinning of Delocalized Excited States*

Using a little imagination and some structural data, there is a resemblance between the poly(acetylene) and $KTiOPO_4$ structures (Fig. 32). Both have alternating long–short bonds and both are premier NLO materials. More importantly both have delocalized excited states, which on perturbation with an incident laser beam can be mixed into the ground state so that the electrons are easily polarized to give large NLO coefficients (11, 253). Unlike poly(acetylene), doping the titanyl chain in KTP can be done selectively with site specificity into a 3-D ordered lattice. The electronic origin of the alternating long–short bond lengths in the titanyl structure is therefore of considerable importance in order to understand structure–property relationships.

Recently, Burdett et al., (254, 255) showed that the metal–oxygen bond alternation (vanadyl, titanyl, etc), which are found in perovskites, linear chain compounds such as KTP, and several cyclic systems, may be understood in terms of a second-order Jahn-Teller effect, which couples the largely oxygen nonbonding levels at the top of the oxygen *p* band with the metal–oxygen antibonding levels of the metal *d* band. This distortion results in the mixing of charge-transfer character into both the bonding orbitals and the nonbonding oxygen lone-pair orbitals, which constitute the HOMO (highest occupied molecular orbitals). The anharmonicity in these electronic potentials depends on the degree to which charge-transfer character can be mixed into the ground-state orbitals.

The nature of the charge-transfer excited state has been examined by Phillips et al., (256) and by Blasse and Brixner (257). The compound $KVOPO_4$ is isostructural with $KTiOPO_4$ and in fact the vanadyl bond length is the shortest [1.672(8) Å] octahedral M—O distance reported in the KTP structure field. With increasing V substitution for Ti in KTP the band edge broadens and systematically shifts to the red as the excited state acquires more vanadium char-

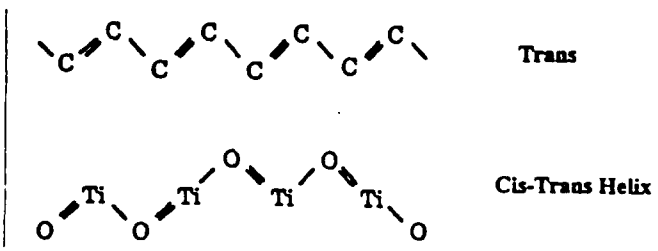

Figure 32. Comparison of structures of poly(acetylene) and titanyl (KTP) chains.

acter. When the composition reaches KVP the absorption is intense and nearly continuous throughout the visible region well beyond the weak 700 nm *d–d* transition and into the IR. Consequently, the excited state MO cannot be localized on the MO_6 octahedra, but must instead be delocalized along the O—M=O chain analogous to organic conjugated systems. Blasse and Brixner (257) reached similar conclusions from the observation of an emission band at 390 nm at temperatures below 100 K. The band has an unusually small Stokes shift of 4200 cm^{-1}, well below the value of about 10,000 cm^{-1} observed for most titanates. The conclusions are that the excited state of KTP is delocalized and that mixing this state with the ground state by the laser electric field is the reason for the unusually large excited state dipole moment contributions and the exceptional NLO behavior of KTP (11, 256).

From this point of view it is necessary to treat the electronic states in terms of delocalized band structure model in order to fully understand and use inclusion chemistry to control KTPs optical properties. Increased band gap energy (E_g), caused by substituting d^{10} metal ions such as Ga, Ge, and Sn onto the octahedral sites of the Ti—O—Ti=O chain, reduces distortion by Burdett's model and decreases virtual state transition probabilities for excited state delocalization. This in turn means a sharp attenuation in NLO susceptibility. Replacing As for the more electronegative P on the tetrahedral sites increases the coordination strength of the exchangeable cation to the XO_4(X = P or As) oxygen atoms and correspondingly decreases the strength of the interaction of the cation to the $(Ti—O)_n$ chain oxygen atoms. This decreased "pinning" of the delocalized excited state (and smaller band gap) would explain the observed 60% improvement in doubling efficiency of KTA over KTP as determined by single-crystal SHG measurements (245).

A related effect is the loss of microscopic susceptibility that takes place as the interactions between the cations and framework oxygen levels become more covalent. This occurs when low-coordinate and/or highly electronegative cations cause the occupied TiO_6 orbitals to become more stable, limiting the degree of excited-state mixing possible. The effects are manifested in Na or Ag exchanged KTP type structures in which the average cation–oxygen coordination distance drops from 2.9 to 2.6 Å, and a generally closer association of the cation with the framework. The differences lie in the relative preferences of the cations for the $(Ti—O)_n$ chain and the PO_4 (or AsO_4) oxygen atoms. In NaTP, as in KTP, the average bond valences for the Na—O(9,10) and the Na—O(1–8) interactions are essentially the same, so the optical nonlinearity of NaTP is impacted only by the overall closer sodium–oxygen contacts. In AgTP, silver plainly favors selective siting coordination with titanyl oxygen atom O(9) (Fig. 11), disrupting conjugation in the $(Ti—O)_n$ chain. In NaTA, the closer coordination of sodium to the framework is counteracted by the increased basicity of the AsO_4 groups, which in effect draw these ions away from the titanyl chain. In this respect, NaTA behaves more like KTA than NaTP.

The low SHG intensity of AgTP is thus readily explained by both the high electronegativity of Ag (relative to K) and the strong coordination of Ag(1) and Ag(2) to the titanyl oxygen atoms. Similarly, the close association of Na with the Ti—O framework oxygen atoms reduces SHG intensity by an order of magnitude despite the similar electronegativities of Na and K. The looser Na coordination with the titanyl oxygen atoms in NaTA allows this material to have a strong nonlinear response. In addition, the effects of any increase in cation framework covalency are likely to be mitigated by arsenate substitution, which should increase the basicity of the oxygen levels, facilitating their mixing with the metallic charge-transfer band orbitals.

There are numerous other examples of selective siting in the KTP structures. Selectively removing ammonia from one of the ammonium ions in ammonium titanyl phosphate results in selective siting of the proton at O(9) (93). The SHG can be switched with hydrogen bonding by the ammonium ions in ammonium titanyl phosphate (SHG active) and ammonium titanyl arsenate (SHG inactive). The transition from active to inactive has been monitored by systematically following ammonium ion exchange substitution into the corresponding KTP and KTA derivatives and independently by following framework arsenate substitution into the ammonium titanyl phosphate derivative (11). Site selectivity is frequently observed and used.

The reader hopefully will have a picture of a host continuum lattice with multiple coordination sites. The basicity of the oxygen atoms in this surface can be modified by framework substitution (arsenate and phosphate). Guest ions of different charge density and size can be incorporated in the host pores and used to perturb the guest surface with huge effects on the electrooptic properties. It is a very practical example of nanocomposite synthesis and tuning.

V. CONCLUSION

The understanding and new synthetic approaches to nanocluster synthesis have opened extensive new vistas for all areas of science. The incorporation of nanoclusters into composite synthesis will require the continued development of highly sophisticated new chemical techniques and nanoscale engineering. Much will depend on the ability to utilize and understand the exterior surface chemistry of the nanocluster phases and the corresponding interfaces with their environment. Similar considerations can be used to control cluster geometry and size distribution by the topography of 3-D host surfaces, making it possible to create semiconductor quantum supralattices. The use of large 3-D surface areas permits concentration studies of cluster interactions over a wide range, and at relatively high optical densities. It is to be expected that novel, normally very unstable, nanosized phases can be synthesized and stabilized via encap-

sulation and integration with the open framework systems that are now being developed.

The synthesis of nanoporous hosts with surfaces that can be functionalized and used in the self-organization of host, or which themselves have unusual electrooptic properties, is certain to play an important part in nanoscale inclusion chemistry. The KTP structural family is only one example of a potentially very rich field. The smaller channel systems that can be used for this purpose means that there is potentially a much larger host base. It also means that there is a greater likelihood of success in terms of crystal or thin-film growth and general processibility for device applications. There are many unanswered questions and unexplored areas from the basic research point of view. As noted in the introduction, synthetic solid state chemistry is for the most part still in its infancy and is almost certain to continue to produce the exciting discoveries that have marked the past few years.

ACKNOWLEDGMENTS

The contributions of the undergraduates, graduate students, and post-doctoral associates who have so greatly contributed to the author's education during the past six years at UCSB; the support of the author's wife, Kaaren, during the writing of this chapter; and funding from the National Science Foundation through the Quantized Electronic Structures Science and Technology Center (QUEST), and the Division of Materials Research, Du Pont, and the Office of Naval Research are greatly appreciated.

REFERENCES

1. L. E. Brus, *Proceedings of the Robert A. Welch Foundation Conference on Chemical Research, XXXII Valency*, Houston, TX 1988, pp. 45–62.
2. M. L. Steigerwald and L. E. Brus, *An. Rev. Mater. Sci.*, *19*, 471 (1989).
3. A. Henglein, *Topics Curr. Chem.*, *143*, 113 (1988).
4. Y. Wang and N. Herron, *Phys. Chem.*, *91*, 257 (1987).
5. S. Schmitt-Rink, D. S. Chemla, and D. A. B. Miller, *Adv. Phys.*, *38*, 89 (1989).
6. D. A. B. Miller, *Opt. Photonics*, February 7–15, (1990).
7. S. Andersson, S. T. Hyde, K. Larsson, and S. Lidin, *Chem. Rev.*, *88*, 221 (1988).
8. M. A. Fox and T. C. Pettit, *Langmuir*, *5*, 1056 (1989).
9. S. R. Marder, J. E. Sohn, and G. D. Stucky (Eds.), *Materials for Nonlinear Optics: Chemical Perspectives, ACS Symposium Series*, 1991, Vol. 455.
10. R. L. Kubena, R. J. Joyce, J. W. Ward, J. L. Gavin, S. P. Stratton, and R. G. Brault, *App. Phys. Lett.*, *50*, 1589 (1987).

11. G. D. Stucky, M. L. F. Phillips, and T. E. Gier, *Chem. Mater.*, *1*, 492 (1989).
12. N. F. Borelli, D. W. Hall, H. J. Holland, and D. W. Smith, *J. Appl. Phys.*, *61*, 5399 (1987).
13. Y. Wang and W. Mahler, *Opt. Commun.*, *61*, 233 (1987).
14. M. P. Andrews and G. A. Ozin, *Chem. Mater.*, *1*, 174 (1989).
15. H. Weller, H. M. Schmidt, U. Koch, A. Fojtik, S. Baral, A. Henglein, W. Kunath, K. Weiss, and E. Dieman, *Chem. Phys. Lett.*, *124*, 557 (1986).
16. DY-M. Tricot and J. H. Fendler, *J. Phys. Chem.*, *90*, 3369 (1986).
17. W. Mahler, *Inorg. Chem.*, *27*, 435 (1988).
18. T. Rajh, M. I. Vucemilovic, N. M. Dimitrijevic, O. I. Micic, and A. J. Nozik, *Chem. Phys. Lett.*, *143*, 305 (1988).
19. J. Zink, B. Dunn, R. B. Kaner, E. T. Knobbe, and J. McKieman, in *Materials for Nonlinear Optics: Chemical Perspectives*, S. Marder, J. E. Sohn, and G. D. Stucky (Eds.), American Chemical Society Symposium Series, 1991, Vol. 455, p. 541.
20. Y. Horikoshi, M. Kawashima, and H. Yamaguchi, *Jpn. J. Appl. Phys.*, *25*, L868 (1986).
21. D.-R. Dai, M. A. Hubbard, D. Li, J. Park, M. A. Ratner, T. J. Marks, J. Yang, and G. K. Wong, in *Materials for Nonlinear Optics: Chemical Perspectives*, S. Marder, J. E. Sohn, and G. D. Stucky (Eds.), American Chemical Society Symposium Series, 1986, Vol. 455, p. 26.
22. E. S. Smotkin, C. Lee, A. J. Bard, A. Campion, M. A. Fox, T. E. Mallouk, T. E. Webber, and J. E. White, *Chem. Phys. Lett.*, *152*, 265 (1988).
23. S. Akhter, H. Lee, H. G. Hong, T. E. Mallouk, and J. M. White, *J. Vac. Sci. Technol.*, *A7*, 1608 (1989).
24. M. A. Reed, R. T. Bate, K. Bradshaw, W. M. Duncan, W. R. Frensley, J. W. Lee, and H. D. Shih, *J. Vac. Sci. Technol.*, *B4*, 358 (1986).
25. R. D. Dupuis, R. C. Miller, and P. M. Petroff, *J. Crystal Growth*, *68*, 398 (1984).
26. R. C. Miller, A. C. Gossard, D. A. Kleinman, and O. Munteanu, *Phys. Rev.*, *B29*, 7085 (1984).
27. T. Iwamoto, in *Inclusion Compounds*, J. L. Atwood, J. E. Davies, and D. D. MacNicol (Eds.), Academic, New York, 1984, Vol. 1, pp. 29–57.
28. R. Robson, Symposium on Supramolecular Architecture in Two and Three Dimension, American Chemical Society 201st National Meeting, Atlanta, GA, 1991.
29. V. N. Bogomolov and A. I. Zadorozhnii, *Fiz. Tverd. Tela (Leningrad)*, *13*, 2771 (1971).
30. V. N. Bogomolov, *Fiz. Txverd. Tela*, *13*, 815 (1971).
31. V. N. Bogomolov, E. V. Kolla, and Y. A. Kumzerov, *Solid State Commun.*, *46*, 151 (1983).
32. A. F. Wells, *Structural Inorganic Chemistry*, Clarendon, Oxford, 1975.
33. D. C. Groult, C. Michel, and B. Raveau, *J. Inorg. Nucl. Chem.*, *36*, 61 (1974).
34. R. Schollhorn, in *Inclusion Compounds*, J. L. Atwood, J. E. D. Davis, and D. D. MacNicol (Eds.), Academic, New York, 1984, Vol. 1, p. 249.

35. L. Ouvrard, *Compt. Rend., 121*, 117 (1990).
36. R. Masse and J. C. Grenier, *Bull. Soc. Fr. Mineral. Cristallogr., 94*, 437 (1971).
37. I. Tordjman, R. Masse, and J. C. Guitel, *Z. Krist., 139*, 103 (1974).
38. D. W. Breck, in *Zeolite Molecular Sieves*, Wiley, New York, 1974.
39. R. M. Barrer, in *Zeolites and Clay Minerals as Sorbents and Molecular Sieves*, Academic, New York, 1978.
40. R. Szostak, *Molecular Sieves, Principles of Synthesis and Identification*, Van Nostrand Reinhold, New York, 1989.
41. H. van Bekkum, E. M. Flanigen, and J. C. Jansen (Eds.), in *Studies in Surface Science and Catalysis: Introduction to Zeolite Science and Practice*, Elsevier, New York, 1991, p. 58.
42. H. W. Kroto, J. R. Heath, S. C. O'Brien, R. F. Curl, and R. E. Smalley, *Nature (London), 318*, 162 (1985).
43. J. V. Smith, *Chem. Rev., 88*, 171(1988).
44. E. M. Flanigen, J. M. Bennett, R. W. Grose, J. P. Cohen, R. L. Patton, R. M. Kirchner, and J. V. Smith, *Nature (London), 271*, 512 (1978).
45. S. T. Wilson, B. M. Lok, C. A. Messina, T. R. Cannan, and E. M. Flanigen, *Intrazeolite Chemistry*, American Chemical Society Symposium Series, 1983, p. 79, Vol. 218.
46. S. T. Wilson, B. M. Lok, C. A. Messina, T. R. Cannan, and E. M. Flanigen, *J. Am. Chem. Soc., 104*, 1146 (1982).
47. B. M. Lok, C. A. Messina, R. L. Patton, R. T. Gajek, T. R. Cannan, and E. M. Flanigen, *J. Am. Chem. Soc., 106*, 6092 (1984).
48. S. T. Wilson and E. M. Flanigen, U.S. Patent 4 567 029, 1986.
49. L. J. Wright and N. B. Milestone, Eur. Patent Appl. 0 141 662, 1985.
50. D. R. Pyke and P. Whitney, *H. Houghton Appl. Catal., 18*, 173 (1985).
51. G. C. Bond, M. R. Gelsthorpe, and K. S. Sing, *J. Chem. Soc. Commun., 1056*, (1985).
52. E. M. Flanigen, B. M. Lok, R. L. Patton, and S. T. Wilson, *Pure Appl. Chem., 58*, 1351 (1986).
53. S. T. Wilson and E. M. Flanigen, *Zeolite Synthesis*, M. L. Occelli and H. E. Robson (Eds.), American Chemical Society Symposium Series, 1989, Vol. 398, p. 329.
54. (a). M.E. Davis, C. Saldarriaga, C. Montes, J. Garces, and C. Crowder, *Nature (London), 331*, 698 (1988). (b). M. E. Davis, C. Saldarriaga, C. Montes, J. Garces, and C. Crowder, *Zeolites, 8*, 362 (1989).
55. D. W. Breck, in *Zeolite Molecular Sieves*, Robert Krieger Publishing, Malabar, FL, 1984.
56. H. Kessler and C. Baerlocher, *Nature (London), 352*, 320 (1991).
57. T. E. Gier and G. D. Stucky, *Nature (London), 349*, 508 (1991).
58. J. M. Newsam and J. D. Jorgensen, *Zeolites, 7*, 569 (1987).
59. M. O'Keefe, *Acta Cryst. B34*, 27, (1978).

60. J. Felsche, S. Luger, and C. Baerlocher, *Zeolites, 6*, 367 (1986).
61. G. D. Stucky, V. I. Srdanov, W. T. A. Harrison, T. E. Gier, N. Keder, K. L. Moran, K. Haug, and H. Metiu, *Supramolecular Chemistry*, American Chemical Society Symposium Series, vol. 273, 1991.
62. W. T. A. Harrison, T. E. Gier, and G. D. Stucky, *J. Mater. Chem., 1*, 153, (1991).
63. T. M. Nenoff, W. T. A. Harrison, T. E. Gier, and G. D. Stucky, *J. Am. Chem. Soc. 113*, 378 (1991).
64. W. T. A. Harrison, T. E. Gier, K. L. Moran, J. M. Nicol, H. Eckert, and G. D. Stucky, *Chem. Mater., 3*, 27 (1991).
65. T. E. Gier, W. T. A. Harrison, and G. D. Stucky, *Ang. Chem., 103*, 1191 (1991).
66. Y. Ortiz-Avila, P. R. Rudolf, and A. Clearfield, *Inorg. Chem., 28*, 2137 (1989).
67. C. Y. Ortiz-Avila, P. J. Squattrito, M. Shieh, and A. Clearfield, *Inorg. Chem., 28*, 2608 (1989).
68. G. Cao, H. Lee, V. M. Lynch, and T. E. Mallouk, *Inorg. Chem., 27*, 2781 (1988).
69. F. Fajula, M. Vera-Pacheco, and F. Figueras, *Zeolites, 7*, 203 (1987).
70. D. Domine and J. Quobex, in *Molecular Sieves*, R. M. Barrer (Ed.), Society of Chemical Industry, London, 1968, p. 78.
71. D. W. Breck and E. M. Flanigen, in *Molecular Sieves*, R. M. Barrier (Ed.), Society of Chemical Industry, London, 1968, p. 47.
72. F. Y. Dai, M. Suzuki, H. Takahashi, and Y. Saito, in *New Developments in Zeolite Science and Technology*, Y. Murakami, A. Iijima, and J. W. Ward (Eds.), Elsevier, Amsterdam, 1986, p. 223.
73. G. A. Jeffrey, in *Inclusion Compounds*, J. L. Atwood, J. D. D. Davies, and D. D. MacNicol (Eds.) Academic, New York, 1984, pp. 135–190.
74. F. Suganuma, T. Yoshinari, and T. Sera, *Jpn. Kokai Tokyo Koho, 6*, (1987).
75. Y. Xu, P. J. Maddox, and J. W. Couves, *J. Chem. Soc. Faraday Trans., 86*, 425 (1990).
76. (a) G. Bomchil, A. Halimaoui, and R. Herino, *Microelectronic Eng., 8*, 293 (1988). (b) J. M. Keen, European Solid State Device Research Conference, ESSDERC 90, 20th, Nottingham, UK, 1991, p. 1631. (c) R. L. Bedard, S. T. Wilson, L. D. Vail, J. M. Bennet, and E. M. Flanigen, "Zeolites: Facts, Figures, Future," in *Studies in Surface Science and Catalysis*, P. A. Jacobs and R. A. van Santen (Eds.), 1989, pp. 375–387.
77. J. B. Parise, *Science, 251*, 293 (1991).
78. D. R. Corbin, J. F. Whitney, W. C. Fultz, G. D. Stucky, M. M. Eddy, and A. K. Cheetham, *Inorg. Chem., 25*, 2279 (1986).
79. L. A. Mundi, K.G. Strohmaier, and R. C. Haushalter, *Inorg. Chem., 30*, 153 and references cited therein (1991).
80. P. B. Moore and J. Shen, *Nature (London), 306*, 356 (1983).
81. M. J. Buerger, W. A. Dollase, and I. Garaycochea-Wittke, *Z. Kristallogr. Kristallgeom., Kristallphys., Kristallchem., 125*, 92 (1967).

82. E. Hauser, H. Bittner, and H. Nowotny, *Monatsh. Chem.*, *101*, 1864 (1970).
83. N. N. Nevskii, V. V. Ilyukhin, L. I. Ivanova, and N. V. Belov, *Dokl. Akad. Nauk SSSR*, *245*, 110 (1979).
84. H. Kessler, Material Resource Society Symposium, Anaheim, April (1991).
85. K. A. Hofmann and F. A. Kuspert, *Z. Anorg. Allg. Chem.*, *15*, 204 (1987).
86. B. F. Hoskins and R. Robson, *J. Am. Chem. Soc.*, *112*, 1546 (1990).
87. B. F. Abrahams, B. F. Hoskin, and R. Robson, *J. Am. Chem. Soc.*, *113(9)*, 3606 (1991).
88. L. Pauling, *Proc. Natl. Acad. Sci.*, *16*, 578 (1930).
89. T. F. Bates, F. A. Hildebrand, and A. Swineford, *Am. Mineralog.*, *35*, 463 (1950).
90. T. F. Bates, *Am. Mineralog.*, *44*, 78 (1959).
91. D. M. Roy and R. Roy, *Am. Mineralog.*, *39*, 957 (1954).
92. K. Yada, *Acta Crystallogr.*, *A27*, 659 (1971).
93. M. M. Eddy, T. E. Gier, N. L. Keder, G. D. Stucky, D. E. Cox, J. D. Bierlein, and G. Jones, *Inorg. Chem.*, *27*, 1856 (1988).
94. P. A. Morris, M. K. Crawford, A. Ferretti, R. H. French, M. G. Roelofs, J. D. Bierlein, and J. B. Brown, *Mater. Res. Soc. Symp. Proc.*, 152; also in Opt. Mater.: Process 1989, *Sci.*, 95 (1989).
95. P. A. Morris, in *Materials for Nonlinear Optics Chemical Perspectives*, S. R. Marder, J. E. Soh, and G.D. Stucky (Eds.), American Chemical Society Symposium Series, 1991, Vol. 455, p. 380.
96. M. L. Phillips, T. E. Gier, M. M. Eddy, N. L. Keder, G. D. Stucky, and J. D. Bierlein, *Solid State Ionics*, *32/33*, 147 (1989).
97. J. Sauer, *Chem. Rev.*, *89*, 199 (1989).
98. R. Vetrival, C. R. A. Catlow, and E. A. Colbourn, "Innovation in Zeolite Materials Science," in *Studies in Surface Science and Catalysis*, P. J. Grobet et al. (Eds.), Elsevier, Amsterdam, 1988, Vol. 37, p. 309.
99. L. Uytterhoeven, W. J. Mortier, and P. Geerlings, *J. Phys. Chem. Solids*, *50*, 479 (1989).
100. K. A. Van Genechten, W. J. Mortier, and P. J. Geerlings, *J. Chem. Phys.*, *86*, 5063.
101. J. B. Nicholas, A. J. Hopfinger, F. R. Trouw, and L. E. Iton, *J. Am. Chem. Soc.*, *113*, 4792 (1991).
102. J. D. Gale, A. K. Cheetham, R. A. Jackson, R. C. Richard, A. Catlow, and J. M. Thomas, *Adv. Mater.*, *2*, 487 (1990).
103. A. K. Nowak, C. J. J. DenOuden, S. D. Pickett, B. Smit, A. K. Cheetham, M. F. M. Post, and J. M. Thomas, *J. Phys. Chem.*, *95*, 848 (1991).
104. R. L. June, A. T. Bell, and D. N. Theodorou, *J. Phys. Chem.*, *94*, 8232 (1990).
105. R. A. van Santen, D. P. De Bruyn, C. J. J. DenOuden, and B. Smit, in *Studies in Surface Science and Catalysis: Introduction to Zeolite Science and Practice*, H. van Bekkum, E. M. Flanigen and J. C. Jansen (Eds.), Elsevier, New York, 1991, Vol. 58, p. 317.

106. P. Demontis, G. B. Suffritti, S. Quartieri, E. S. Fois, and A. J. Gamba, *J. Phys. Chem.*, *92*, 867 (1988).

107. R. Dovesi, C. Pisani, C. Roetti, M. Causa, and V. R. Saunders, *CRYSTAL88: An ab Initio All-Electron LCAO Hartree-Fock Program for Periodic Systems*; QCPE Program No. 577, Quantum Chemistry Program Exchange, Indiana University, Bloomington, IN, 1988.

108. J. Sauer and D. Deininger, *Zeolites*, *2*, 114 (1982).

109. R. T. Sanderson, *Chemical Bonds and Bond Energy*, Academic, New York, 1976, p. 138.

110. R. J. Hill, M. Newton, and G. V. Gibbs, *J. Solid State Chem.*, *47*, 185 (1983).

111. S. Grigoras and T. H. Lane, *J. Comp. Chem.*, *9*, 25 (1988).

112. V. Bosacek, D. Freude, T. Froehlich, H. Pfeifer, and H. Schmiedel, *J. Colloid Interface Sci.*, *85*, 502 (1982).

113. T. Masuda, K. Tsutsumi, and H. Takahashi, *J. Colloid Interface Sci.*, *77*, 238 (1980).

114. E. CohendeLara and Y. Delaval, *J. Chem. Soc. Faraday Trans. 2*, *74*, 790 (1978).

115. D. Denney, V. M. Mastikhin, S. Namba, and J. Turkevich, *J. Phys. Chem.*, *82*, 1752 (1978).

116. K. Tsutsumi and H. Takahashi, *J. Phys. Chem.*, *76*, 110 (1972).

117. E. Dempsey, in *Molecular Sieves*, Society of Chemical Industry, London, 1968, p. 293.

118. P. H. Kasai and R. J. Bishop, Jr., in *Zeolite Chemistry and Catalysis*, J. A. Rabo (Ed.), American Chemical Society, 1976, pp. 350–391.

119. V. Ramamurthy, J. V. Caspar, and D. R. Corbin, *J. Am. Chem. Soc.*, *113*, 594 (1991).

120. *Studies in Surface Science and Catalysis*, Elsevier, New York, Vols. 33, 37, 46, 49a, 49b, 52, and 58.

121. P. B. Weisz, *Chemtech*, *3*, 498 (1973).

122. R. M. Moore and J. R. Katzer, *AIChE J.*, *18*, 816 (1972).

123. A. P. Alivisatos, A. L. Harris, N. J. Levinos, M. L. Steigerwald, and J. E. Brus, *Chem. Phys.*, *89*, 4001 (1988).

124. N. Herron, Y. Wang, M. M. Eddy, G. D. Stucky, D. E. Cox, K. Moller, and T. Bein, *J. Am. Chem. Soc.*, *111*, 530 (1989).

125. R. M. Barrer and J. F. Cole, *J. Chem. Soc. A*, *9*, 1516 (1970).

126. D. A. Fursenko, in *Fiz. Khim. Issled. Mineraloobraz. Sist.*, A. A. Godovikov (Ed.), Akad. Nauk SSSR, Sib. Otd., Inst. Geol. Geofiz., Novosibirsk, USSR, 1982, pp. 104–107.

127. R. M. Barrer, in *Hydrothermal Chemistry of Zeolites*, Academic, London, 1982.

128. I. Hassan and P. R. Buseck, *Am. Mineral.*, *74*, 394 (1989).

129. G. D. Stucky, T. Gier, and W. T. H. Harrison, unpublished data.

130. J. B. Barrie and J. J. Klinowski, *Phys. Chem.*, *93*, 5972 (1989).

131. B. Beagley, C. M. B. Henderson, and D. Taylor, *Mineral. Mag.*, *46*, 459 (1982).

132. D. R. Corbin, L. Abrams, G. A. Jones, R. L. Harlow, and P. J. Dunn, *Zeolites*, *11*, 364 (1991).
133. J. B. Parise, X. Liu, and D. R. Corbin, *J. Chem. Soc. Chem. Commun.*, *3*, 162 (1991).
134. D. R. Corbin, L. Abrams, G. A. Jones, M. M. Eddy, W. T. A. Harrison, G. D. Stucky, and D. E. Cox, *J. Am. Chem. Soc.*, *112*, 4821 (1990).
135. R. M. Barrer, in *Inclusion Compounds*, J. L. Atwood, J. E. D. Davies and D. D. MacNicol (Eds.), Academic, New York, 1983, Vol. 1.
136. W. T. A. Harrison, T. E. Gier, and G. D. Stucky, *Chem. Commun.*, 540 (1990).
137. S. C. Abrahams, S. K. Kurtz, and P. J. Jamieson, *Phys. Rev.*, *172*, 551 (1968).
138. G. A. Kourouklis, A. Jayaraman, and A. A. Ballman, *Solid State Commun.*, *62*, 379 (1987).
139. R. M. Hazen and L. W. Finger, *J. Appl. Phys.*, *56*, 1838 (1984).
140. R. M. Hazen, *Science*, *219*, 1065 (1983).
141. G. D. Stucky, D. R. Corbin, and G. A. Jones, unpublished results.
142. S. Ozkar, G. A. Ozin, K. Moller, and T. Bein, *J. Am. Chem. Soc.*, *112*, 9575 (1990).
143. J. Caro, B. Zibrowius, and G. Finger, Germ. Patent Appl. DP 41 09 038, March 15, 1991.
144. R. M. Barrer, E. F. Vansant, and G. Peeters, *J. Chem. Soc. Faraday Trans. 1*, *74*, 1871 (1978).
145. T. Bein, R. F. Carver, R. D. Farlee, and G. D. Stucky, *J. Am. Chem. Soc.*, *110*, 4546 (1988).
146. T. Bein, D. B. Chase, R. D. Farlee, and G. D. Stucky, *Stud. Surf. Sci. Catal.*, *28*, 311 (1986).
147. A. Borvornwattananont, K. Moller, and T. Bein, *J. Chem. Soc. Chem. Commun.*, *1*, 28 (1990).
148. G. A. Ozin, M. D. Baker, J. Godbe, and C. Gil, *J. Phys. Chem.*, *93*, 2899 (1989).
149. G. A. Ozin and S. Ozkar, *J. Phys. Chem.*, *94*, 7556 (1990).
150. D. R. Corbin, M. Keane, L. Abrams, R. D. Farlee, P. E. Bierstedt, and T. Bein, *J. Catal.*, *124*, 268 (1990).
151. J. S. Krueger, J. E. Mayer, and T. E. Mallouk, *J. Am. Chem. Soc.*, *110*, 8232 (1988).
152. L. Persaud, A. J. Bard, A. Campion, M. A. Fox, T. E. Mallouk, S. E. Webber, and J. E. White, *J. Am. Chem. Soc.*, *109*, 7309 (1987).
153. Z. Li and T. E. Mallouk, *J. Phys. Chem.*, *91*, 643 (1987).
154. Z. Li, C. Lai, T. E. Mallouk, and E. Thomas, *Inorg. Chem.*, *28*, 178 (1989).
155. L. Persaud, A. J. Bard, A. Campion, M. A., Fox, T. E. Mallouk, S. E. Webber, and J. E. White, *Inorg. Chem.*, *26*, 3825 (1987).
156. A. L. Weisenhorn, J. E. MacDougall, S. A. C. Gould, S. D. Cox, W. S. Wise, J. Massie, P. Maivald, V. B. Elings, G. D. Stucky, and P. K. Hansma, *Science*, *247*, 1330 (1990).

157. V. N. Bogomolov and A. I. Zadorozhnii, *Fiz. Tverd. Tela (Leningrad)*, *17*, 1652 (1975).
158. R. M. Barrer and J. L. Whiteman, *J. Chem. Soc. A*, *1*, 19 (1967).
159. W. P. Halperin, *Rev. Mod. Phys.*, *58*, 533 (1986).
160. J. A. Rabo, C. L. Angell, P. H. Kasai, and V. Schomaker, *Faraday Soc. Discuss.*, *41*, 328 (1966).
161. R. M. Barrer and J. F. Cole, *J. Phys. Chem. Sol.*, *29*, 1755 (1968).
162. M. R. Harrison, P. P. Edwards, J. Klinowski, J. M. Thomas, D. C. Johnson, and C. J. Page, *J. Sol. State. Chem.*, *54*, 330 (1984).
163. U. Westphal and G. Geismar, *Z. Anorg. Allg. Chem.*, *508*, 165 (1984).
164. J. B. A. F. Smeulders, M. A. Hefni, A. A. K. Klaassen, E. DeBoer, U. Westphal, and G. Geismar, *Zeolites*, *7*, 347 (1987).
165. G. Geismar and U. Westphal, *Chem. Ztg.*, *111*, 2772 (1987).
166. R. E. H. Breuer, E. DeBoer, and G. Geismar, *Zeolites 1989*, *9*, 336 (1989).
167. F. M. Tranjan and L. T. Todd, *J. Electrochem. Soc.*, *135*, 2288 (1988).
168. K. Ota and K. Ono, *Jpn. Tokkyo Koho*, *5*, (1985).
169. V. Denko, *Tr. In-ta Fiz. AN ESSR*, *55*, 14 (1984).
170. G. Liu, Proc. International Symposium Hydrothermal Reactions, 1st Meeting Date 1982, S. Shigeyuki (Ed.), Gakujutsu Bunken Fukyu-kai, Tokyo, Japan, 1983, pp. 553–560.
171. G. A. Ozin, A. Stein, G. D. Stucky, and J. P. Goodbar, *Proceedings of 5th Inclusion Phenomena and Molecular Recognition*, Jerry Atwood (Ed.), Plenum, New York, 1990, pp. 379–393.
172. P. H. Kasai, *J. Chem. Phys.*, *43*, 3322 (1965).
173. S. L. Suib, R. P. Zerger, G. D. Stucky, R. M. Emberson, P. G. Debrunner, and L. E. Iton, *Inorg. Chem.*, *19*, 1858 (1980).
174. G. D. Stucky. L. E. Iton, T. Morrison, G. Shenoy, S. Suib, and R. P. Zerger, *J. Mol. Catal.*, *27*, 71 (1984).
175. L. R. M. Martens and P. A. Jacobs, *Nature (London)*, *315*, 568 (1985).
176. D. Taylor and C. M. B. Henderson, *Phys. Chem. Minerals*, *2*, 325 (1978).
177. K. Haug, V. Srdanov, G. Stucky, and H. Metiu, *J. Phys. Chem.* (1992) in press.
178. B. Barrachin and E. J. CohendeLara, *Chem. Soc. Faraday Trans. 2*, *82*, (1953).
179. T. Ito and J. J. Fraissard, *Chem. Soc. Faraday Trans. 1*, *83*, 451 (1987).
180. S. J. Beran, *Mol. Catal.*, *45*, 225 (1988).
181. L. Leherte, *Chem. Phys. Lett.*, *145*, 237 (1988).
182. F. Vigne-Meader and A. J. Auroux, *Phys. Chem.*, *94*, 316 (1990).
183. N. F. Mott, in *Metal-Insulator Transitions*, Taylor & Francis, London, 1990.
184. A. Stein, P. M. Macdonald, G. A. Ozin, and G. D. Stucky, *J. Phys. Chem.*, *94*, 6943 (1990).
185. A. Stein, G. A. Ozin, and G. D. Stucky, *J. Am. Chem. Soc.*, *112*, 904 (1990).
186. T. E. Gier, unpublished results.

187. T. E. Mallouk, private communication.
188. K. L. Moran, W. T. A. Harrison, T. E. Gier, J. E. MacDougall, and G. D. Stucky, *Mater. Res. Soc. Symp. Proc.*, *164*, 123 (1990).
189. Y. Wang and N. Herron, *J. Phys. Chem.*, *92*, 4988 (1988).
190. K. Moller, M. M. Eddy, G. D. Stucky, N. Herron, and T. Bein, *J. Am. Chem. Soc.*, *111*, 2564 (1989).
191. K. Moller, T. Bein, N. Herron, W. Mahler, J. MacDougall, and G. D. Stucky, *Mol. Cryst. Liq. Cryst.*, *181*, *305 (1990)*.
192. G. D. Stucky and J. E. MacDougall, *Science*, *247*, 669 (1990).
193. S. D. Cox, Ph.D. Thesis, University of California, Santa Barbara, 1989.
194. J. E. MacDougall, H. Eckert, G. D. Stucky, N. Herron, Y. Wang, K. Moller, T. Bein, and D. Cox, "New Nonlinear Materials Through Inclusion Chemistry," *J. Am. Chem. Soc.*, *111*, 8006 (1989).
195. R. M. Barrer and W. M. Meier, *J. Chem. Soc.*, 299 (1958).
196. R. M. Barrer and A. G. Kanellopoulos, *J. Chem. Soc.*, *A*, 775 (1970).
197. R. M. Barrer and J. Klinowski, *J. Chem. Soc. Faraday 2*, *74*, 904 (1978).
198. J. R. Johns and R. F. Howe, *Zeolites*, *5*, 251 (1985).
199. T. Ishihara, J. Takahashi, and T. Goto, *Phys. Rev. B: Condens. Matter*, *42*, 11099 (1990).
200. J. Calabrese, N. L. Jones, R. L. Harlow, N. Herron, D. L. Thorn, and Y. Wang, *J. Am. Chem. Soc.*, *113*, 2328 (1991).
201. O. Teraskai, K. Yamazaki, J. M. Thomas, T. Ohsuna, D. Watanable, J. V. Sanders, and J. C. Barr, *Nature (London)*, *330*, 6143 (1987).
202. O. Teraskai, K. Yamazaki, J. M. Thomas, T. Ohsuna, D. Watanabe, J. V. Sanders, and J. C. Barr, *J. Sol. State Chem.*, *77*, 72 (1988).
203. Y. Nozue, T. Kodaira, O. Terasaki, K. Yamazaki, T. Goto, D. Watanabe, and J. M. Thomas, *J. Phys. Condens. Matter 2*, 2509 (1990).
204. Y. Nozue, Z. K. Tang, and T. Goto, *Solid State Commun.*, *73*, 531 (1990).
205. O. Terasaki, Z. K. Tang, Y. Nozue, and T. Goto, Materials Research Society, Anaheim, CA, 1991.
206. G. A. Ozin, S. Ozkar, and P. Macdonald, *J. Phys. Chem.*, *94*, 6939 (1990).
207. G. A. Ozin, S. Kirkby, M. Meszaros, S. Ozkar, A. Stein, and G. D. Stucky, in *Materials for Nonlinear Optics*, S. Marder, J. Sohn and G. D. Stucky (Eds.), American Chemical Society Symposium Series, 1991, Vol. 455, pp. 554–581.
208. F. A. Cotton, *Advanced Inorganic Chemistry*, Wiley-Interscience, New York, 1988.
209. V. N. Bogomolov, *Usp. Fiz. Nauk*, *124*, 171 (1978).
210. V. N. Bogomolov and Yu. A. Kumzerov, *Pisma Zh. Eksp. Teor. Fiz.*, *21*, 434 (1975).
211. S. D. Cox, T. E. Gier, G. D. Stucky, and J. Bierlein, *J. Am. Chem. Soc.*, *110*, 2986 (1988).

212. S. D. Cox, T. E. Gier, G. D. Stucky, and J. Bierlein, *Solid State Ionics*, Volume Date 1988, 32-33 *(Pt. 1)*, 514 (1989).

213. J. M. Nicol, T. J. Udovic, J. J. Rush, S. D. Cox, and G. D. Stucky, *Mater. Res. Soc. Symp. Proc.*, *166*, 367 (1990).

214. S. D. Cox, T. E. Gier, and G. D. Stucky, *Chem. Mater.*, *2*, 609 (1990).

215. S. D. Cox and G. D. Stucky, *J. Phys. Chem.*, *95*, 710 (1991).

216. D. J. Williams, *Angew. Chem. Int. Ed. Engl.*, *23*, 690 (1984).

217. *Royal Society of Chemistry Special Publication No. 69: Organic Materials for Nonlinear Optics. The Proceedings of a Conference Organized by the Applied Solid State Chemistry Group of the Dalton Division of The Royal Society of Chemistry, Oxford, June 29-30, 1988*; R. A. Hann and D. Bloor (Eds.), Royal Society of Chemistry, London, 1989.

218. G. Khanarian (Ed.), *Proc. SPIE - Int. Soc. Opt. Eng., Nonlinear Optical Properties of Organic Materials*, *971*, SPIE, 1988.

219. *Nonlinear Optical Properties of Polymers*, A. J. Heeger, J. Orenstein, and D. R. Ulrich (Eds.), MRS Symposium Proceedings, 109, Pittsburgh, PA, 1988.

220. *Nonlinear Optical Properties of Organic Molecules and Crystals*, D. S. Chemla and J. Zyss (Eds.), Academic, New York, 1987, Vol. 1.

221. G. R. Meredith, *Mater. Res. Bull.*, *13*, 24 (1988).

222. S. R. Marder, J. W. Perry, and W. P. Schaefer, *Science*, *245*, 626 (1989).

223. S. Tomaru, S. Zembutsu, M. Kawachi, and M. Kobayashi, *J. Chem. Soc. Chem. Commun.*, 1207 (1984).

224. S. Tomaru, S. Zembutsu, M. Kawachi, and M. Kobayashi, *J. Incl. Phenom.*, *2*, 885 (1984).

225. Y. Wang and D. F. Eaton, *Chem. Physl. Let.*, *120*, 441 (1985).

226. D. F. Eaton, A. G. Anderson, W. Tam, and Y. Wang, *J. Am. Chem. Soc.*, *109*, 1886 (1987).

227. W. Tam, D. F. Eaton, J. C. Calabrese, I. D. Williams, Y. Wang, and A. G. Anderson, *Chem. Mater.*, *1*, 128 (1989).

228. I. Weissbuch, M. Lahav, L. Leiserowitz, G. R. Meredith, and H. Vanherzeele, *Chem. Mater.*, *1*, 114 (1989).

229. J. M. Bennet, J. P. Cohen, E. M. Flanigen, J. J. Pluth, and J. V. Smith, in *Intrazeolite Chemistry, ACS Symposium Series 218*, G. D. Stucky and F. G. Dwyer (Eds.), American Chemical Society, Washington, DC, 1983, pp. 109-118.

230. J. M. Bennett, J. W. Richardson, Jr., J. J. Pluth, and J. V. Smith, *Zeolites*, *6*, 160 (1987).

231. L. B. McCusker, C. Baerlocher, E. Jahn, and M. Buelow, *Zeolites*, *11*, 308 (1991).

232. J. A. Gard and J. M. Tait, *Acta. Cryst.*, *B28*, 825 (1972).

233. J. L. Oudar and J. Zyss, *Phys. Rev. A*, *26*, 2016 (1982).

234. D. F. Eaton, *Science*, *253*, 281 (1991).

235. J. L. Oudar and D. S. Chemla, *J. Chem. Phys.*, *66*, 2664 (1977).

236. B. F. Levine, C. G. Bethea, C. D. Thurmond, R. T. Lynch, and J. L. Bernstein, *J. Appl. Phys.*, *50*, 2523 (1979).
237. J. E. MacDougall, S. D. Cox, G. D. Stucky, A. L. Weisenhorn, P. K. Hansma, and W. S. Wise, *Zeolites*, *11*, 429 (1991).
238. M. C. Etter, K. S. Huang, G. M. Frankenbach, and D. A. Adsmond, in *Materials for Nonlinear Optics: Chemical Perspectives*, S. Marder, J. E. Sohn, and G. D. Stucky (Eds.), American Chemical Society Symposium Series, 1991, Vol. 455, pp. 446–456.
239. J. Zyss and J. L. Oudar, *Phys. Rev. A*, *26*, 2028 (1982).
240. O. S. Khalil and S. P. McGlynn, *J. Luminescence*, *11*, 185 (1975).
241. J. D. Bierlein and T. E. Gier, U. S. Patent 3 949 323, (1976).
242. T. E. Gier, *U.S. Patent 4 231 838*, 1980.
243. T. E. Gier, *U.S. Patent 4 305 778*, 1981.
244. J. D. Bierlein, A. Ferretti, L. H. Brixner, and W. H. Hsu, *Appl. Phys. Let.*, *50*, 1216 (1987).
245. J. D. Bierlein, *Proc. SPIE-Int. Soc. Opt. Eng.*, *1104*, 2 (1989).
246. W. T. A. Harrison, T. E. Gier, G. D. Stucky, and A. J. Schultz, *Chem. Commun.*, 540 (1990).
247. R. H. Jarman and S. G. Grubb, *Proc. SPIE-Int. Soc. Opt. Eng.*, *968*, 108 (1988).
248. M. L. F. Phillips, W. T. A. Harrison, and G. D. Stucky, *Inorg. Chem.*, *29*, 3245 (1990).
249. P. A. Thomas, A. M. Glazer, and B. E. Watts, *Acta Crystallogr. Sect. B: Struct. Sci.*, *B46*, 333 (1990).
250. J. G. Bergman and G. R. Crane, *J. Solid State Chem.*, *12*, 172 (1975).
251. B. F. Levine, *Phys. Rev. B.*, *10*, 1655 (1974).
252. G. Marnier, B. Boulanger, and B. Menaert, *J. Phys.: Condens. Matter*, *1*, 5509 (1989).
253. G. D. Stucky, S. R. Marder, and J. E. Sohn, *Materials for Nonlinear Optics: Chemical Perspective, ACS Symposium Series*, Vol. 455, p. 2.
254. J. K. Burdett and T. Hughbanks, *Inorg. Chem.*, *24*, 1741 (1967).
255. J. K. Burdett, *Inorg. Chem.*, *24*, 2244 (1985).
256. M. L. F. Phillips, W. T. A. Harrison, T. E. Gier, G. D. Stucky, G. V. Kulkarni, and J. K. Burdett, *Inorg. Chem.*, *29*, 2158 (1990).
257. G. Blasse and L. H. Brixner, *Mater. Res. Bull.*, *24*, 1099 (1989).

TECHNICAL REPORT DISTRIBUTION LIST - GENERAL

Office of Naval Research (2)*
Chemistry Division, Code 1113
800 North Quincy Street
Arlington, Virginia 22217-5000

Dr. James S. Murday (1)
Chemistry Division, Code 6100
Naval Research Laboratory
Washington, D.C. 20375-5000

Dr. Robert Green, Director (1)
Chemistry Division, Code 385
Naval Air Weapons Center
Weapons Division
China Lake, CA 93555-6001

Dr. Elek Lindner (1)
Naval Command, Control and Ocean
Surveillance Center
RDT&E Division
San Diego, CA 92152-5000

Dr. Bernard E. Douda (1)
Crane Division
Naval Surface Warfare Center
Crane, Indiana 47522-5000

Dr. Richard W. Drisko (1)
Naval Civil Engineering
Laboratory
Code L52
Port Hueneme, CA 93043

Dr. Harold H. Singerman (1)
Naval Surface Warfare Center
Carderock Division Detachment
Annapolis, MD 21402-1198

Dr. Eugene C. Fischer (1)
Code 2840
Naval Surface Warfare Center
Carderock Division Detachment
Annapolis, MD 21402-1198

Defense Technical Information
Center (2)
Building 5, Cameron Station
Alexandria, VA 22314

* Number of copies to forward